Super-regenerative Receiver for UWB-FM

Rui Hou

Department of Microelectronics
Delft University of Technology

September 20, 2008

Super-regenerative Receiver for UWB-FM

by

Rui Hou

A thesis submitted to the Department of Microelectronics, Faculty of Electrical Engineering, Mathematics and Computer Science, Delft University of Technology, in partial fulfillment of the requirements for the degree of

Master of Science

in

Microelectronics

Supervisors:

Prof. John R. Long
Nitz Saputra

Thesis committee:

Prof. John R. Long
Dr. ing. Leo C. N. de Vreede
Dr. Kofi A. A. Makinwa
Nitz Saputra

September 20, 2008

Abstract

UWB-FM is a low-complexity ultra-wideband (UWB) communication system designed for short-range, low- and medium-data-rate wireless applications such as the personal area network (PAN). These applications often require simple, integrated receivers with low power consumption.

Most of previous work utilized delay-line demodulators for UWB-FM detection. This coherent detection method offers the best performance in general but is not necessarily power-efficient. Reported power consumption was around 20 mW for a 2 GHz RF bandwidth.

The goal of this research is to explore the possibility of reducing power consumption of a UWB-FM receiver by exploiting the super-regeneration principle.

As a result, a fully integrated super-regenerative receiver in IBM 90-nm RF CMOS technology is designed to detect 500 MHz bandwidth UWB-FM signals at 4.5 GHz. Circuit simulations show that a receiver sensitivity of -82.2 dB is attainable for a 100 kbps baseband data-rate and 10^{-6} bit-error-rate. The whole receiver draws an average of 2 mA from a 0.9 V supply.

This work is, according to the author's knowledge, the first time the super-regeneration principle is used for UWB-FM detection. The 1.8 mW power dissipation is also by far the smallest among UWB-FM receivers reported in the literature. In addition, the contribution of this work includes an innovative optimization of the quenching waveform for WBFM detection and a novel low-power driven design procedure for LNAs.

In conclusion, super-regenerative receivers are promising for short-range, low-data-rate UWB-FM applications, due to their simplicity and low power-consumption.

Acknowledgments

The work presented in this thesis could not have been done without the help and influence of many individuals.

Firstly, I would like to give my gratitude to my supervisor, Prof. John R. Long, for his constant guidance and support. I have benefited greatly from his expertise, inspiration, criticism and encouragement.

Additionally, I am very grateful to Ph.D student Nitz Saputra, who is also taken care of my work from beginning to end. His broad knowledge has brought me out of trouble quite a few times. Our discussions are always delightful, full of insights and enlightenment. I thank him for his valuable feedback regarding my thesis.

I would also like to thank the committee members, Prof. Leo de Vreede and Prof. Kofi Makinwa for their time reading this thesis and attending the defense.

Working in the Electronics group has been quite a pleasant experience, due to the kind and intelligent people there. In particular, I thank my college student Yixiong Hu and Yousif Shamsa. We have been cooperating for two years, and it has been a pleasure since then.

This two years studying in Delft University of Technology has been colorful and full of adventure. Before my graduation, I would like to express my gratitude to all the professors and teachers who gave me lectures and trainings. Evidently, I will benefit from the knowledge they imparted for the rest of my life. I thank all my college students for their kindness and help.

My family is always supporting me, especially during my study in the Netherlands. I am very grateful for that.

Last but not least, I am deeply thankful for the love, encouragement and support of my brilliant wife, Cheng Jiang.

Rui Hou

Delft, the Netherlands

Contents

List of Figures

List of Tables

Chapter 1

Introduction

1.1 Motivation

During the last 10 years, the rapidly advanced short-range communication technologies are creating new opportunities for interconnections such as personal area networks (PAN) and wireless sensor networks (WSN). These networks have many potential applications, ranging from clinical diagnosis to wildlife monitoring. The network nodes are necessarily simple and highly integrated so they can be massively produced to reduce the cost. Low power consumption is also an indispensable feature for these devices, since consumer products with bulky batteries are unattractive and field deployment of ephemeral sensors is unacceptable.

A wireless transceiver is a critical component providing the communication link between distributed nodes. Reducing its cost and power consumption leads to global cost and power saving, comfortably portable consumer products and extended lifetime of field-deployed sensors.

1.2 Purpose and Scope of the Research

The goal of this research is to explore the possibility of reducing power consumption of a UWB-FM receiver by exploiting the super-regeneration principle. UWB-FM [1] is a low-power low-complexity ultra-wideband (UWB) modulation scheme designed for short-range, low- and medium-data-rate (LDR and MDR) PAN and WSN applications. It utilizes the wideband frequency modulation (WBFM) to spread the spectrum of a continuous carrier over a large bandwidth. Super-regeneration [2, 3] is the process of amplifying radio frequency (RF) signals through the periodically building-up oscillations. Super-regenerative receivers (SRR) are naturally suited for low-power low-complexity applications, by virtue of their simple structure and low power-consumption [4, 5, 6, 7, 8, 9, 10].

To demonstrate the feasibility of UWB-FM detection by super-regeneration and its low-power potential, a receiver is implemented in IBM 90-nm RF CMOS technology. According to the requirements of short-range UWB-FM applications, this receiver should have an operating frequency of 4.5 GHz, an RF bandwidth of 500 MHz, a data-rate of 100 kbps, a bit-error-rate of 10^{-6} and a line-of-sight communication range of 10 meters, with low power-consumption as the fundamental design objective.

1.3 Thesis Organization

This thesis focuses on the design and implementation of a super-regenerative receiver for UWB-FM applications. Chapter 2 provides the background about the UWB-FM modulation scheme, previous work and the current approach. Chapter 3 analyzes mathematically the super-regeneration theory, which forms a solid foundation for the following design practice. In Chapter 4, the receiver specification is derived based on its application background; an architecture is selected and the system-level simulation result is presented to demonstrate the feasibility of the receiver. Chapter 5 concentrates on the circuit design of the RF part of the receiver, including a super-regenerative oscillator (SRO), a peak detector and a low-noise amplifier (LNA). This chapter also presents an innovative optimization of the quenching waveform for WBFM detection and a novel low-power driven design procedure for the LNA. Chapter 6 focuses on the circuit design of the analog part of the receiver, including a current saw-tooth waveform generator for the SRO, a dynamic biasing circuit for the LNA, an output buffer for testability and a current reference for biasing. In Chapter 7, the simulation set-up of the complete receiver is introduced and the simulation result is presented. This chapter also details a global power reduction attempt and an iteration of the design process. Chapter 8 concludes the thesis with a summary of research results and discussion of future work directions.

Chapter 2

Background

2.1 UWB-FM Modulation Scheme

UWB-FM is a low-power low-complexity UWB modulation scheme targeting short-range, low- and medium-data-rate wireless applications [1]. This scheme involves double frequency modulations (FM), a low modulation-index frequency shift keying (FSK) followed by a high modulation-index analog FM.

The double FM scheme is illustrated in Fig. 2.1. As shown in the graph, a digital baseband signal, $d(t)$, having a data rate of 20, 40 or 100 kbps, modulates a triangular subcarrier of 1-2 MHz, $m(t)$, using FSK with a modulation index of 1. The subcarrier, $m(t)$, then modulates the RF carrier of 3-5 GHz, $v(t)$, using FM, to spread its spectrum to a bandwidth of 500 MHz. The modulation indexes and the RF carrier frequency shown in the graph have been modified for the sake of visibility.

The power spectrum of a UWB-FM signal centering at 4.5 GHz, being modulated by a 1 MHz triangular wave, is shown in Fig. 2.2. The low-cost low-power demodulation of this signal to reconstruct the subcarrier is the problem studied in this research.

2.2 Previous Work

Most of previous work utilized delay-line demodulators for the UWB-FM detection [11, 12]. The block diagram of such a demodulator is shown in Fig. 2.3. A delay element first converts the input FM signal into a PM signal. Then a multiplier, operating as a phase detector, recovers the modulation signal. This coherent detection scheme provides the best dynamic range in principle [13]. However, since a mixer and a high gain amplifier are used at the RF frequency, UWB-FM receivers incorporating delay-line demodulators are not necessarily power-efficient.

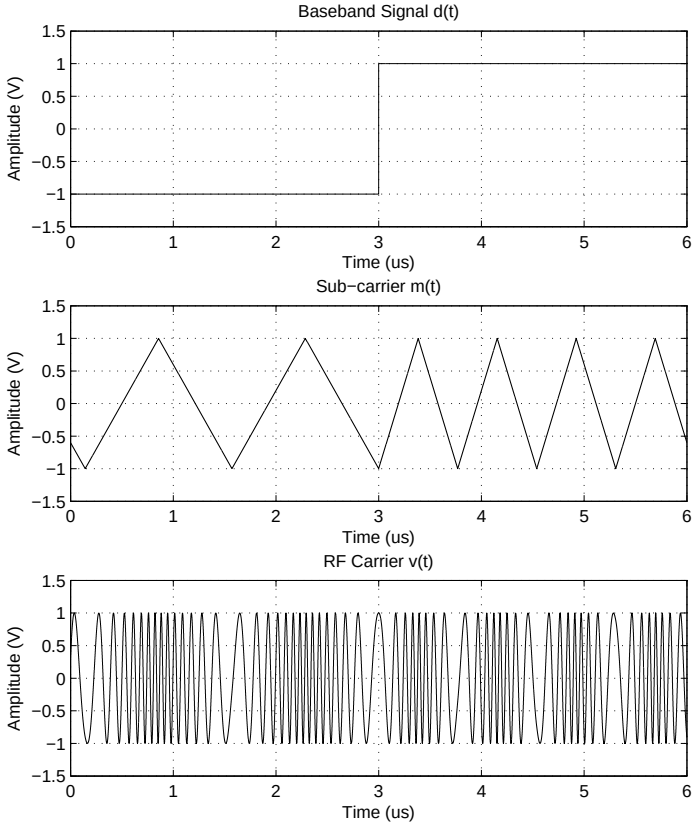

Figure 2.1: The time-domain waveform of the baseband data, subcarrier and UWB signal.

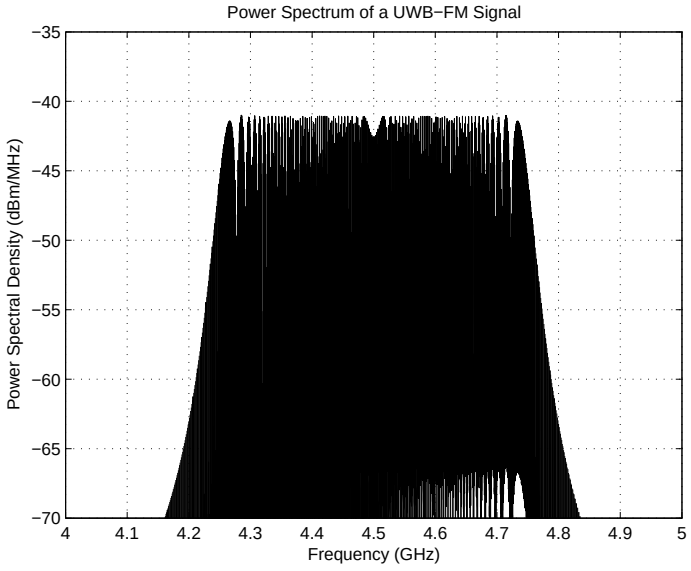

Figure 2.2: Power spectrum of the UWB-FM signal.

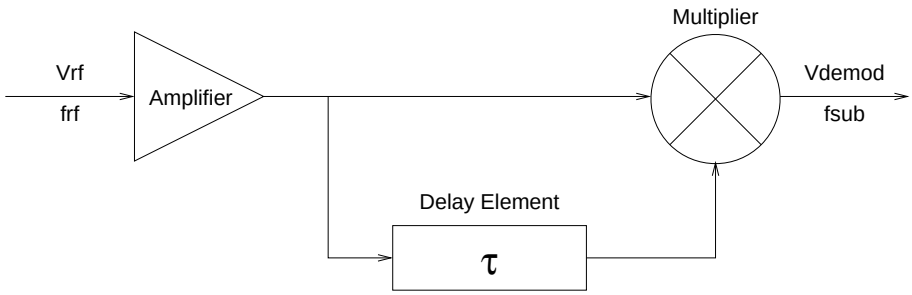

Figure 2.3: WBFM delay-line demodulator.

In the literature, power consumption of 2 GHz bandwidth receivers is reported. One implementation excluding LNA, fabricated in 0.18 um Si-Ge BiCMOS technology, consumes 9.6 mW power [11]. Another one including an LNA, implemented in 0.18 um CMOS process, consumes 19.4 mW [12].

2.3 Current Approach: Super-regeneration

This research explores the possibility of reducing power consumption of UWB-FM demodulation by exploiting the super-regeneration principle.

Super-regenerative receivers were invented by Edwin H. Armstrong in 1922 [2]. Employing positive feedback, these receivers operated in an intermittent oscillatory condition. Oscillations were periodically built up from weak RF excitation and then quenched to avoid amplification saturation. In doing so, a huge amount of gain could be obtained by a single stage. The amplification was so remarkable that a single vacuum tube could amplify noise to an audible level.

However, super-regenerative receivers have never been in a dominant position, since their drawbacks are also conspicuous. Firstly, super-regenerators are inherently also an oscillator. The spurious emission of these receivers can easily cause interference. Secondly, classical super-regenerative receivers suffer from poor frequency selectivity. Thirdly, super-regenerative receivers are inherently frequency unstable. Due to these drawbacks, super-regenerative receivers have limited narrow-band applications, such as garage-door openers, toys, and low cost walkie-talkies.

The literature has shown revived interests of super-regenerative receivers for the last 10 years. Short-range low-data-rate wireless applications have a growing demand for low-power low-cost receivers. Super-regenerative receivers, due to their simplicity and huge gain, are naturally a candidate architecture. Typically, this type of receivers have been designed for simple narrow-band modulation schemes such as on-off keying (OOK) [4, 5, 6, 7, 8, 9, 10], providing that proper measures [14, 15] are taken to improve the poor selectivity and inherent frequency instability. Occasionally, they were also used to detect spread spectrum [16, 17] and pulse based

UWB signals [18, 19, 20], benefiting from the alleviated selectivity and frequency-stability requirements of these applications.

The classical way of applying super-regeneration principle to FM detection is based on the slope demodulation process [21]. In essence, a super-regenerator is detuned from the RF center frequency so as to generate variable gain for frequency variation. Other techniques [22, 23] are also seen in the literature.

Chapter 3

Super-regeneration

3.1 Introduction

Super-regenerative receivers, despite their structural simplicity , are quasi-periodical nonlinear time-varying dynamical systems. The difficulty in modeling their behavior results the commonly used "cut and try" design methodology. In fact, the underlying theory [3, 24] is so complex that it has never been understood by more than a handful of people at a given time [25]. However, many trade-offs occurring in this design practice rely on the underlying mathematics, as will be presented in the rest of the thesis.

Super-regenerative receivers have two modes of operations, the linear and the logarithmic mode. In the linear operation mode, growing-up oscillations are quenched *before* the amplitude saturation shows its effect. In such a way, the peaking oscillation amplitude has a linear relationship with the initial RF excitation amplitude. In contrast, the logarithmic operation mode quenches the oscillations *after* the amplitude saturation. In doing so, all the pulses have the same amplitude. The different RF power is distinguished by the different duration of oscillations, since large RF excitation yields faster oscillation building-up, and vice versa. The duration of oscillations is logarithmically proportional to the initial RF excitation.

A logarithmic-mode super-regenerative receiver is modeled by a nonlinear ordinary differential equation with variable coefficients, whose analytical solution does not necessarily exist. Therefore, this chapter focuses on the linear-mode response of the system. Since the properties of the two modes differ only at the end of an oscillation build-up cycle, many results obtained in this analysis are also relevant to the logarithmic mode.

The differential equation modeling super-regenerative oscillators are presented in Section 3.2 and solved in Section 3.3. Based on this solution, the characteristics of super-regenerators are further analyzed in Section 3.4.

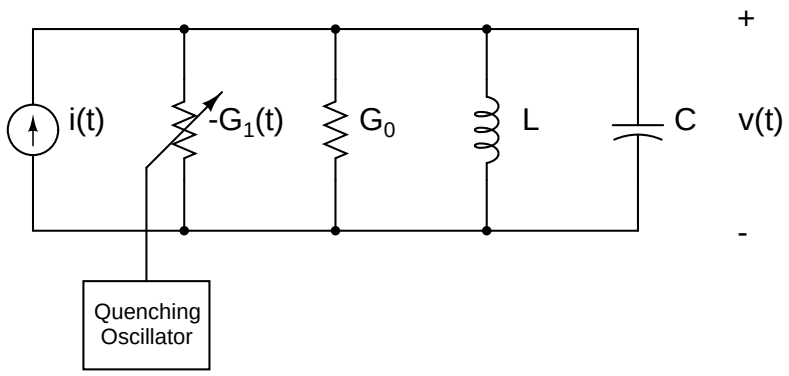

Figure 3.1: Super-regenerative oscillator.

3.2 Driven Parametric Oscillator Model

Super-regenerative oscillators are externally stimulated oscillators with time-varying damping coefficients. A circuit representation of such an oscillator is shown in Fig. 3.1, where a periodically time-varying negative conductance modifies the damping of a parallel RLC resonant tank. SROs originated from delay-line oscillators can be better modeled as a variable-gain amplifier in a positive feedback loop [24]. Since they are mathematically equivalent, the rest of this chapter will use Fig. 3.1 as the SRO model without losing generality.

The differential equation characterizing the time varying dynamical system shown in Fig 3.1 can be derived using Kirchhoff's current law

$$C\frac{\mathrm{d}v\left(t\right)}{\mathrm{d}t}+G\left(t\right)v\left(t\right)+\frac{1}{L}\int v\left(t\right)\mathrm{d}t=i\left(t\right). \tag{3.1}$$

Differentiating both sides yields

$$\ddot{v}\left(t\right)+\frac{G\left(t\right)}{C}\dot{v}\left(t\right)+\left[\frac{1}{LC}+\frac{\dot{G}\left(t\right)}{C}\right]v\left(t\right)=\frac{\dot{i}\left(t\right)}{C}, \tag{3.2}$$

where

$$G\left(t\right)=G_0-G_1\left(t\right) \tag{3.3}$$

is the time varying conductance of the resonant tank.

The waveforms of the varying conductance are shown in Fig. 3.2 and 3.3. A quenching cycle starts from time 0. The total conductance of the tank is positive during the period from time 0 to t_1, and negative during the period from t_1 to t_2. If the transition of conductance at t_1 and t_2 are slow, such that the regeneration period includes many oscillation cycles, as shown in Fig. 3.2, the SRO is called to be working in a slope-controlled state. On the other hand, if the transition of conductance at t_1 and t_2 are fast compared with oscillation cycles, as shown in Fig.

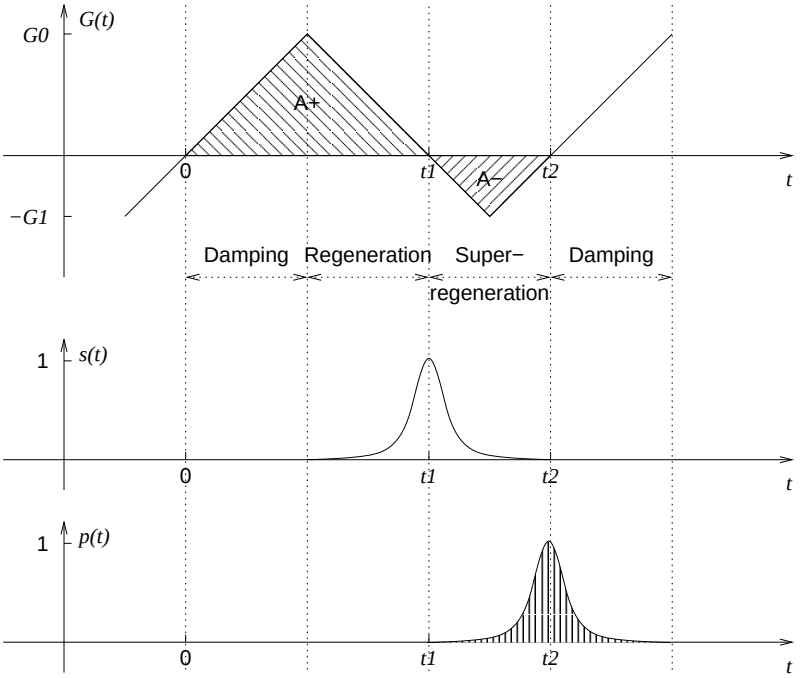

Figure 3.2: Slope-controlled state: the conductance $G(t)$, sensitivity $s(t)$ and pulse envelope $p(t)$.

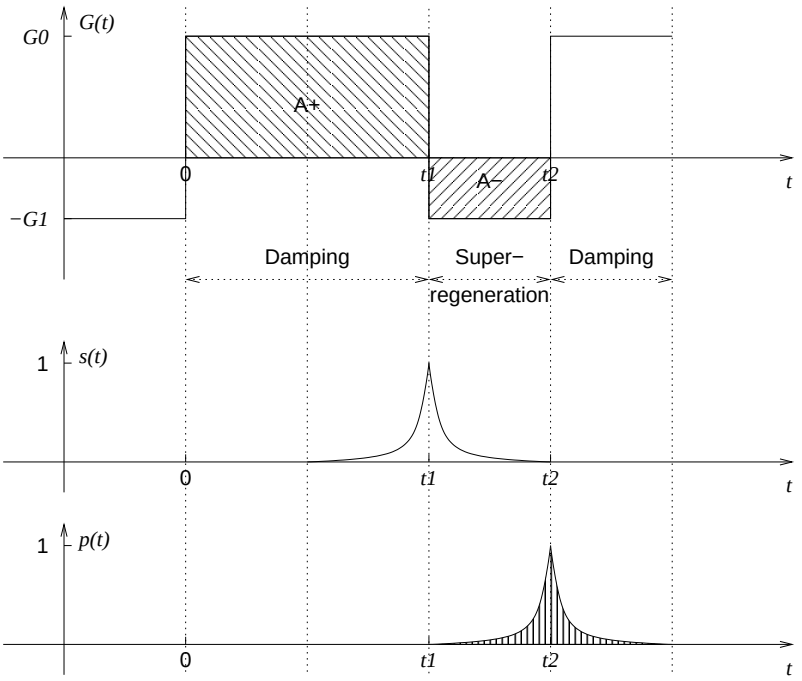

Figure 3.3: Step-controlled state: the conductance $G(t)$, sensitivity $s(t)$ and pulse envelope $p(t)$.

3.3, the SRO is called to be working in a step-controlled state.

The division of receiver operation into two states is historical and artificial. In the following analysis, it will be shown that the generic solution suitable for all types of waveforms is too general to be of any practical use. The two operation states are the two extreme situations, whose solutions in closed analytical forms exist. The operation using any other conductance waveforms, e.g. a sinusoidal wave, can be approximated by the combination of the two extreme cases with accuracy.

Equ. 3.2 is a second-order linear ordinary differential equation (ODE) with variable coefficients. The next section derives the solution of this equation.

3.3 Solution of the ODE

The complete set of solutions of a second-order linear ordinary differential equation can be represented as

$$v(t) = \left[\begin{array}{cc} v_{z1}(t) & v_{z2}(t) \end{array} \right] \left[\begin{array}{c} c_1 \\ c_2 \end{array} \right] + v_p(t) \tag{3.4}$$

where the first term is the general solution and the second term, the particular solution. The general solution is the natural response, or zero-input response, of the dynamical system, when no stimulus is applied. The particular solution, on the other hand, is the forced response, or zero-state response, of the dynamical system, when a particular stimulus is applied to a system initiating from the relaxed state.

In following subsections, the fundamental system of the general solution, the vector containing $v_{z1}(t)$ and $v_{z2}(t)$, is first derived from the corresponding homogeneous equation. Then the particular solution, $v_p(t)$, is derived using the method of variation of the parameters. At last, the complete solution is determined and discussed.

3.3.1 General Solution

Assuming zero input, we obtain the corresponding homogeneous equation of Equ. 3.2

$$\ddot{v}(t) + 2\zeta(t)\omega_0\dot{v}(t) + \left[\omega_0^2 + 2\omega_0\dot{\zeta}(t)\right] v(t) = 0\,, \tag{3.5}$$

where

$$\zeta(t) = \frac{G(t)}{2C\omega_0} \tag{3.6}$$

is the time-varying damping factor, and

$$\omega_0 = \frac{1}{\sqrt{LC}} \tag{3.7}$$

is the natural frequency. Equ. 3.5 represents an undriven parametric oscillator. The standard procedure to solve this equation is to transform it into Hill equation by eliminating the damping term.

This transformation is accomplished by a change of variables

$$v(t) = x(t) \exp\left[-\omega_0 \int_0^t \zeta(t)\, \mathrm{d}t\right]. \tag{3.8}$$

Substituting Equ. 3.8 and

$$\dot{v}(t) = \left[\dot{x}(t) - \omega_0 \zeta(t)\, x(t)\right] \exp\left[-\omega_0 \int_0^t \zeta(t)\, \mathrm{d}t\right] \tag{3.9}$$

$$\ddot{v}(t) = \left\{\ddot{x}(t) - 2\omega_0 \zeta(t)\, \dot{x}(t) + x(t)\left[\omega_0^2 \zeta^2(t) - \omega_0 \dot{\zeta}(t)\right]\right\} \exp\left[-\omega_0 \int_0^t \zeta(t)\, \mathrm{d}t\right] \tag{3.10}$$

into Equ. 3.5 yields [1]

$$\ddot{x}(t) + \left[\omega_0^2 - \omega_0^2 \zeta^2(t) + \omega_0 \dot{\zeta}(t)\right] x(t) = 0\,. \tag{3.11}$$

Equ. 3.11 can be further simplified into the equation of free oscillation

$$\ddot{x}(t) + \omega_0^2 x(t) \approx 0, \tag{3.12}$$

on condition that

$$\zeta^2(t) \ll 1 \tag{3.13}$$

and

$$\left|\dot{\zeta}(t)\right| \ll \omega_0. \tag{3.14}$$

We shall briefly examine these conditions before going on. Equ. 3.13 implies under-damping in both positive and negative conductance periods. More specifically, in order to validate the free oscillation simplification, the instantaneous quality factor of the resonant tank should always satisfy

$$Q(t) = \frac{\omega_0 C}{G(t)} = \frac{1}{2\zeta(t)} \gg 0.5\,. \tag{3.15}$$

Equ. 3.14 implies a slow conductance variation compared with the oscillation frequency. In other words, the system is assumed to be quasi-static to the oscillation when we use the free oscillation approximation.

Given that conditions 3.13 and 3.14 are satisfied, Equ. 3.11 degenerates into

[1] It is worth mentioning here that the Hill equation, 3.11, characterizes a special type of amplifiers – parametric amplifiers, which was a popular choice for high-performance LNAs back in the 1970s [26].

Equ. 3.12, which is a linear constant-coefficient ODE. Applying Laplace transform to both sides yields

$$s^2X(s) - sX\left(0^-\right) - \dot{X}\left(0^-\right) + \omega_0^2 X(s) = 0\,, \tag{3.16}$$

which has the solution in complex frequency domain

$$X(s) = \frac{sX(0^-) + \dot{X}(0^-)}{s^2 + \omega_0^2}. \tag{3.17}$$

Performing inverse Laplace transform gives us the time-domain solution to Equ. 3.12

$$x(t) = \left[X\left(0^-\right)\cos\omega_0 t + \frac{\dot{X}(0^-)}{\omega_0}\sin\omega_0 t\right] u(t) \tag{3.18}$$

or in the vector form of Equ. 3.4

$$x(t) = \begin{bmatrix} \cos(\omega_0 t) & \sin(\omega_0 t) \end{bmatrix} \begin{bmatrix} V_i \\ V_q \end{bmatrix} u(t)\,, \tag{3.19}$$

where $u(t)$ is the Heaviside step function and V_i and V_q are real constants representing the inphase and quadrature amplitude of the free oscillation to be determined by boundary conditions. Substituting Equ. 3.19 into Equ. 3.8, we obtain the general solution to the ODE of super-regenerative oscillators

$$v_z(t) = \exp\left[-\omega_0 \int_0^t \zeta(t)\,\mathrm{d}t\right] \begin{bmatrix} \cos(\omega_0 t) & \sin(\omega_0 t) \end{bmatrix} \begin{bmatrix} V_i \\ V_q \end{bmatrix} u(t)\,. \tag{3.20}$$

Equ. 3.20 is the natural response, or zero-input response, of the super-regenerative oscillator. We can observe from this equation that when no input is applied, the output of an SRO is an exponentially growing or decaying sinusoidal signal with frequency determined by the resonant tank. Whether the envelope is growing or decaying depends on the integration of the damping function, or the accumulative conductance. When the accumulative conductance is positive, the envelope of the output is decaying, and vice versa.

3.3.2 Particular Solution

The particular solution of the inhomogeneous linear ODE 3.2 is based on the same fundamental system as the one derived from its corresponding homogeneous equation 3.5. So it should be of the form

$$v_p(t) = \exp\left[-\omega_0 \int_0^t \zeta(t)\,\mathrm{d}t\right] \begin{bmatrix} \cos(\omega_0 t) & \sin(\omega_0 t) \end{bmatrix} \begin{bmatrix} v_i(t) \\ v_q(t) \end{bmatrix} \tag{3.21}$$

where $v_i(t)$ and $v_q(t)$ are the time-varying inphase and quadrature amplitudes to be determined in the following part of this subsection.

If Equ. 3.21 satisfies the homogeneous equation, $v_i(t)$ and $v_q(t)$ need to be constants, in other words,

$$\exp\left[-\omega_0 \int_0^t \zeta(t)\,\mathrm{d}t\right] \begin{bmatrix} \cos(\omega_0 t) & \sin(\omega_0 t) \end{bmatrix} \begin{bmatrix} \dot{v_i}(t) \\ \dot{v_q}(t) \end{bmatrix} = 0\,. \tag{3.22}$$

Substituting Equ. 3.21 into Equ. 3.2 and applying Equ. 3.22, we obtain

$$\frac{\mathrm{d}}{\mathrm{d}t}\left\{\exp\left[-\omega_0 \int_0^t \zeta(t)\,\mathrm{d}t\right] \begin{bmatrix} \cos(\omega_0 t) & \sin(\omega_0 t) \end{bmatrix}\right\} \begin{bmatrix} \dot{v_i}(t) \\ \dot{v_q}(t) \end{bmatrix} = \frac{\dot{i}(t)}{C}\,. \tag{3.23}$$

Combining Equ. 3.22 and 3.23, we can solve $\dot{v_i}(t)$ and $\dot{v_q}(t)$ using Crammer's rule, resulting

$$\dot{v_i}(t) = \frac{\begin{vmatrix} 0 & y(t)\sin(\omega_0 t) \\ \frac{\dot{i}(t)}{C} & \sin(\omega_0 t)\,\dot{y}(t) + \omega_0 \cos(\omega_0 t)\,y(t) \end{vmatrix}}{W(t)} = -\frac{\sin(\omega_0 t)\,\dot{i}(t)}{y(t)\,\omega_0 C} \tag{3.24}$$

$$\dot{v_q}(t) = \frac{\begin{vmatrix} y(t)\cos(\omega_0 t) & 0 \\ \cos(\omega_0 t)\,\dot{y}(t) - \omega_0 \sin(\omega_0 t)\,y(t) & \frac{\dot{i}(t)}{C} \end{vmatrix}}{W(t)} = \frac{\cos(\omega_0 t)\,\dot{i}(t)}{y(t)\,\omega_0 C}\,, \tag{3.25}$$

where

$$y(t) = \exp\left[-\omega_0 \int_0^t \zeta(t)\,\mathrm{d}t\right] \tag{3.26}$$

and the Wronskian determinant

$$W(t) = \begin{vmatrix} y(t)\cos(\omega_0 t) & y(t)\sin(\omega_0 t) \\ \cos(\omega_0 t)\,\dot{y}(t) - \omega_0 \sin(\omega_0 t)\,y(t) & \sin(\omega_0 t)\,\dot{y}(t) + \omega_0 \cos(\omega_0 t)\,y(t) \end{vmatrix}. \tag{3.27}$$

Integrating Equ. 3.24 and 3.25 and substituting the result back into Equ. 3.21 yields the particular solution

$$v_p(t) = \frac{y(t)}{\omega_0 C} \int_0^t \frac{\dot{i}(\tau)}{y(\tau)} \left[\sin(\omega_0 t)\cos(\omega_0 \tau) - \cos(\omega_0 t)\sin(\omega_0 \tau)\right] \mathrm{d}\tau\,. \tag{3.28}$$

We further simplify the solution by applying the angle sum identity and substituting Equ. 3.26 into 3.28

$$v_p(t) = \frac{1}{\omega_0 C} \exp\left[-\omega_0 \int_0^t \zeta(t)\,\mathrm{d}t\right] \int_0^t \dot{i}(\tau) \exp\left[\omega_0 \int_0^\tau \zeta(t)\,\mathrm{d}t\right] \sin\omega_0(t-\tau)\,\mathrm{d}\tau\,. \tag{3.29}$$

We split the second exponential integral interval into $[0, t_1]$ and $[t_1, \tau]$. The former one becomes τ independent and can be moved out, combined with the first exponential integral, yielding

$$v_p(t) = \frac{1}{\omega_0 C} \exp\left[-\omega_0 \int_{t_1}^{t} \zeta(t)\,\mathrm{d}t\right] \int_0^t \dot{i}(\tau) \exp\left[\omega_0 \int_{t_1}^{\tau} \zeta(t)\,\mathrm{d}t\right] \sin\omega_0(t-\tau)\,\mathrm{d}\tau\,. \tag{3.30}$$

Equ. 3.30 can also be expressed in a compact form

$$v_p(t) = \frac{1}{\omega_0 C} K_s p(t) \int_0^t \dot{i}(\tau)\, s(\tau) \sin\omega_0(t-\tau)\,\mathrm{d}\tau \tag{3.31}$$

where

$$K_s = \exp\left[-\omega_0 \int_{t_1}^{t_2} \zeta(t)\,\mathrm{d}t\right] \tag{3.32}$$

is the super-regenerative gain,

$$p(t) = \exp\left[-\omega_0 \int_{t_2}^{t} \zeta(t)\,\mathrm{d}t\right] \tag{3.33}$$

is the normalized oscillation envelope, and

$$s(t) = \exp\left[\omega_0 \int_{t_1}^{t} \zeta(t)\,\mathrm{d}t\right] \tag{3.34}$$

is the sensitivity curve.

Equ. 3.31 is the forced response or zero-state response of super-regenerative oscillators under arbitrary stimulus. In this project, we are more interested in the SRO response of a constant-envelope frequency-modulated signal

$$i(t) = A\cos(\omega t + \phi)\ , \tag{3.35}$$

where A is the constant envelope, ϕ is the constant phase and ω is a slowly varying frequency. The derivative of this FM signal is

$$\dot{i}(t) = -A\sin(\omega t + \phi)\left(\omega + \frac{\mathrm{d}\omega}{\mathrm{d}t} t\right). \tag{3.36}$$

We further assume that the variation of the frequency in one quenching cycle is negligible comparing with the instantaneous frequency, i.e.

$$\frac{\mathrm{d}\omega}{\mathrm{d}t} t \ll \omega \text{ when } t \in [0, T_q] \tag{3.37}$$

which simplifies Equ. 3.36 into

$$\dot{i}\,(t) \approx -A\omega \sin\left(\omega t + \phi\right). \tag{3.38}$$

Substituting Equ. 3.38 into Equ. 3.31 yields

$$v_p\,(t) = \frac{-A\omega}{\omega_0 C} K_s p\,(t) \int_0^t s\,(\tau) \sin\left(\omega t + \phi\right) \sin\omega_0\,(t-\tau)\,\mathrm{d}\tau\,. \tag{3.39}$$

Applying trigonometric product-to-sum identity, we have

$$v_p\,(t) = \frac{-A\omega}{2\omega_0 C} K_s p\,(t) \int_0^t s\,(\tau) \left\{\cos\left[\tau\left(\omega+\omega_0\right) - \omega_0 t + \phi\right] - \cos\left[\tau\left(\omega-\omega_0\right) + \omega_0 t + \phi\right]\right\}\mathrm{d}\tau\,. \tag{3.40}$$

Assuming $\omega \approx \omega_0$, the integral of the first cosine term is nearly zero because of its high frequency. As a result, Equ. 3.40 can be approximated by

$$v_p\,(t) \approx \frac{A\omega}{2\omega_0 C} K_s p\,(t) \int_0^t s\,(\tau) \cos\left[\tau\left(\omega-\omega_0\right) + \omega_0 t + \phi\right]\mathrm{d}\tau. \tag{3.41}$$

Equ. 3.41 is the forced-response to the excitation given by Equ. 3.35.

3.3.3 Complete Solution

The complete solution of the linear varying-coefficient ODE 3.2 is the sum of its general solution given by Equ. 3.20 and its particular solution given by Equ. 3.41. Generally, to solve differential equations, we still need to apply boundary conditions to find out the unknown constants $\begin{bmatrix} V_i \\ V_q \end{bmatrix}$ in the general solution, Equ. 3.20. However, practical applications of super-regenerative oscillators make this final step unnecessary.

In SRO applications, we are more interested in the super-regeneration period. We often make natural responses of SROs negligible compared with magnitudes of input signals in that period, because forced responses provide amplification and natural responses are input independent. The suppression of the natural response is achieved by periodical quenching of oscillations. When the response of an SRO is primarily determined by its input, the SRO is called to be working in the noncoherent state. Otherwise, when the build-up of oscillations are not only triggered by the input signal, but also initiated by the residue oscillation from a previous quenching cycle, it is called hang-over and the SRO is called to be working in the coherent state. The coherent state of operation is undesirable because of its reduced sensitivity to incoming signals. Therefore, for properly designed super-regenerative oscillators

with negligible hang-over, their complete response in the super-regeneration phase should be dominated by their forced response given by Equ. 3.41.

3.4 Characteristics of an SRO

The previous section derives the response of an SRO under a constant envelope FM excitation. Based on this result, this section analyzes an SRO with respect to its sensitivity period, oscillation envelope, gain and frequency response.

3.4.1 Sensitivity Curve

The sensitivity curve is derived in Equ. 3.34 and rewritten here as

$$s(t) = \exp\left[\omega_0 \int_{t_1}^{t} \zeta(t)\,\mathrm{d}t\right]. \tag{3.42}$$

At $t = t_1$, it shows the maximum value of 1. When $t > t_1$, the damping is negative, so the sensitivity decays with time. When $t < t_1$, the damping is positive but its integral is negative, so the sensitivity also decays as t is getting away from t_1. Because of its exponential dependence on time, this curve is normally sharp. Practically, it can be seen as a sampling operation of the incoming signal at t_1. Because the value of $s(t)$ is close to zero when t is far away from t_1, we can change the integral interval of Equ. 3.41 from $[0, t]$ to $[0, t_2]$ or even $[-\infty, +\infty]$ when t is out of the sensitivity period. We can then write the Equ. 3.41 as

$$v_p(t) \approx \frac{A\omega}{2\omega_0 C} K_s p(t) \int_0^{t_2} s(\tau) \cos\left[\tau(\omega - \omega_0) + \omega_0 t + \phi\right] \mathrm{d}\tau \tag{3.43}$$

or even

$$v_p(t) \approx \frac{A\omega}{2\omega_0 C} K_s p(t) \int_{-\infty}^{\infty} s(\tau) \cos\left[\tau(\omega - \omega_0) + \omega_0 t + \phi\right] \mathrm{d}\tau. \tag{3.44}$$

We now separately study the two types of operations, namely the slope-controlled state and the step-controlled state. As shown in Fig. 3.2, the slope-controlled state has gradual damping transition from positive to negative values. Equ. 3.6 in this case is specified as

$$\zeta_{sl}(t) = \frac{-\alpha(t - t_1)}{2C\omega_0}, \tag{3.45}$$

where α denotes the absolute slope of conductance. Applying Equ. 3.42, we have the sensitivity curve in slope-controlled state

$$s_{sl}(t) = \exp\left[\frac{-\alpha(t - t_1)^2}{4C}\right]. \tag{3.46}$$

It has a shape of Gaussian functions, as shown in Fig. 3.2.

In the step-controlled state, performing the same procedure gives us

$$\zeta_{st}(t) = \begin{cases} \frac{G_0}{2C\omega_0} \text{ when } t < t_1 \\ \frac{-G_1}{2C\omega_0} \text{ when } t \geq t_1 \end{cases}, \tag{3.47}$$

and

$$s_{st}(t) = \begin{cases} \exp \frac{-G_0(t_1-t)}{2C} \text{ when } t < t_1 \\ \exp \frac{-G_1(t-t_1)}{2C} \text{ when } t \geq t_1 \end{cases}. \tag{3.48}$$

The sensitivity curve has a shape of a double-sided decaying exponential function, as shown in Fig. 3.3.

3.4.2 Oscillation Envelope

The oscillation envelope is derived in Equ. 3.33 and rewritten here as

$$p(t) = \exp\left[-\omega_0 \int_{t_2}^{t} \zeta(t)\,\mathrm{d}t\right]. \tag{3.49}$$

At $t = t_2$, it shows the maximum value of 1. When $t > t_2$, the damping and its integral are both positive, so the sensitivity decays with time. When $t < t_2$, the damping is negative but its integral is positive, so the sensitivity also decays as t is getting away from t_2. Similar to sensitivity, because of its exponential dependence on time, this curve is sharp. Practically, the oscillation envelope is a sharp pulse at t_2.

Following the same procedure that we use to derive the sensitivity curves, we can also obtain the oscillation envelope in slope-controlled state, in the form of a Gaussian function

$$p_{sl}(t) = \exp\left[\frac{-\alpha(t-t_2)^2}{4C}\right], \tag{3.50}$$

as shown in Fig. 3.2, and the one in step-controlled state, in the form of a double-sided decaying exponential function

$$p_{st}(t) = \begin{cases} \exp \frac{-G_0(t_2-t)}{2C} \text{ when } t < t_2 \\ \exp \frac{-G_1(t-t_2)}{2C} \text{ when } t \geq t_2 \end{cases}. \tag{3.51}$$

as shown in Fig. 3.3.

3.4.3 Gain

In the literature, the gain of a super-regenerative oscillator is divided into 3 parts, namely the passive gain, the regenerative gain and the super-regenerative gain.

The passive gain originates from the passive resonant tank. It is defined as

$$K_0 = \frac{1}{G_0}, \tag{3.52}$$

which trivially converts an input current into an output voltage.

The regenerative gain quantifies the amplification effect in the regeneration period. It is defined as

$$K_r = \frac{G_0}{2C} \int_0^{t_2} s\left(t\right) \mathrm{d}t\,, \tag{3.53}$$

which is determined by the area under the sensitivity curve. A wide sensitivity window yields high regenerative gain.

The super-regenerative gain originates from exponentially growing envelope in the negative-conductance period. It is derived from Equ. 3.32 and rewritten here as

$$K_s = \exp\left[-\omega_0 \int_{t_1}^{t_2} \zeta\left(t\right) \mathrm{d}t\right] = \exp\left[-\frac{1}{2C} \int_{t_1}^{t_2} G\left(t\right) \mathrm{d}t\right]. \tag{3.54}$$

It is exponentially proportional to the area under the negative conductance curve.

Substituting the three expressions of gain into Equ. 3.43 yields

$$v_p\left(t\right) = \frac{A\omega}{\omega_0} K_0 K_r K_s p\left(t\right) \frac{1}{\int_0^{t2} s\left(t\right) \mathrm{d}t} \int_0^{t_2} s\left(\tau\right) \cos\left[\tau\left(\omega - \omega_0\right) + \omega_0 t + \phi\right] \mathrm{d}\tau. \tag{3.55}$$

The meaning of Equ. 3.55 becomes clear if we assume $\omega = \omega_0$. In this situation, when the receiver is tuned to the frequency of the input signal, Equ. 3.55 becomes

$$v_p\left(t\right) = A K_0 K_r K_s p\left(t\right) \cos\left(\omega_0 t + \phi\right), \tag{3.56}$$

which indicates that the response of an SRO to a tuned signal is an oscillation with a gain of $K_0 K_r K_s$ and a pulse shape of $p\left(t\right)$.

3.4.4 Frequency Response

Applying Euler's formula to Equ. 3.44 yields

$$v_p\left(t\right) = \frac{A\omega}{2\omega_0 C} K_s p\left(t\right) \int_{-\infty}^{\infty} s\left(\tau\right) \left[\frac{e^{j\tau(\omega-\omega_0)} e^{j(\omega_0 t+\phi)}}{2} + \frac{e^{-j\tau(\omega-\omega_0)} e^{-j(\omega_0 t+\phi)}}{2}\right] \mathrm{d}\tau. \tag{3.57}$$

If we define the Fourier transform of the sensitivity function as

$$\psi(\omega) = \int_{-\infty}^{\infty} s(t) \exp(-j\omega t)\, \mathrm{d}t = \mathcal{F}\{s(t)\}, \tag{3.58}$$

then Equ. 3.57 can be expressed as

$$\begin{aligned} v_p(t) &= \frac{A\omega}{4\omega_0 C} K_s p(t) \left[\psi^*(\omega-\omega_0) e^{j(\omega_0 t+\phi)} + \psi(\omega-\omega_0) e^{-j(\omega_0 t+\phi)}\right] && (3.59)\\ &= \frac{A\omega}{2\omega_0 C} K_s p(t) \operatorname{Re}\left[\psi^*(\omega-\omega_0) e^{j(\omega_0 t+\phi)}\right] && (3.60)\\ &= \frac{A\omega}{2\omega_0 C} K_s p(t) \left|\psi^*(\omega-\omega_0)\right| \cos\left[\omega_0 t + \phi + \angle\psi^*(\omega-\omega_0)\right] && (3.61) \end{aligned}$$

where "*" stands for complex conjugate.

Equ. 3.61 implies that when the frequency deviation is small compared with the resonant frequency, the frequency response of an SRO is approximately the complex conjugate of the Fourier transform of the sensitivity curve.

Performing Fourier transform

$$e^{-at^2} \Longleftrightarrow \frac{1}{\sqrt{2a}} e^{-\frac{\omega^2}{4a}} \tag{3.62}$$

to Equ. 3.46 yields

$$\left|\psi_{sl} * (\omega-\omega_0)\right| = \sqrt{\frac{2C}{\alpha}} e^{-\frac{C}{\alpha}(\omega-\omega_0)^2} \tag{3.63}$$

Performing Fourier transform to Equ. 3.48 yields

$$\begin{aligned} \left|\psi_{st} * (\omega-\omega_0)\right| &= \left| \int_{-\infty}^{0} e^{\frac{G_0}{2C}t} e^{j\omega t} \mathrm{d}t + \int_{0}^{+\infty} e^{\frac{-G_1}{2C}t} e^{j\omega t} \mathrm{d}t \right| && (3.64)\\ &= \frac{\sqrt{\left[\frac{G_1 G_0}{4C^2} + (\omega-\omega_0)^2\right]^2 + \frac{(\omega-\omega_0)^2}{4C^2}(G_0-G_1)^2}}{\left[\frac{G_0^2}{4C^2} + (\omega-\omega_0)^2\right]\left[\frac{G_1^2}{4C^2} + (\omega-\omega_0)^2\right]} && (3.65) \end{aligned}$$

3.5 Conclusion

In this chapter, the characteristics of super-regenerative oscillators are mathematically examined. First, a driven parametric oscillator model is presented, and described as a second-order linear ordinary differential equation with varying coefficients. Then, the general solution and a particular solution under an excitation of a constant-envelope frequency-modulated signal are derived. After that, the complete response of the dynamical system in the super-regenerative period is approximated by its forced response. At last, characteristics of SROs, namely sensitivity, oscillation envelope, gain and frequency response are derived for SROs working in slope-

and step-controlled state.

The summarized SRO characteristics and even the simplification assumptions in the equation solving process given in this chapter are instrumental to the architecture and circuit design presented in the rest of the thesis. For example, in a later chapter, we will argue that the combination of a slope-controlled start-up and a step-controlled quenching yields the desirable receiver behavior for UWB-FM reception. In this stage, we can already predict by using Equ. 3.51 and 3.63 that the resulting frequency response has a Gaussian shape and the oscillation pulses have shapes of a double-sided decaying exponential function.

Chapter 4

Architecture Design

4.1 Introduction

In this chapter, the design issues in the architecture level are discussed. Section 4.2 derives the system specification based on the application background. The whole design process tries to satisfy the specification given at the end of this section. From the aspect of FM demodulation, Section 4.3 determines necessary blocks and their characteristics to be implemented in this receiver. The resulting block diagram of the UWB-FM receiver front-end is presented and explained in Section 4.4 and simulated in Section 4.5 to verify its feasibility in the system level.

4.2 System Specification

A typical UWB-FM receiver consists of an LNA, a WBFM demodulator and a sub-band FSK demodulator. The former 2 components constitute the receiver front-end to be implemented in this project, as shown in Fig. 4.1. The specification for complete UWB-FM receivers has been proposed in "My Personal Adaptive Global NET (MAGNET)" project [27]. This section discusses the corresponding requirements to

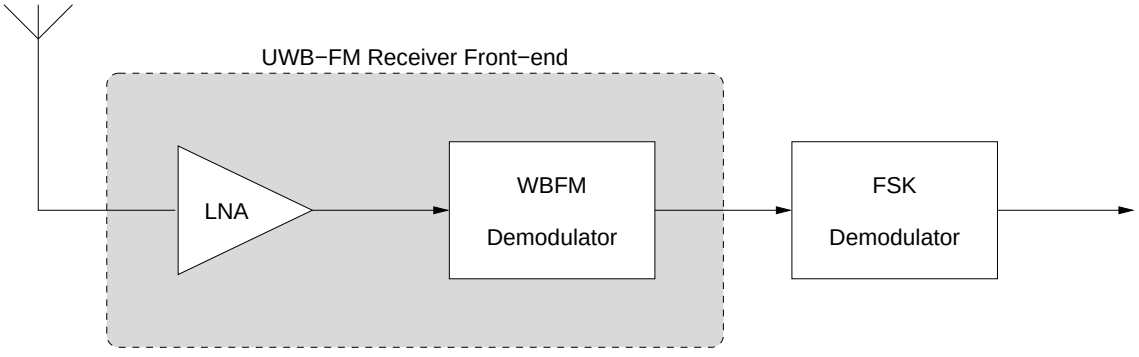

Figure 4.1: The top level block diagram of a UWB-FM receiver.

Parameter	Value
RF center frequency	4.5 GHz
RF bandwidth (-10 dB)	500 MHz

Table 4.1: RF frequency and bandwidth specification.

the receiver front-end.

Subsection 4.2.1 and 4.2.2 outline the input RF signal and the output subband signal characteristics. The receiver specification is calculated in Subsection 4.2.3 and concluded in 4.2.4.

4.2.1 RF Signal Characteristics

This subsection calculates the receiver input signal-to-noise ratio by considering the transmitting power, channel propagation, antenna gain and noise bandwidth.

4.2.1.1 Operating Frequency

The RF signal frequency and bandwidth are listed in Tab. 4.1.

UWB-FM systems utilize the 3-5 GHz frequency band with several multiple access schemes available. The two which have influence to the receiver architecture are listed below.

- RF FDMA, 500 MHz RF bandwidth, 3 RF bands from 3 to 5 GHz [27].
- Sub-carrier FDMA, 2 GHz RF bandwidth, 1 RF band from 3 to 5 GHz [28].

The reception of multiple subcarriers requires a certain linearity of a receiver front-end, because nonlinear distortion intermodulates subcarriers. The RF bandwidth for this project is 500 MHz, and only 1 subcarrier is carried in each RF channel. Therefore, the linearity requirement of our receiver front-end is relaxed.

4.2.1.2 Transmitting Power and Propagation

The transmitting power of an indoor UWB transmitter is limited by FCC regulation [29] to -41.3 dBm/MHz EIRP (Equivalent Isotropic Radiated Power), in the frequency range between 3.1 and 10.6 GHz. This rule sets a maximum transmitting carrier power of

$$P_T K_T = -41\mathrm{dBm/MHz} + 10\log\left(500\mathrm{MHz}\right) = -14\,\mathrm{dBm}, \tag{4.1}$$

where P_T is the transmitter power and K_T is the antenna gain at the transmitter side.

The path loss of the communication channel is defined as

$$PL\left(d\right) = \left(\frac{4\pi d}{\lambda}\right)^{n} \tag{4.2}$$

where d, λ and n are the distance, carrier wavelength and propagation exponent, respectively. For short-range, line-of-sight UWB applications, the propagation exponent seldom exceeds 2 [30]. In other words, transmission loss is often proportional to less than square of the distance. Assuming free space propagation, which has a propagation exponent of 2, we have the signal power at the receiver input of

$$P_R = \frac{P_T K_T K_R}{\left(4\pi d/\lambda\right)^2} \tag{4.3}$$

where K_R is the antenna gain at the receiver side.

UWB-FM receivers do not have particular antenna requirements. Commonly used omni-directional antennas provide a few dB gain (2.3 dB for a dipole antenna). But imperfect matching could cause several dB of loss. So, it is still sensible to assume the use of isotropic antennas at both ends of the channel. For a communication range of 10 meters, we have the signal power at the receiver input of

$$P_R = -14\text{dbm} - 20\log(\frac{4\pi \cdot 10\text{m}}{\frac{3\times10^8\text{m/s}}{4.5\times10^9\text{Hz}}}) = -80\text{dBm}. \tag{4.4}$$

4.2.1.3 Noise Power and SNR

The noise power at the receiver input is

$$N_R = -174\text{dbm} + 10\log(500\text{MHz}) = -87\text{dBm}. \tag{4.5}$$

The signal-to-noise ratio at the input is thus

$$SNR_i = P_R/N_R = -80\text{dbm} + 87\text{dbm} = 7\text{dB}. \tag{4.6}$$

4.2.2 Sub-band Signal Characteristics

UWB-FM reception involves an FSK demodulation of subband signals, which requires a certain SNR at the output of the front-end to work properly.

According to [27], the subband signal is specified in Tab. 4.2. In this project, we implement the maximum data-rate of 100 kbps.

Parameter	Value
Sub-carrier frequency	1 MHz
Sub-carrier modulation	FSK
Modulation index	$\beta_{FSK} = 1$
Data rate	20, 40, 100 kbps

Table 4.2: Sub-band signal characteristics.

4.2.2.1 Sub-band Signal Bandwidth

The modulation index of FSK is defined as the ratio of the maximum frequency deviation to the modulation frequency

$$\beta_{FSK} = \frac{2\triangle f}{f_m}. \tag{4.7}$$

The maximum frequency deviation and bandwidth of subband can be calculated as

$$\triangle f_{FSK} = \frac{1}{2}\beta_{FSK} f_m = 50 \text{ kHz} \tag{4.8}$$

and

$$BW_{FSK} = 4\Delta f_{FSK} = 200 \text{ kHz}. \tag{4.9}$$

4.2.2.2 SNR Requirement

For orthogonal BFSK modulation, and optimum detection (with a matched filter) we have the bit error rate

$$P_e = \frac{1}{2} erfc \sqrt{\frac{E_b}{2N_0}}, \tag{4.10}$$

where E_b/N_0 is the energy per bit to noise power density ratio. According to application analysis, a maximum bit error rate of 10^{-6} is required for low-data-rate (LDR) physical layer [31]. In that case, we need a E_b/N_0 of nearly 14 dB.

Finally, the link spectral efficiency can be calculated by

$$\frac{R}{BW_{FSK}} = 0.5, \tag{4.11}$$

and the signal-to-noise ratio needed from the output of WBFM demodulator is then

$$SNR_o = \frac{E_b}{N_0} \cdot \frac{R}{BW} = 14\text{dB} - 3\text{dB} = 11\text{dB}. \tag{4.12}$$

4.2.3 Receiver Front-end Specification

4.2.3.1 Noise Figure

From Equ. 4.6 and 4.12, the noise figure of the receiver front-end is

$$NF_{tot} = SNR_i - SNR_o = -4\text{dB}. \tag{4.13}$$

A negative noise figure is indeed possible in UWB-FM receivers, since the subcarrier bandwidth is significantly smaller than the RF bandwidth. Frequency-domain filtering can be applied after the RF front-end to distinguish signal from noise. The processing gain illustrating this property is

$$G_p = \frac{BW_{RF}}{BW_{FSK}} = \frac{500\text{MHz}}{200\text{kHz}} = 34\text{dB}. \tag{4.14}$$

Therefore, noise-figure headroom of 30 dB exists for LNA and FM demodulator when processing gain is taken into account.

4.2.3.2 Linearity

Non-linearity distortion jeopardizes the amplitude of a signal. For FM signals, since information is carried only on the frequency, they are immune to amplitude distortion. In practical FM systems, high-efficiency power amplifiers in transmitters and amplitude limiting device in receivers are commonly used although they do cause severe amplitude distortions.

Furthermore, the subcarrier in UWB-FM is FSK modulated, which does not require linearity either. Therefore, even the frequency discriminator in UWB-FM front-ends can be made nonlinear. This permits the use of integrators and super-regenerative oscillators as frequency-to-amplitude converters. FM-discriminators are discussed in Section 4.3.3.

4.2.3.3 Spurious Emission

This project involves the use of a super-regenerative oscillator as a detector which could produce considerable power in RF frequencies and has the potential to violate FCC or European power emission regulations. So an isolation specification should be imposed to LNA to prevent the oscillation from coupling back to antenna.

According to [32], narrow-band spurious emissions defined in effective isotropic radiated power (EIRP) for receivers should not exceed -47 dBm in frequency range from 1 GHz to 12.75 GHz.

Parameter	Value
RF center frequency	4.5 GHz
RF bandwidth (-10 dB)	500 MHz
Receiver Sensitivity	-80 dBm
Noise Figure	30 dB
Spurious Emissions (EIRP)	-47 dBm

Table 4.3: System-level specification for the UWB-FM receiver front-end.

4.2.4 Specification Summary

The system-level specification is summarized in Tab. 4.3.

4.3 The FM Demodulation Scheme

4.3.1 Indirect FM Detection

Information carried in frequency cannot be recovered directly [13]. An intermediate transformation has to be performed to convert an FM signal into either an AM or a PM signal. Then, the base-band signal can be reconstructed by a corresponding amplitude or phase demodulation.

The choice between the FM-AM and the FM-PM intermediate transformation involves a performance-complexity trade-off. All phase detection methods are synchronous. In other words, phase detection unavoidably involves a comparison between the incoming PM signal and a reference signal. Coherent detection offers the best performance at the cost of complexity and power consumption. On the other hand, amplitude demodulation can be either synchronous or asynchronous. Noncoherent amplitude detectors, such as square-law and peak detectors are commonly used for low-complexity receivers. The penalty paid for noncoherent detection is the lack of phase selectivity and thus a degraded dynamic range.

UWB-FM receivers target on low-complexity low-power applications. The noncoherent amplitude detection is clearly favored as long as the system specifications derived in Section 4.2 are satisfied. If the performance of the noncoherent detection is not adequate, the coherent amplitude detection can still be performed. Therefore, the FM-AM conversion scheme is chosen for this project.

The ideal FM-AM conversion is the differentiation of the FM signal to time. A frequency modulated sinusoidal carrier can be expressed as

$$s(t) = A\cos\left[\omega(t)\,t + \phi\right] \tag{4.15}$$

where A is the constant amplitude, ϕ is the constant initial phase and $\omega(t)$ is the instantaneous angular frequency as a function of time. The derivative of this FM

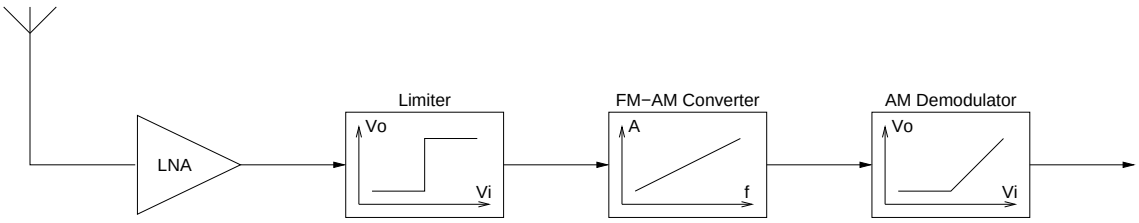

Figure 4.2: Block diagram of a generic FM-AM receiver.

signal is

$$\dot{s}(t) = -A\omega(t)\sin[\omega(t)t + \phi], \tag{4.16}$$

which has an amplitude variation being proportional to the instantaneous frequency.

A general FM-AM receiver structure is shown in Fig. 4.2. The 3 building blocks, namely, the limiter, frequency discriminator and AM detector are discussed in detail in the following subsections.

4.3.2 Limiter

An ideal FM signal has a constant amplitude. In reality, however, channel propagation induces amplitude noise. The effect of this noise can be derived by adapting Equ. 4.15 and 4.16 into

$$s_n(t) = A(t)\cos[\omega(t)t + \phi] \tag{4.17}$$

and

$$\dot{s}_n(t) = \dot{A}(t)\cos[\omega(t)t + \phi] - A(t)\omega(t)\sin[\omega(t)t + \phi]. \tag{4.18}$$

The first term in Equ. 4.18 is called the radial component, which carries no information but interference. The second term, named the tangential component, carries the information, but is contaminated by the amplitude noise. In order to eliminate the amplitude noise, amplitude limiters are frequently used before FM-AM converters to regulate the amplitude.

The consequences of amplitude limiting are controversial. On one hand, a limiter reduces amplitude noise. The total noise is partially discriminated and removed. On the other hand, the nonlinearity of the limiter reduces the dynamic range of the receiver as well. In other words, input signals are suppressed more than the noise. Thus, the net effect of amplitude limiting depends on the input SNR.

The relationship between the output and input SNR of an ideal UWB-FM demodulator is shown in Fig. 4.3. The performance of another demodulator used for commercial FM (20 kHz wide baseband and 75 kHz maximum frequency deviation) is also plotted as a comparison. From the figure, it can be observed that FM demod-

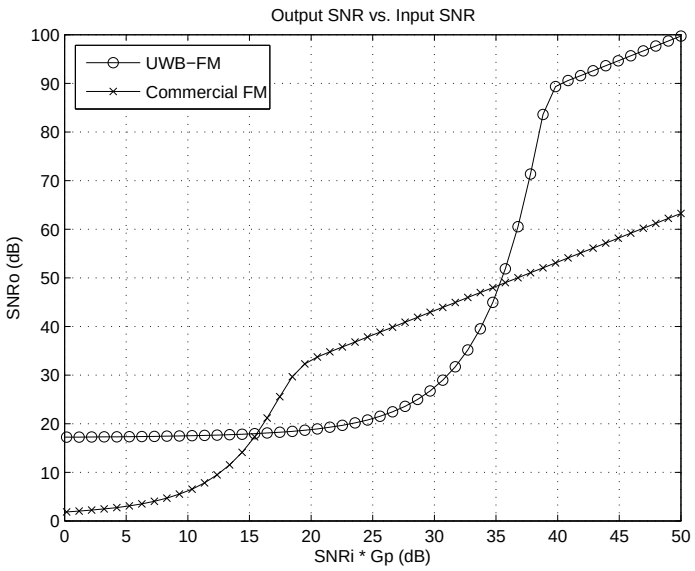

Figure 4.3: The threshold effect of FM detection.

ulators exhibit thresholds, below which the output SNRs degrade dramatically as the input SNRs decrease. If an FM receiver operates above the threshold, amplitude limiting yields improvement of output SNR. Conversely, if the input SNR is lower than the threshold, limiting the amplitude leads to a degradation of output SNR [13].

The UWB-FM demodulator to be designed has an input SNR of at least 7 dB and a processing gain of 34 dB, as derived in Equ. 4.6 and 4.14. This leads to an output SNR of around 90 dB. As shown in Fig. 4.3, the receiver is operating 1 dB above the threshold of the UWB-FM system. Therefore, for a UWB-FM receiver, the advantage and drawback of the amplitude limiter countervail each other. The net improvement or degradation of the output SNR is limited, if there is any.

According to the preceding analysis of the amplitude limiter, two design decisions are made. Firstly, the amplitude limiter is not going to be implemented in this receiver, since it is not effective for UWB-FM. Secondly, the nonlinearity of the LNA can be tolerated, since it has the same effect as an amplitude limiter. This nonlinearity is commonly considered to be harmful to the dynamic range of the receiver. However, for FM receivers, this distortion also suppresses the amplitude noise.

4.3.3 FM Discriminator

FM discriminators convert FM signals into AM-FM ones. Any circuit having a non-constant amplitude-frequency response can be used for this conversion. Frequency domain filters are the most common FM discriminators.

Discriminator Types A first order differentiator has a transfer function of

$$H(j\omega) = j\omega \tag{4.19}$$

which is an ideal FM discriminator in the sense that it converts frequency into amplitude *linearly*. Furthermore, when additive white Gaussian noise (AWGN) with a power spectral density of N_0 is applied to the signal, the output noise power is

$$N_{out} = |H(j\omega)|^2 N_0 = \omega^2 N_0 \tag{4.20}$$

which quadratically shapes the noise in such a way that low frequencies have low noise level. This noise shaping is the fundamental reason of the SNR improvement of FM systems [13].

A first order integrator has a transfer function of

$$H(j\omega) = \frac{1}{j\omega} \tag{4.21}$$

which converts frequency *nonlinearly*. For AWGN with a power spectral density of N_0, the output noise power is

$$N_{out} = |H(j\omega)|^2 N_0 = \frac{N_0}{\omega^2} \tag{4.22}$$

which shapes the noise in a wrong way that the noise power is concentrated in the low-frequency band. Although it has nonlinearity and inferior SNR performance, it is used more often than differentiators because it requires fewer components. An LC tank is a typical integrator being biquadratically transformed from low-pass to band-pass form.

Super-regenerative oscillators themselves have nonuniform frequency responses. Slope-controlled SROs has a frequency response shaping as a Gaussian curve, as shown in Equ. 3.63. The frequency response of the step-controlled SROs is similar to the response of a pair of loosely coupled tuned circuits [3], as shown in Equ. 3.65. These gain variations as a function of frequency can be exploited to do the FM-AM conversion. However, both of the shapes are nonlinear and the noise is also shaped in a wrong way.

Since a super-regenerative oscillator is going to be used for amplification, it is straightforward to exploit its frequency response to convert FM into AM without extra components, unless its inferior noise performance is intolerable.

Tuned Filters Vs. Detuned Filters Tuned differentiators and integrators convert FM signals into double-sideband (DSB) AM *without* a carrier. Tuned super-

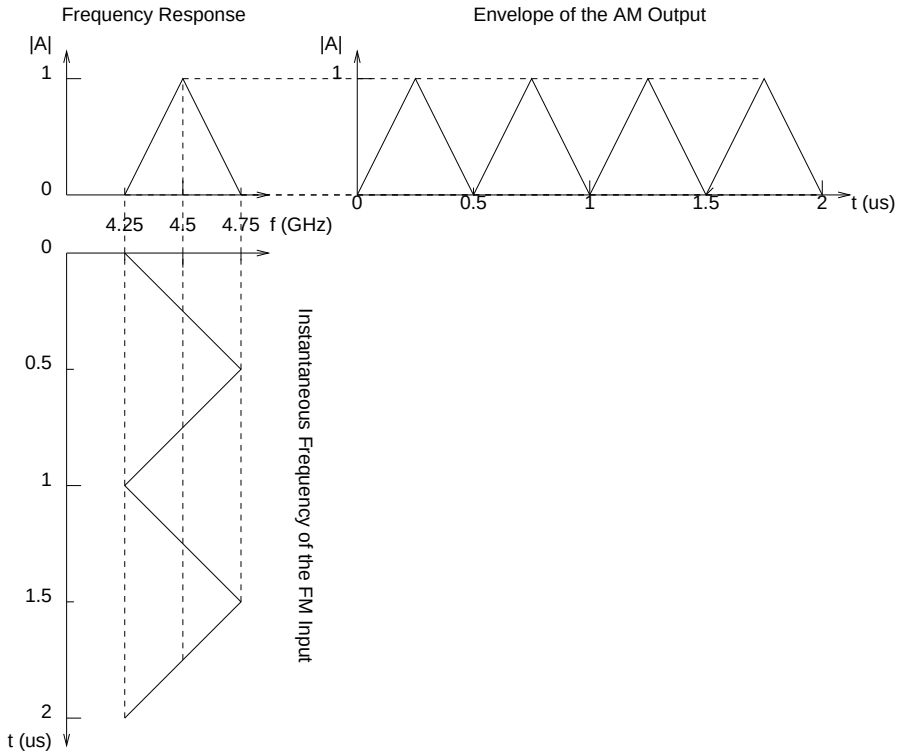

(a) Tuned FM-AM conversion.

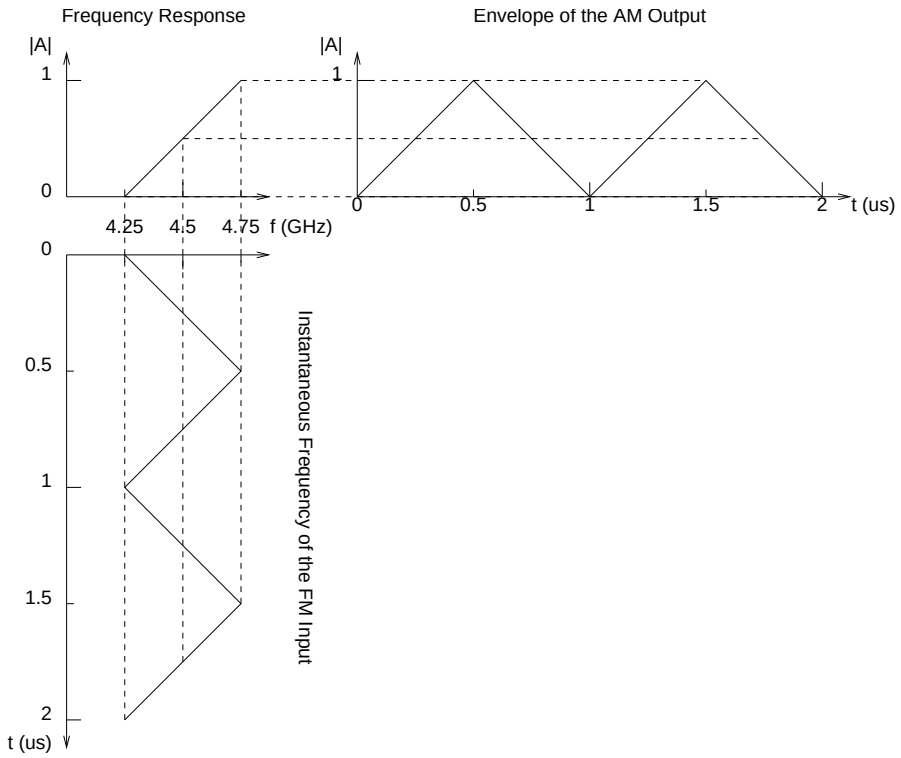

(b) Detuned FM-AM conversion.

Figure 4.4: Tuned and detuned FM-AM conversion.

regenerative oscillators act as FM-AM converters followed by full-wave rectifiers, since their frequency responses are not monotonic within the FM bandwidth. The FM-AM conversion effect of a tuned filter is illustrated in Fig. 4.4 (a). If the following stage is a noncoherent AM detector, none of these signals can be correctly demodulated.

The common remedy to tackle this problem is to detune a filter (or an SRO) away from the center frequency of an FM signal in such a way that the amplitude response of the filter is monotonic within the frequency band of interests, as shown in Fig. 4.4 (b). The penalty paid is that half of the filter bandwidth is opened to no signal but noise.

In this design, we exploit a special property of the UWB-FM modulation scheme, so that a tuned filter (or SRO) and a noncoherent AM detector can be used together. Since the signal to be recovered is an FSK modulated signal which carries information only on its frequency, not on its amplitude, the information carried in the frequency can be recovered, although a full-wave rectifier distorts the amplitude heavily and doubles the frequency. More specifically, as shown in Fig. 4.4 (a), a 1 MHz triangular subcarrier is recovered as a 2 MHz triangular wave; a 0.9-1.1 MHz FSK modulated signal is recovered as a 1.8-2.2 MHz FSK modulated signal.

4.3.4 AM Demodulator

AM detection can be synchronous or asynchronous. Asynchronous, or noncoherent, detectors retrieve the amplitude modulus of the AM signal. The modulus of the FM-AM-converted signal (Equ. 4.18) has an amplitude modulus of

$$V_{mod} = \|\dot{s}_n(t)\| = \sqrt{\dot{A}^2(t) + A^2(t)\,\omega^2(t)}. \tag{4.23}$$

Synchronous, or coherent, detectors produce the projection of the AM signal on a reference signal. Defining the reference signal as

$$r(t) = -B\sin(\omega t + \phi), \tag{4.24}$$

the projection of the AM signal on this reference signal is then

$$V_{prj} = \dot{s}_n(t)\,r(t) + \dot{s}_{nq}(t)\,r_q(t) \tag{4.25}$$

where $\dot{s}_{nq}(t)$ and $r_q(t)$ are the quadrature of $\dot{s}_n(t)$ and $r(t)$, defined as

$$\dot{s}_{nq}(t) = \dot{A}(t)\sin[\omega(t)\,t + \phi] + A(t)\,\omega(t)\cos[\omega(t)\,t + \phi] \tag{4.26}$$

$$r_q(t) = B\cos(\omega t + \phi). \tag{4.27}$$

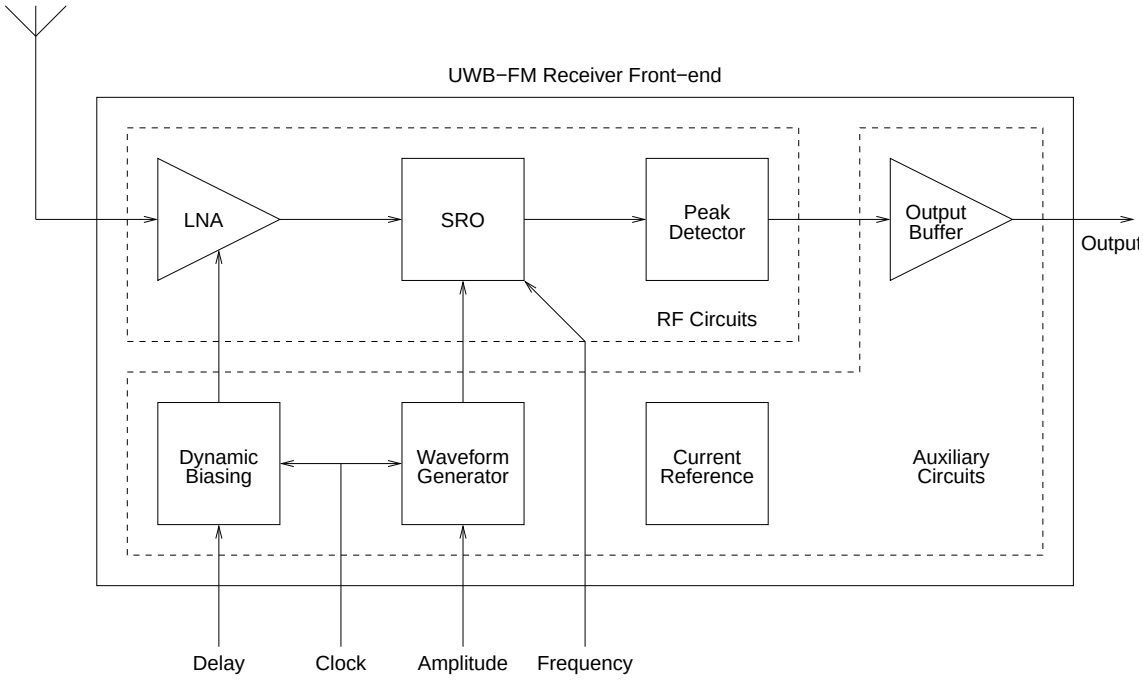

Figure 4.5: Block diagram of the super-regenerative receiver for UWB-FM.

Substituting Equ. 4.18, 4.24, 4.26 and 4.27 into Equ. 4.25 yields

$$\begin{aligned} V_{prj} &= -\left(\dot{A}\cos - A\omega\sin\right) B\sin + \left(\dot{A}\sin + A\omega\cos\right) B\cos && (4.28)\\ &= -\dot{A}B\sin\cos + AB\omega\sin^2 + \dot{A}B\sin\cos + AB\omega\cos^2 && (4.29)\\ &= AB\omega && (4.30) \end{aligned}$$

Comparing Equ. 4.23 and 4.30, coherent detection can distinguish the amplitude noise from signal while the noncoherent detection cannot. This drawback for noncoherent detectors is intrinsic since they do not have a phase reference.

Coherent detectors, although provide the best achievable performance [13], are power consuming since at least one multiplier is necessary for the projection calculation. Synchronization dissipates extra power if a local oscillator is used to produce the reference signal.

In this design, the AM demodulation is performed by the simplest form of noncoherent detectors, a peak detector, for its structural simplicity and low power consumption. Its inferior noise performance is partially made up by the high gain of the SRO in front of it.

4.4 Receiver Architecture

The block diagram of the super-regenerative receiver is shown in Fig. 4.5. The RF part of the receiver, consisting of an LNA, an SRO and a peak detector, originates

from the generic FM receiver plotted in Fig. 4.2. The LNA suppresses the noise of following stages, matches the impedance of the antenna for maximum power transmission and shields the high-power oscillation of SRO from coupling back into the antenna. The SRO provides most of the receiver gain and converts the incoming FM signal into AM. The peak detector extracts the envelope of the periodically building-up oscillations as the output signal.

The auxiliary circuits consist of a waveform generator, a dynamic biasing circuit, an output buffer and a current reference. The waveform generator produces a certain biasing waveform to bias the SRO for a certain frequency response. The dynamical biasing circuit shut the LNA down in the quenching period of SRO to save power. The output buffer drives the measurement instrumentation. And the current reference provides biasing for all on-chip circuits.

The receiver is designed to be flexibly configurable. Four external control signals are accepted. The "clock" and the "amplitude" signals adjust the time-constants and amplitude of the quenching waveform. The "delay" signal controls the warm-up time of the LNA before the SRO starts to work. The "frequency" signal tunes the oscillation frequency of the SRO.

4.5 System-level Simulation

The objective of the system-level simulation is to verify the theory discussed in Chapter 3 and the feasibility of the UWB-FM super-regenerative receiver discussed in this chapter.

The simulation method is the numerical integration of a nonlinear time-varying dynamical model of the super-regenerative receiver stimulated by an UWB-FM signal. Mathworks Simulink is used to perform these simulations.

The top-level simulation setup is shown in Fig. 4.6. A 4.5 GHz, 500 MHz bandwidth WBFM signal modulated by a 1 MHz triangular subcarrier is the excitation of the receiver. The "Channel" block representing a 10-meter propagation attenuates the signal to -80 dBm at 100 ohm resistance as specified in Equ. 4.4. The spectrum of the signal at the input of the receiver is plotted in Fig. 4.7.

The three blocks shown at the bottom of Fig. 4.6, namely the "GM", "sro" and "PeakDetector", model the LNA, SRO and peak detector in a receiver. Block "Ga" provides a rectangular quenching waveform. The purpose of the feedback from the output of the peak detector to the input "amp" of the SRO is to model the amplitude limiting nonlinearity of the SRO.

The model of the SRO is plotted in Fig. 4.8. It is described by the second order time-varying differential equation 3.2 modeling the circuit shown in Fig. 3.1. In addition, the nonlinearity is also modeled by the look-up table, so reduction of

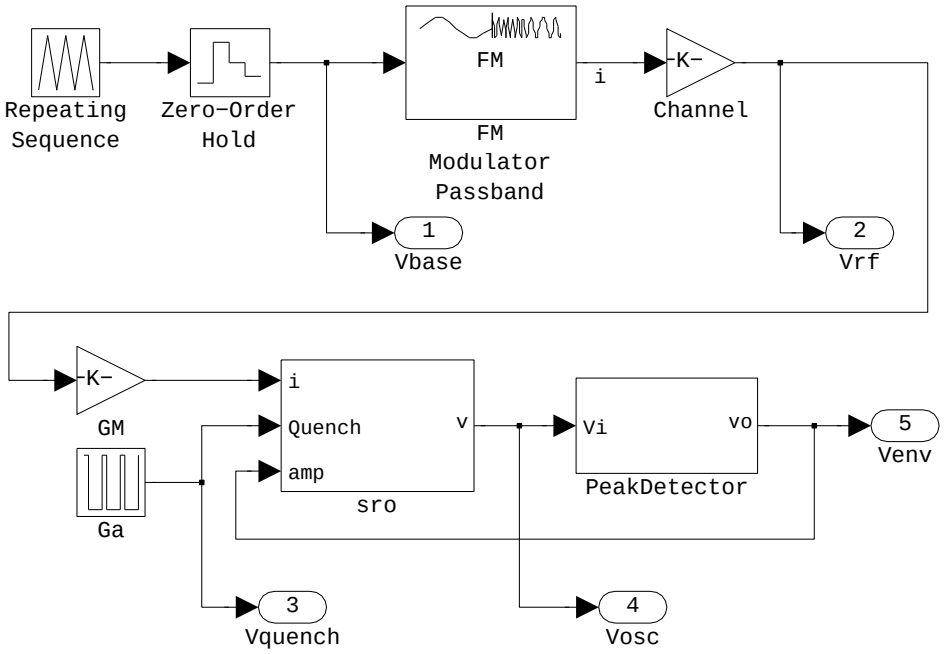

Figure 4.6: Top-level simulation setup.

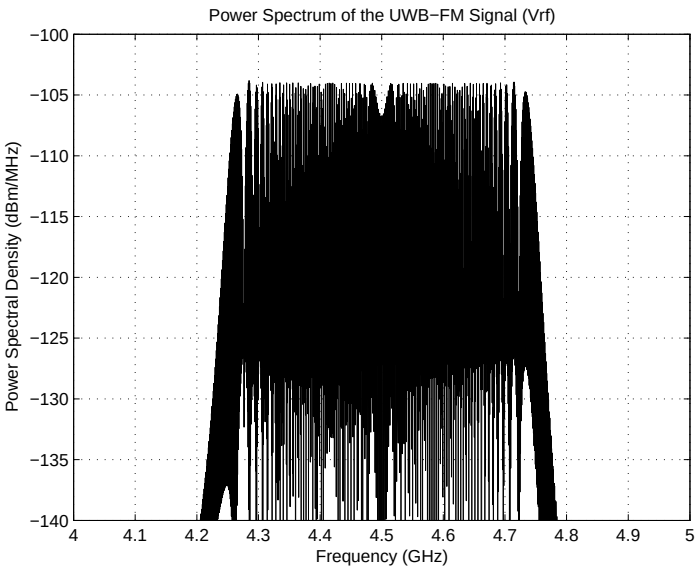

Figure 4.7: The spectrum of the UWB-FM signal at the input of the receiver.

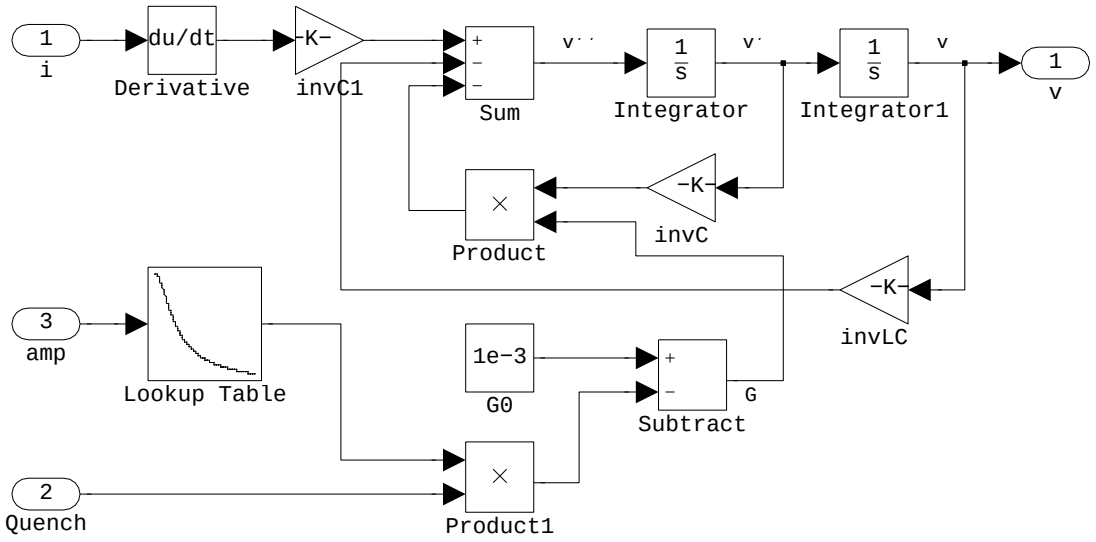

Figure 4.8: The nonlinear time-varying model of the SRO.

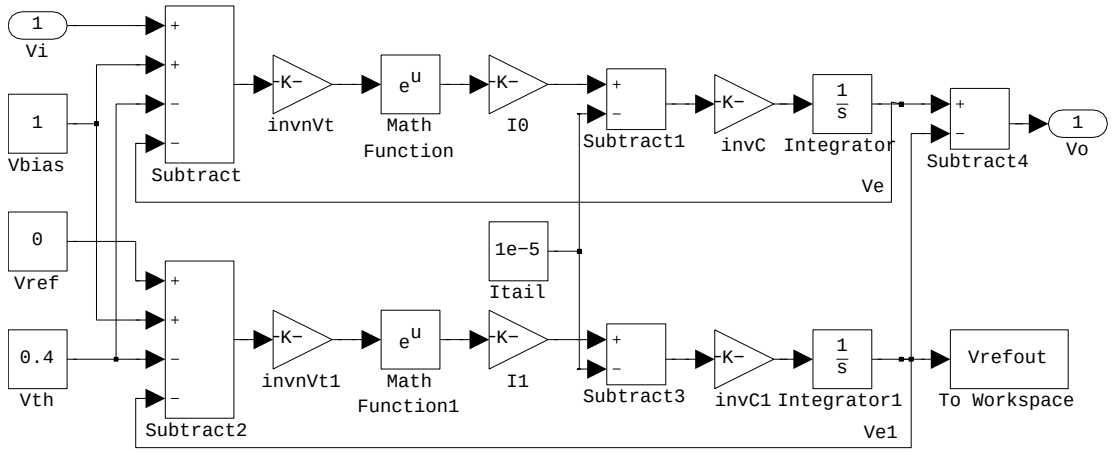

Figure 4.9: The peak detector model.

negative conductance can be modeled when the oscillation amplitude increases.

The peak detector block, shown in Fig. 4.9, models the simplest peak detector, formed by a diode, a capacitor and a current source. Despite its structural simplicity, the correct operation relies on the dynamic nonlinearity of the circuit. In essence, this block implements the implicit equation

$$V_E = \frac{1}{C}\int_0^t \left[I_0 \exp\left(\frac{V_B + V_i - V_E}{V_T}\right) - I_{tail} \right] \mathrm{d}t. \tag{4.31}$$

In every integration step, V_E is calculated by this equation and the output of the peak detector is given by

$$V_o = V_E - V_{E1}. \tag{4.32}$$

The simulation result is shown in Fig. 4.10. As shown in the graph, the restored subcarrier is a pulse-amplitude-modulated version of the actual signal. Its frequency (and presumably the FSK modulation index) is doubled as predicted in Subsection 4.3.3.

Intensive simulations are performed to verify that the gain, output pulse shape and frequency response of the receiver are adjustable by tuning the amplitude, duty-cycle, frequency and the shape of the quenching waveform.

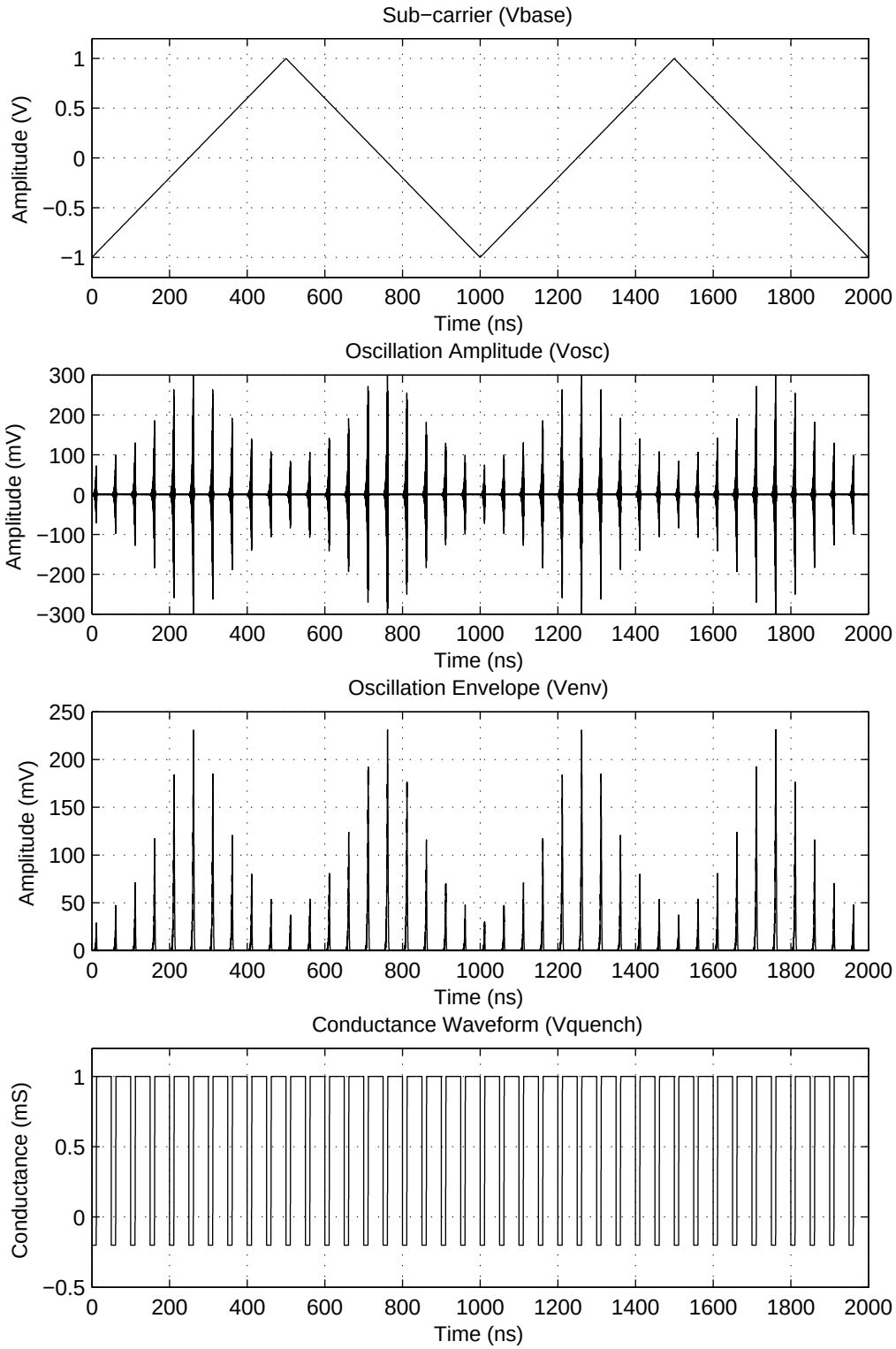

Figure 4.10: The simulated baseband signal, oscillations, their envelopes and the quenching waveform.

Chapter 5

Receiver Circuit Design

5.1 Introduction

In Chapter 4, receiver specifications are derived and a block-level receiver structure is proposed. The design and implementation of the RF building blocks, namely the super-regenerative oscillator, the peak detector and the low-noise amplifier, utilizing IBM 90-nm CMOS technology are present in this chapter.

Since a detailed specification for each circuit block is not available at the beginning, we follow a specific design procedure. First, the super-regenerative oscillator and the peak detector are designed to realize the receiver functionality with minimal power dissipation. Then, we use the noise and swing information of these stages to determine the LNA specifications, namely the gain, noise figure and reverse isolation. After the LNA is worked out, quenching generators for SRO and LNA are designed without influencing the receiver performance. Finally, we implement the output buffer stage and the on-chip current reference.

The super-regenerative oscillator, peak detector and low-noise amplifier are introduced in Section 5.2, 5.3 and 5.4, respectively. The other building blocks, namely the biasing waveform generator for SRO, the dynamic biasing circuit for LNA, the output buffer and the current reference are introduced in Chapter 6.

5.2 Super-regenerative Oscillator

5.2.1 Design Objective

The design goals for this super-regenerative oscillator are to provide maximal gain in RF frequency, correct frequency response to convert FM into AM and to consume minimal power. Maximal gain of SRO is desirable because firstly, it shields the receiver back-end from jeopardizing system sensitivity, and secondly, the gain of this stage is cheaper than that of an LNA.

5.2.2 Resonator Selection

Resonators are frequency selective elements used in oscillators. The quality of resonators directly influences the noise and power consumption of SROs.

Generally speaking, off-chip discrete passives offer considerably better performance. Nevertheless, we avoid using them as resonators for the following reasons. First of all, the use of off-chip components increases the component count and decreases the integration level. These lead to an increased production cost which is unfavorable for low-complexity low-cost UWB-FM applications. Secondly, off-chip components are susceptible to parasitics caused by packaging and mounting. These parasitics can be prohibitively large and even worse, difficult to control. Therefore, in this project, we prefer integrated passives.

Commonly used resonators in the literature include LC tanks, distributed elements, quartz crystals, SAW devices and recently, BAW devices.

Quartz crystals and SAW devices have been the choice for high-performance narrow-band SROs since their high quality factor solves the inherent low-selectivity and frequency-instability problems of super-regenerative receivers. However, these devices are incompatible with silicon technology and normally incapable of operating at frequencies upper than 2 GHz.

BAW devices also have high Q factors and they can work at UWB frequencies. Nonetheless, they need special MEMS fabrication processes or sophisticated wafer-bonding technologies, which are commonly unavailable.

Distributed elements can be used as resonators such as quarter-wave lines, which are commonly used in microwave oscillators. With high permittivity dielectrics, transmission lines are also high-Q devices. However, physical dimensions of transmission lines are normally unfavorable for integration. For instance, 4.5 GHz signals have a wavelength of 67 mm in vacuum. A quarter-wave line with pure silicon as the dielectric would have a length of $67/\sqrt{\varepsilon_{r-sillicon}}/4 = 4.9$ mm.

LC tanks are the oldest type of filters used in SROs, originating from Armstrong's patent in 1922. They have been the most popular choice because of the abundance of discrete inductors and capacitors. However, integrated passives, especially inductors, suffer from the low Q caused by the resistance of metals and substrate coupling.

In conclusion, despite their high-loss, integrated lumped components are the best choice with respect to fabrication cost and technology.

5.2.3 The Schematic

The schematic of the super-regenerative oscillator is plotted in Fig. 5.1. Its topology is identical with a classical NMOS negative-GM oscillator. Transistors M1 and M2 are biased by the tail current source M3 to generate a negative conductance in

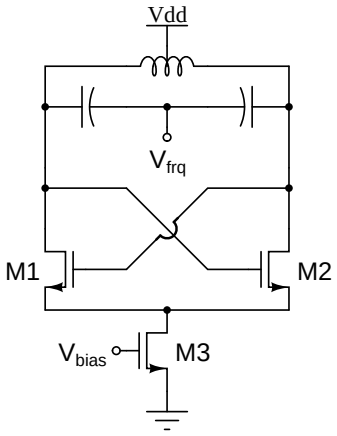

Figure 5.1: The schematic of the super-regenerative oscillator.

parallel with the LC resonation tank. A periodic biasing current yields a periodically varying negative conductance, which causes the super-regeneration, mathematically interpreted in Chapter 3.

A differential oscillator structure is chosen for 3 reasons. First of all, it does not consume more power than a single-ended one, for a given voltage swing. However, it is capable to oscillate at an amplitude twice as much as a single-ended version, for a given voltage supply. This characteristic is especially favorable to low-power designs because supply voltage can be lowered without influencing the voltage swing. Secondly, a symmetrically driven inductor demonstrates a higher Q factor. As will be discussed in Subsection 5.2.6, enhanced Q factor yields power and noise reduction of oscillators. The latter one further leads to LNA power reduction. Thirdly, common-mode noise can be rejected.

5.2.4 Biasing Waveform

According to Chapter 3, biasing waveforms control the oscillation envelope and frequency response of super-regenerative oscillators. Being more specific, the positive to negative conductance transitions decide the shape of frequency response and the negative to positive ones control the shape of oscillation envelope.

Moreover, the operation states of an SRO can be categorized into two types, determined by its biasing waveform. The transitions of conductance polarity are gradual for a slope-control and sharp for a step-control, as shown in Fig. 3.2 and 3.3.

In this subsection, we examine the alternative frequency responses and pulse shapes, select the most favorable combination for the low-power UWB-FM demodulation and design the favored biasing waveform for the SRO.

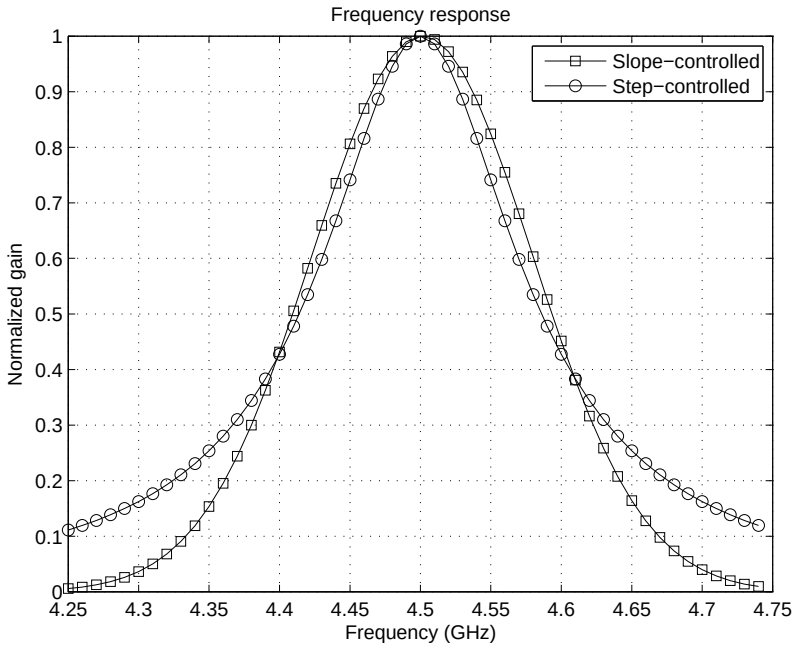

Figure 5.2: Frequency responses of slope- and step-controlled SROs.

5.2.4.1 Frequency Response

When the conductance transitions from positive to negative are slope-controlled, the sensitivity curve of an SRO has a Gaussian shape (Equ. 3.46), whose Fourier transform is also Gaussian shaped (Equ. 3.63). On the other hand, step-controlled conductance transitions from positive to negative yield sensitivity curves as double-sided decaying exponential functions (3.48), whose Fourier transform is shown in Equ. 3.65. The frequency responses of these two types of quenching are shown in Fig. 5.2.

The bandwidth of the frequency response is tunable for both slope- and step-controlled SROs. A larger slope, or a more negative conductance yields a sharper sensitivity curve and a flatter frequency response, and vice versa.

In our UWB-FM receiver, we choose to use the slope-control. Our motivation is discussed in the following paragraphs.

Since the frequency response of the SRO is used for FM to AM conversion, the one with the maximum conversion gain is preferred. Direct observation of Fig. 5.2 may not lead to the correct conclusion because the curve shapes are adjustable. A meaningful comparison should be made when both of them are tuned to their best performance. So, we perform the bandwidth optimization in the following 3 paragraphs.

We use the slope factor α, the changing rate of conductance, in Equ. 3.63 as the tuning variable for slope-controlled SROs. A set of frequency response curves are generated as shown in Fig. 5.3, when α ranges from 10^5 to 10^6 Siemens per

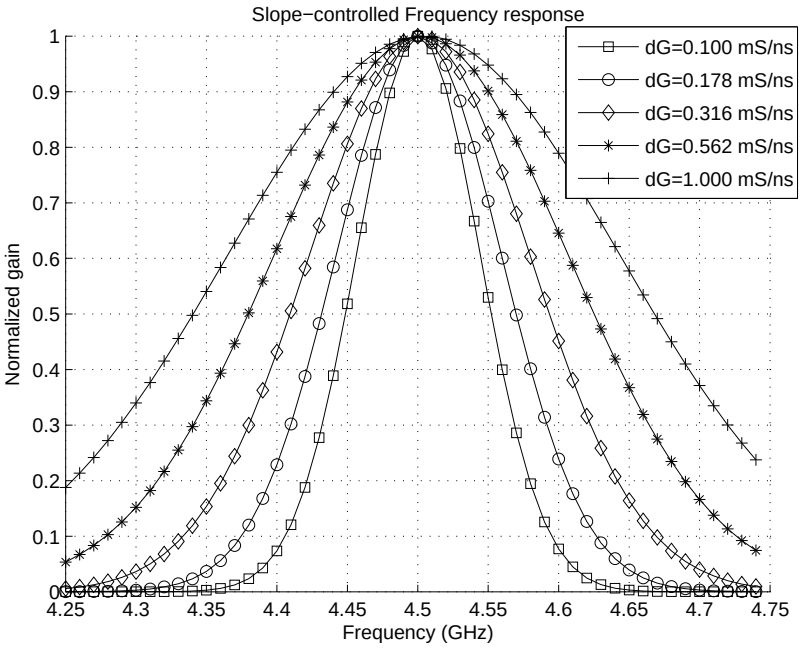

Figure 5.3: The optimization of slope-controlled frequency response.

second (S/s). If we apply the UWB-FM signal (triangular wave modulated) to such FM-AM conversion curves and change the horizontal axis to time, the curves would represent exactly 1 period of the waveform in time.

The first-harmonic amplitudes of these AM waves can be calculated by

$$A_{slope} = \frac{1}{\pi} \int_{-\pi}^{\pi} f(\theta) \cos\theta \mathrm{d}\theta \tag{5.1}$$

where $f(\theta)$ and θ are the AM waves and their phase. A parameter sweep shows that the best FM-AM conversion curve is obtained when $\alpha = 0.359 \times 10^6$ S/s, or 0.359 mS/ns, and the normalized output amplitude is 0.485.

We perform the same procedure to step-controlled SROs by using $-G_1$, the negative tank conductance as the sweeping parameter. A G_1 ranging from 100 uS to 3 mS yield the frequency response curves shown in Fig. 5.4. Applying Equ. 5.1 to this set of curves, we obtain the best FM-AM conversion curve when $-G_1 = -0.681$ mS. The normalized output amplitude is 0.387.

The comparison of best conversion gain of slope- and step-controlled SROs are listed in Tab. 5.1. The theoretically best conversion gain, 0.5, is also listed as a reference. It is provided by a cosine shaped curve with 250 MHz bandwidth.

It can be observed from Tab. 5.1 that slope-controlled SROs offer a nearly optimum frequency response. Therefore, we use a slope-controlled start-up for the SRO.

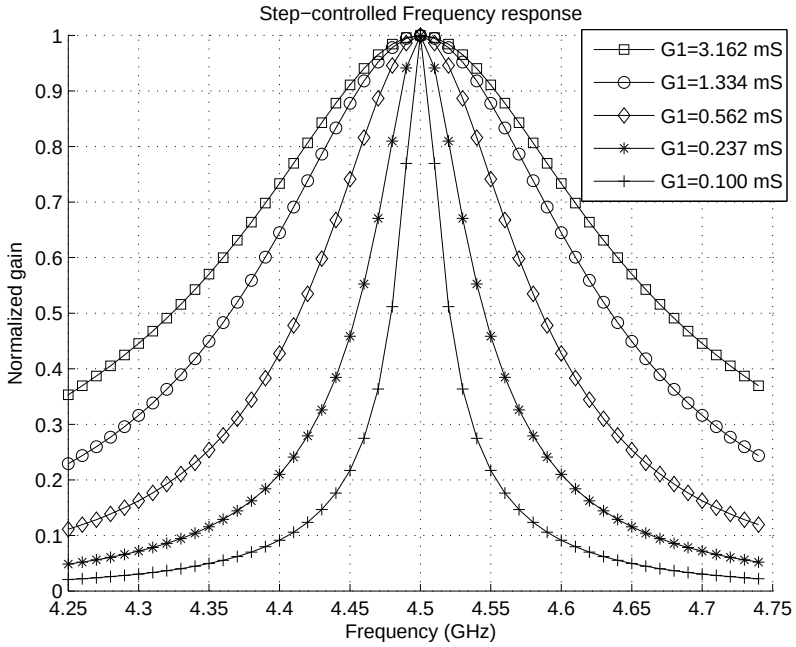

Figure 5.4: The optimization of step-controlled frequency response.

SRO Type	Freq. Resp. Curve	Max. FM-AM Conv.	Condition
Slope-cntl	Gaussian	0.485	$\alpha = 0.359\,\mathrm{mS/ns}$
Step-cntl	Equ. 3.65	0.387	$-G_1 = -0.681\,\mathrm{mS}$
Ideal	Cosine	0.5	$BW_{-3dB} = 250\,\mathrm{MHz}$

Table 5.1: The comparison of FM-AM conversion gain of slope-, step-control and the ideal case.

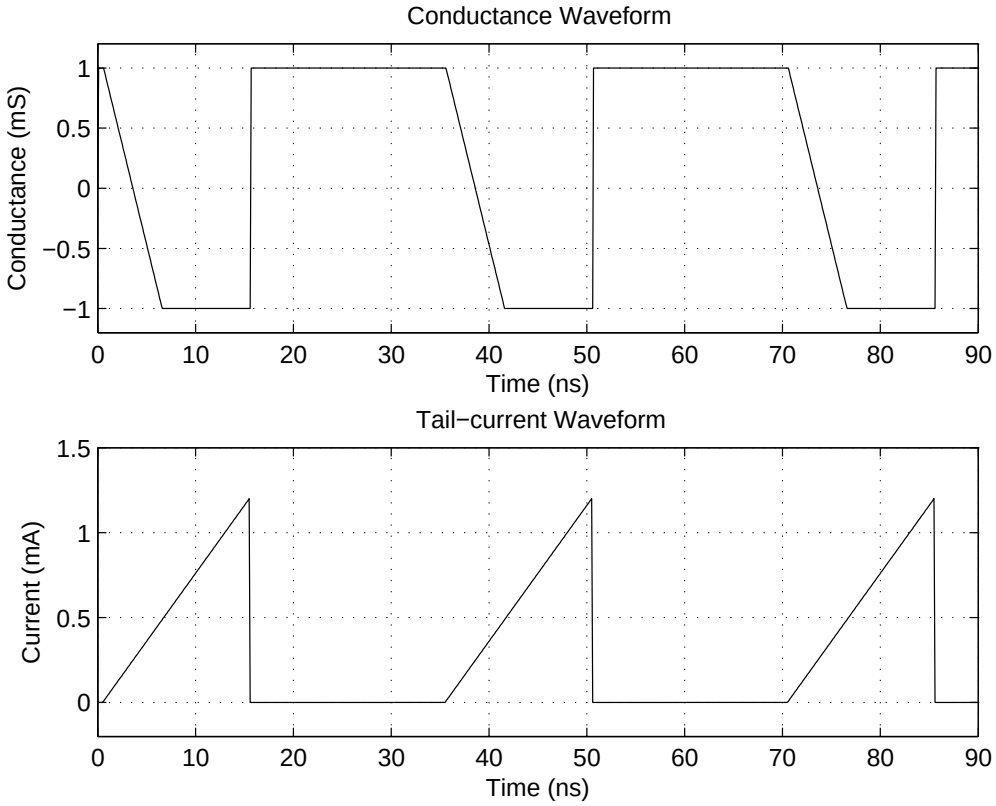

Figure 5.5: The waveform of the total conductance and the tail current for the SRO.

5.2.4.2 Oscillation Envelope

When the conductance transitions from negative to positive is slope-controlled, the oscillation envelope of an SRO has a Gaussian shape (3.50), as shown in Fig. 3.2. On the other hand, step-controlled conductance transitions from negative to positive yield exponential growing and decaying envelope (Equ. 3.51), as shown in Fig. 3.3.

A step-controlled quenching is preferred, because the peak oscillation amplitude appears when the biasing current is maximum. For a slope-controlled quenching, the peak amplitude happens when the conductance polarity is changing. At this time, the biasing current is not maximum, which may lead to gain compression and reduced dynamic range.

5.2.4.3 Tank Conductance and Biasing Current Waveform

A slope-controlled start-up and a step-controlled quenching yield a saw-tooth-like waveform. The designed conductance waveform is plotted in Fig. 5.5. In the figure, the slope of the positive to negative conductance transition is set to 0.359 mS/ns according to Tab. 5.1.

The conductance waveform can be efficiently generated by a saw-tooth current

source. The waveform of this source is shown in Fig. 5.5. The maximum current is 1.2 mA determined by the voltage swing requirement and the passive tank resistance. The current ramp takes 15 ns, this implies a current slope of 0.08 mA/ns.

At the starting-up phase, MOSFETs of the cross-coupled pair are in weak inversion, the negative transconductance provided by the pair is

$$-GM = -\frac{1}{2}g_m = -\frac{1}{2}\frac{I_d}{nV_T} = -\frac{1}{4}\frac{I_{tail}}{nV_T} \tag{5.2}$$

where g_m, I_d and n are the small-signal transconductance, drain current and slope factor of one transistor, and V_T is the thermal voltage. So before transistors M1 and M2 shown in Fig. 5.1 are saturated, the negative conductance is proportional to the biasing current. The IBM 90-nm NMOS we used has a slope factor, n, of 1.37. So in this linear region, the conductance slope is calculated by

$$\alpha = \frac{0.08 \text{ mA/ns}}{4 \times 1.37 \times 26 \text{ mV}} = 0.561 \text{ mS/ns}. \tag{5.3}$$

As the current grows larger, the I-V relation deviates from the exponential law. The absolute value of the conductance slope is becoming smaller and smaller. The critical point happens at this phase. When I_{tail} reaches 340 uA, the positive-to-negative transition of the conductance occurs. Ideally, at this critical point, the conductance slope should be 0.359 mS/ns.

When current grows large, the I-V behavior of pair transistors is more and more close to the square law. Then the negative transconductance is more accurately approximated by

$$-GM = -\frac{1}{2}g_m = -\frac{1}{2}\sqrt{2KI_d} = -\frac{1}{2}\sqrt{KI_{tail}}, \tag{5.4}$$

where $K = \mu C_{ox}{}^{W}/_{L}$. From this equation, we can determine the width of the MOSFETs. First of all, the width influences the gain of the SRO. A larger width yields a larger -GM and thus a larger negative area below this -GM curve. Secondly, the width affects the position of the critical point. A smaller width yields a comparatively higher current density and thus an early transition and a longer square-law region.

We select the width based on the amount of gain needed. For a given input RF signal strength, specific LNA gain and output oscillation amplitude, the gain of the SRO is a determinable constant. Since the maximum biasing current is set by the voltage swing, the slope is fixed by the frequency response, only width is adjustable to provide the specific amount of amplification. As a result, we determine the transistor width to be 12 um.

When the receiver needs the gain control, for example, when a communication

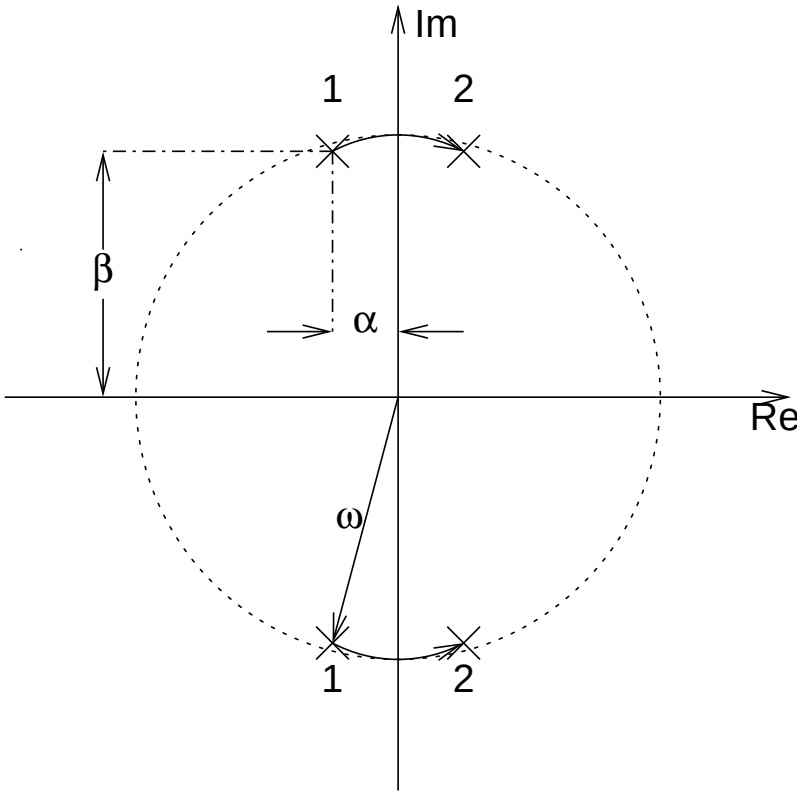

Figure 5.6: Pole positions of an SRO.

range is smaller than the maximum designed distance, then a smaller gain is still attainable after fabrication by slightly tuning the maximum current or the rise-time of the ramp. These adjustments detune the frequency response and the oscillation amplitude from their optimum values. But since decreasing the gain implies that a shorter communication distance and a better input SNR are available, the receiver performance is not degraded.

The GM compression effect shown in Equ. 5.4 is actually desirable. The reasons are explained in the following 2 paragraphs.

First of all, the absolute conductance has an upper bound for certain frequency stability. Equ. 3.15 in Chapter 3 is a high-Q assumption we made to simplify a parametric oscillator response into a free oscillation. Its graphical representation is shown in Fig. 5.6. A passive resonant tank has a pair of conjugate poles at position 1, and negative conductance moves poles to position 2 to start an oscillation. The parameters

$\omega_0 = \frac{1}{LC}$ is the natural oscillation frequency,

$\alpha = \frac{G_0 - G_1(t)}{2C}$ is the damping factor, and

$\beta = \sqrt{\omega_0^2 - \alpha^2}$ is the damped oscillation frequency.

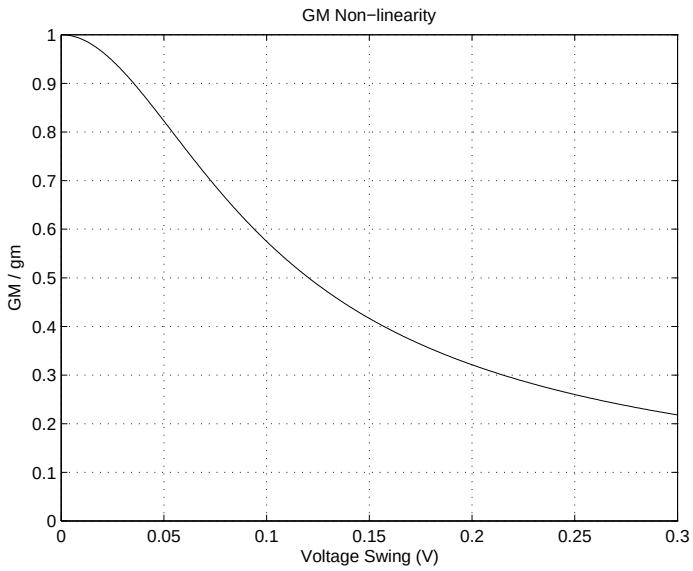

Figure 5.7: Negative GM nonlinearity.

When Equ. 3.15 is satisfied, the damping oscillation frequency is approximately the natural frequency, i.e.

$$\beta \approx \omega_0. \tag{5.5}$$

If the negative GM is too large, however, Equ. 5.5 does not hold any more. Then frequency stability is jeopardized.

Secondly, the tail current has a lower bound for certain voltage swing, since the voltage swing across a resonant tank is linearly proportional to the biasing current,

$$V_{sw} \propto R_{tank} I_{tail}. \tag{5.6}$$

In conclusion, we desire a certain slope-controlled conductance waveform across the resonant tank to provide an optimum frequency response for FM-AM conversion. Current biasing is suitable to generate this waveform for 2 reasons. Firstly, when MOSFETs are in weak inversion, the negative conductance is linearly proportional to biasing current. Secondly, when the MOSFETs are saturated, the negative conductance is weakly dependent on biasing current (they have a square-root relationship, as shown in Equ. 5.4), which relaxes the trade-off between frequency stability and voltage swing.

5.2.5 Dynamic-range Power Trade-off

In Subsection 5.2.4, we propose the current waveform, which has a maximum of 1.2 mA. This value is a trade-off between the dynamic range and the power consumption. All previous analysis assumes a linear time-varying negative conductance. However,

the practical negative conductance generated by a cross-coupled pair is oscillation-amplitude dependent. A curve showing this nonlinearity is plotted in Fig. 5.7. Oscillators utilize this nonlinearity as the automatic amplitude control mechanism.

Super-regenerative oscillators have 2 operation modes, the linear and the logarithmic mode. The latter one is normally undesirable because it performs the dynamic range compression. Intuitively, in logarithmic mode, large signals have smaller gain than that of small signals and noise. So the SNR at the output is inherently reduced, even if the amplification is noiseless. The gain compression caused by GM nonlinearity also has this undesirable dynamic-range compression effect.

The solution to prevent the dynamic-range compression is to increase the power dissipation. A larger biasing current leads to a larger available voltage swing, and more linear gain when the swing is small.

The maximum biasing current is determined based on this trade-off. Intensive simulations are performed with the biasing current gradually increased from a small value, until an acceptable output SNR is obtained. In this way, certain amount of gain nonlinearity is tolerated and minimum power consumption is guaranteed.

5.2.6 The Inductor

5.2.6.1 Inductor Design Objective

Our design goal for the SRO is to reduce power consumption. For an RLC resonant tank the dissipated power is expressed as

$$P_{loss} = \frac{\omega_0 E_{tank}}{Q} \tag{5.7}$$

where ω_0, E_{tank} and Q are the resonant frequency, energy stored in the tank, and the quality factor. In order to reduce power dissipation, we could either increase Q or decrease E_{tank}. However, the latter method reduces the oscillation voltage swing as well, since E_{tank} can be further expressed as

$$E_{tank} = \frac{1}{2} C V_{sig}^2 \tag{5.8}$$

where C is the tank capacitance and V_{sig} is the voltage across the capacitor. The minimal oscillation amplitude is determined by the noise

$$\overline{V_n^2} = \frac{kT}{C}, \tag{5.9}$$

and an SNR requirement

$$SNR = \frac{\overline{\left(V_{sig}/\sqrt{2}\right)^2}}{\overline{V_n^2}} = \frac{E_{tank}}{kT}, \tag{5.10}$$

where k and T are the Boltzmann's constant and absolute temperature. A clear power SNR trade-off is obtained by combining Equ. 5.7 and 5.10

$$\frac{SNR}{P_{loss}} = \frac{Q}{\omega_0 kT}. \tag{5.11}$$

Since $\omega_0 kT$ is practically a constant, if we want high SNR and low power consumption, maximizing the Q factor is the ultimate way.

5.2.6.2 Inductor Selection

In IBM 90-nm RF CMOS design library, a scalable model for symmetrical inductors within a certain dimension range is available. More specifically, within an outer dimension of 75-to-300 um, a coil width of 7.02-to-15 um and a line spacing of 3-to-5 um, we have a symmetrical inductor fully modeled without EM simulations. Our goal is to figure out the parameter combination yielding the highest Q factor and a self-resonance frequency reasonably above the operating frequency of 4.5 GHz.

Since the trade-offs are multidimensional, an enumeration of all parameter combinations with a cost function of Q factors is a straightforward solution. However, this brute-force searching process is computationally intensive. In order to shrink the design space, several heuristics are considered.

First of all, an M1 metal ground plane is used to prevent capacitive coupling to the substrate. This measure reduces the induced current flowing in the ohmic substrate, which increases the Q factor. Furthermore, noise coupling between the inductor and the substrate is also shielded. The penalty of this measure is the reduced self-resonant frequency caused by the increased capacitance.

Secondly, the minimum line spacing of 3 um is used to maximize the magnetic coupling among adjacent lines. This measure increases the inductance and the Q factor. However, the self-resonant frequency is also influenced because of the increased capacitance between adjacent conductors.

Intensive simulations are performed to enumerate the value of outer dimension, conductor width and the number of turns. As a result, the inductor with the highest Q factor and a reasonably high self-resonant frequency is selected with its parameters shown in Tab. 5.2

Parameter	Value
Outer dimension	300 x 300 um
Line width	15 um
Line spacing	3 um
Number of turns	2
Q factor	23
Self-resonance frequency	6.65 GHz

Table 5.2: Inductor parameters.

5.2.7 Power Supply, Oscillation Amplitude and Oxide Integrity

For the SRO shown in Fig. 5.1, the DC value of the oscillation is the supply voltage. The maximal voltage swing can reach up to twice as large as this value. While these properties are desirable for low-power high-performance oscillators, high-voltage operation threatens the integrity of gate oxide. As the device dimensions shrink down, oxide thickness also decreases. Thin oxide is vulnerable to stressing voltages. The thickness of gate oxide for IBM 90-nm CMOS is 1.4 nm, which has a breakdown voltage of 1.32 V. Even below this value, gradual oxide degradation still happens under a long-duration of voltage stress.

5.2.7.1 Power Supply Consideration

Minimal supply voltage is desired for low-power operation and maximal oscillation voltage swing. For a nominal voltage supply of 1 V, a $\pm 20\%$ variation of this voltage is normally acceptable. So the positive voltage swing of this SRO is limited to be 1.2 V. The verification of dielectric integrity to be discussed in a later paragraph shows that this maximum of 1.2 V is not going to cause oxide breakdown or degradation. Further increasing the voltage swing and reducing the power consumption requires the decreasing of supply voltage.

However, the minimum supply voltage is limited by LNA which is likely to use a cascode structure for reverse isolation. Moreover, the input transistor is likely to be biased in strong inversion for a decent transit frequency, which needs a gate-source voltage of around 600 mV. Taking these factors into consideration, we decide a supply voltage of 900 mV.

5.2.7.2 Oscillation Amplitude

We pursue the maximum oscillation amplitude despite its adverse influence on power consumption, because the lack of receiver back-end specification requests the universality and adaptability of this receiver front-end. In other words, this frond-end

should not impose severe noise requirement to its following stages. This objective demands a large output amplitude.

Given the supply voltage of 900 mV and a maximum voltage limit of 1.2 V, the voltage swing amplitude should not exceed 300 mV, i.e. a single-ended peak-to-peak swing of 600 mV and a differential peak-to-peak swing of 1200 mV.

5.2.7.3 Dielectric Integrity Verification

The absolute maximum oxide breakdown voltage can be estimated according to IBM's technology design manual [33]. For a product lifetime of 100 KPOH (thousand of power-on hours), a maximum temperature of 85 °C, an area of gate oxide of $2 \times 200\text{um} \times 100\text{nm}$ and a power-supply voltage of 900 mV, we have a maximum permitted transient voltage of 1.6 V. So a 300 mV voltage swing amplitude (i.e. 1200 mV differential peak-to-peak oscillation) is not going to cause oxide breakdown or degradation.

5.2.8 Simulation Result

A transient simulation is performed to the super-regenerative oscillator. The simulation result is shown in Fig. 5.8.

The stimulus to the SRO is a 4.5 GHz RF carrier being modulated by a 1 MHz triangular wave, with a modulation bandwidth of 500 MHz, as specified in the UWB-FM specification. A period of the modulation signal is shown at the top of Fig. 5.8, from 0 to 1000 ns. At t=0 and 1000 ns, the subcarrier has the minimum value, yielding an RF signal with an instantaneous frequency of 4.25 GHz. At t=500 ns, the subcarrier is at its maximum, generating the RF signal with 4.75 GHz instantaneous frequency. At t=250 and 750 ns, the subcarrier is 0, so the RF frequency at those time is 4.5 GHz.

The single-ended voltage output of the SRO is shown in the middle of Fig. 5.8. The frequency response of the SRO can be observed. When the input signal has a frequency of 4.5 GHz, the SRO outputs the maximum oscillation amplitude of around 0.3 V. The deviation of frequency from its center yields the reduction of output amplitude. When the RF frequency is at 4.25 or 4.75 GHz, the output amplitude is the minimum.

The biasing current waveform is shown in the bottom of Fig. 5.8. In every biasing period of 35 ns, the current ramps from 0 to 1.2 mA in 15 ns. Then it drops to 0 at once and keeps a 0 value for the rest 20 ns. This SRO draws 0.257 mA in average from a 0.9 V supply, yielding a power consumption of 231 uW.

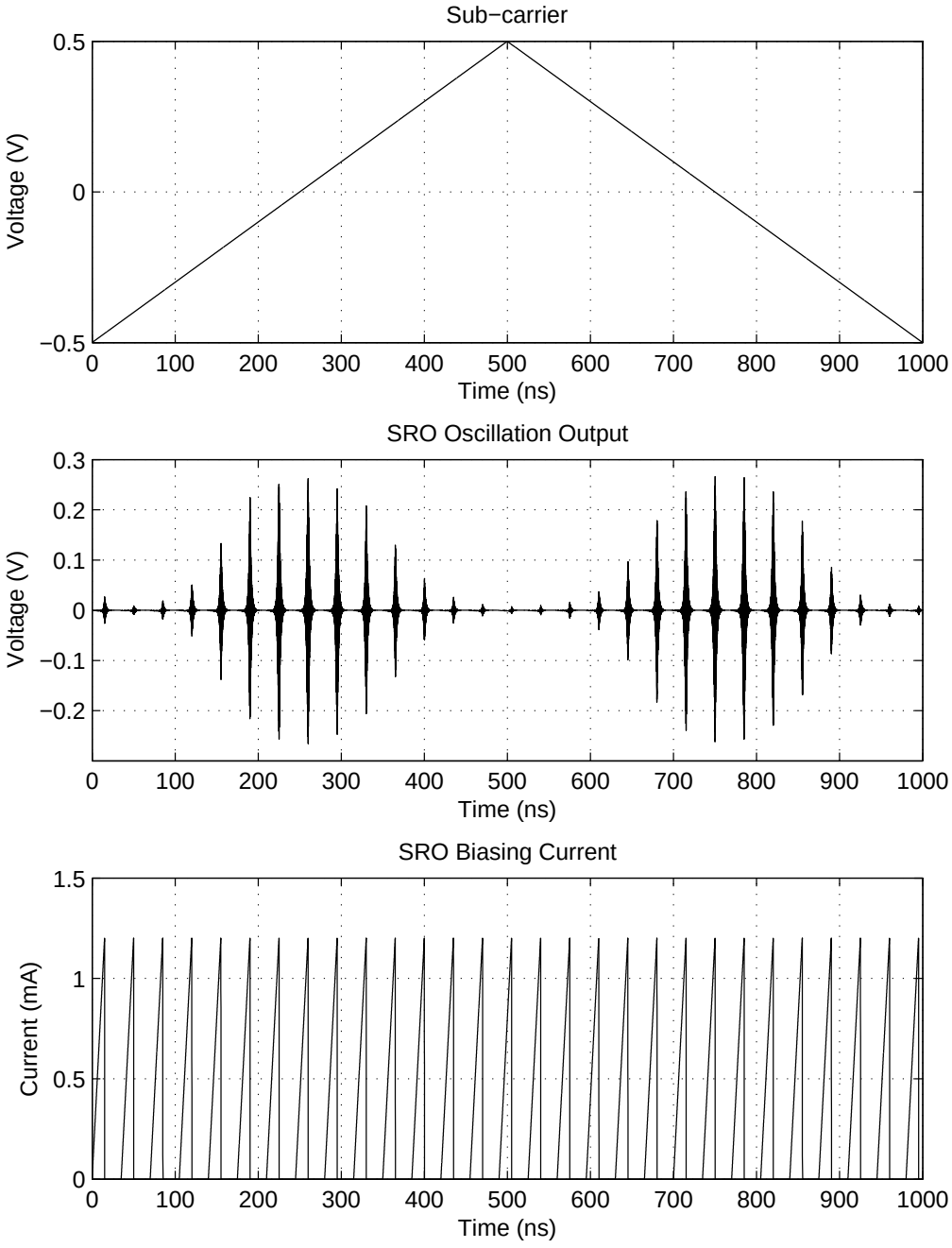

Figure 5.8: The baseband signal, output oscillations and the SRO biasing current.

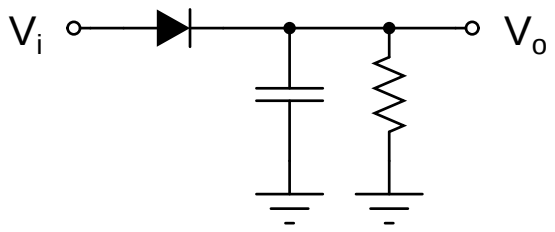

Figure 5.9: The simplest peak detector.

5.3 Peak Detector

5.3.1 Design Objective

Peak detectors extract slow-varying oscillation envelope by following the oscillation's peaks. They are frequently used as simple amplitude demodulators. In this project, a peak detector is designed to demodulate an AM signal, which is converted from UWB-FM by the super-regenerative oscillator.

The design goal for this peak detector is the maximum conversion gain and low power dissipation. The conversion-gain definition of peak detectors are identical with that of mixers, which is the output envelope magnitude divided by the input oscillation amplitude.

5.3.2 The Differential Peak Detector

The simplest peak detector is shown in Fig. 5.9, which consists of a diode, a capacitor and a resistor. Assuming an ideal diode for simplicity and an RC time constant much larger than the incoming signal, we can describe its operation as follows. When a peak comes and $V_i > V_o$, the diode conducts; V_o follows V_i and the capacitor is charged. After the peak, $V_i < V_o$, the diode is tuned off; the capacitor hold the peak voltage and the resistor slowly discharges the capacitor. The discharge speed is set in such a way that when the next peak comes, V_o is always *slightly* smaller than V_i to close the diode, charge the capacitor and track the pulse while maintain the smoothness of the output envelope.

The circuit used in our design is shown in Fig. 5.10. Two diode-connected MOSFETs, M1 and M2, substitute the diode in Fig. 5.9 to track both positive and negative peaks of a differential oscillation. A tail current source M3 discharges the capacitor instead of the resistor. A dummy duplicate of this circuit, M1'–M3' copies the same voltage drop to output a reference voltage, so that V_o will be zero when oscillation envelope is zero.

The differential structure is used for 2 reasons. First of all, it tracks the differential output peaks of both polarities. So the discharge speed could be twice as much

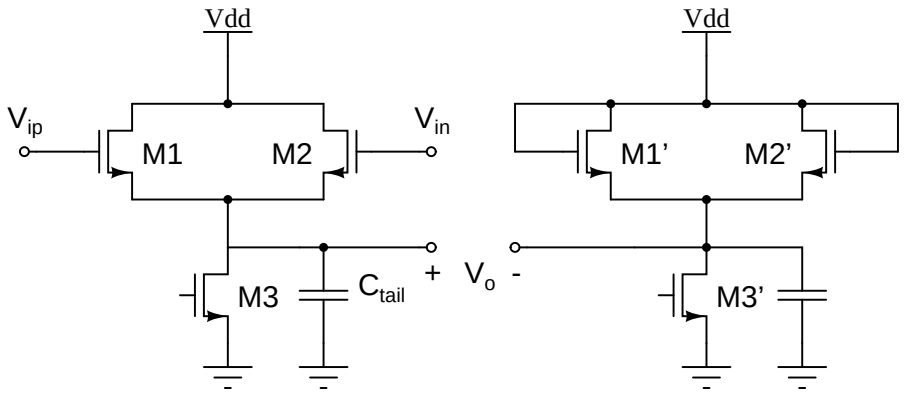

Figure 5.10: The differential NMOS peak detector.

as before without influencing envelope smoothness. A faster discharge is desirable in this receiver because the oscillation envelope is exponentially shaped pulses, which are sharp and require fast tracking. The second reason to use a differential structure is that it behaves as a balanced load to the symmetrical oscillator. Maintaining symmetry is good for common-mode noise rejection.

The design parameters to be determined are the biasing current, the capacitor value and the physical dimension of M1 and M2.

5.3.3 Biasing and Conversion Gain

In this subsection, we explain that the 2 source followers, M1 and M2 should be biased in deep weak-inversion to maximize the peak detector's conversion gain.

Traditionally, diodes and bipolar transistors are used as the nonlinear switches. Both types of them have an exponential V-I relationship. The transfer characteristic of peak detectors built from these devices can be approximated as

$$V_o = V_i - V_T \ln \sqrt{\frac{2\pi V_i}{V_T}}, \tag{5.12}$$

where V_i, V_o and V_T are the input and output amplitude and thermal voltage, respectively [34].

When MOSFETs are working in weak-inversion, the V-I relationship is still exponential, expressed as

$$I_d = I_{d0} \exp\left(\frac{V_{gs}}{nV_T}\right) \tag{5.13}$$

where $n > 1$ is called the nonideal or slope factor, and V_T is the thermal voltage. The transfer characteristic of peak detectors using weakly inverted MOSFETs is

adapted from Equ. 5.12 as

$$V_o = V_i - nV_T \ln \sqrt{\frac{2\pi V_i}{nV_T}}. \tag{5.14}$$

For MOSFETs working in strong inversion, the square-law applies

$$I_d = \frac{1}{2}\mu_n C_{ox} \frac{W}{L} \left(V_{gs} - V_{th}\right)^2. \tag{5.15}$$

A sinusoidal excitation $2V_i \cos(\omega t)$ applied to the input of MOSFET M1 or M2 yields a drain current

$$\begin{aligned} I_d &= \frac{1}{2}\mu_n C_{ox} \frac{W}{L} \left(\tilde{V}_{gs} + V_i \cos(\omega t) - V_{th}\right)^2 & (5.16)\\ &= \frac{1}{2}\mu_n C_{ox} \frac{W}{L} \left[\left(\tilde{V}_{gs} - V_{th}\right)^2 + 2\left(\tilde{V}_{gs} - V_{th}\right) V_i \cos(\omega t) + V_i^2 \cos^2(\omega t)\right] & (5.17) \end{aligned}$$

where

$$\tilde{V}_{gs} = V_G - V_s, \tag{5.18}$$

V_G and V_s are the DC gate voltage and transient source voltage. Since M1 and M2 are alternatively switched on and off for 50% of the time by nearly identical peak amplitudes, they share the bias current evenly. And the average tail current of M1 and M2 is limited by half of the biasing current, i.e.

$$\begin{aligned} \frac{I_{tail}}{2} &= \overline{I_d} = \int_{-\frac{T}{2}}^{\frac{T}{2}} \frac{1}{2}\mu_n C_{ox} \frac{W}{L} \left[\tilde{V}_{ov}^2 + 2\tilde{V}_{ov} V_i \cos(\omega t) + V_i^2 \cos^2(\omega t)\right] \mathrm{d}t & (5.19)\\ &= \overline{I_d} = \frac{1}{2}\mu_n C_{ox} \frac{W}{L} \left(\tilde{V}_{ov}^2 + \frac{V_i^2}{2}\right), & (5.20) \end{aligned}$$

where I_{tail} and $\overline{I_d}$ are the tail biasing and average drain current, and

$$\tilde{V}_{ov} = \tilde{V}_{gs} - V_{th} = V_G - V_s - V_{th} \tag{5.21}$$

is the transient overdrive voltage. For M1' and M2', the tail current is also evenly shared and the same square-law applies

$$\frac{I_{tail}}{2} = I_d' = \frac{1}{2}\mu_n C_{ox} \frac{W}{L} \left(V_{gs}' - V_{th}\right)^2. \tag{5.22}$$

Equating Equ. 5.20 and 5.22, we have

$$\tilde{V}_{ov} = \sqrt{\left(V_{ov}'\right)^2 - \frac{V_i^2}{2}}, \tag{5.23}$$

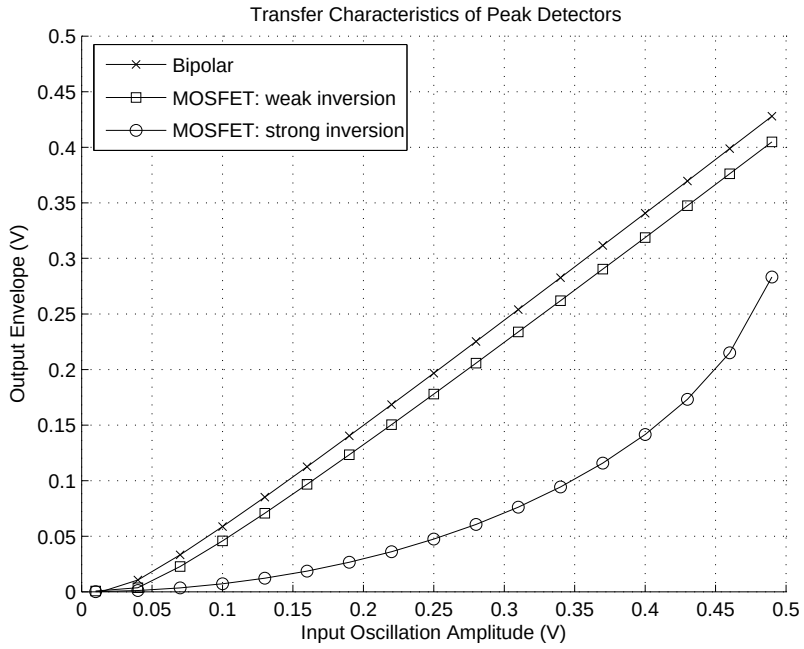

Figure 5.11: Transfer characteristics of peak detectors.

where

$$V'_{ov} = V'_{GS} - V_{th} = V_G - V'_S - V_{th} \tag{5.24}$$

is the overdrive voltage of MOSFET M1' and M2'. The output voltage of the peak detector is defined as

$$\begin{aligned} V_o &= V_s - V'_S & (5.25)\\ &= V'_{ov} - \tilde{V}_{ov}. & (5.26) \end{aligned}$$

Substituting Equ. 5.23 into 5.26 yields

$$V_o = V'_{ov} - \sqrt{(V'_{ov})^2 - \frac{V_i^2}{2}}. \tag{5.27}$$

Equ. 5.27 is the transfer characteristic of a peak detector using square-law nonlinear devices.

A comparison of conversion gains of peak detectors using MOSFETs working in weak- and strong-inversion, is now possible by using Equ. 5.14 and 5.27. Fig. 5.11 plots the transfer characteristics of peak detectors utilizing bipolar transistors, MOSFETs working in weak-inversion with a slope factor of 1.5 and those working in strong inversion with an overdrive voltage of 0.5 V. As shown in the graph, bipolar peak detectors have the highest conversion gain of 0.873. Weakly inverted MOSFETs cause a slightly inferior conversion gain of 0.826. Strongly inverted MOSFETs yields the worst result, a conversion gain of 0.578, which is significantly lower than the other

two.

It is worth mentioning here that peak detectors fabricated by standard CMOS technologies can also perform as the bipolar ones by using dynamic threshold MOSFETs (DTMOSs). In essence, DTMOSs are PMOSs or triple-well NMOSs with connections from their bodies to their gates, which form parasitic bipolar transistors. However, DTMOSs are not used in this design since the use of PMOSs needs AC coupling and triple-well NMOSs require 3 additional masks. In other words, the extra gain squeezed out by DTMOSs is too little to justify the trade-offs.

5.3.4 Parameter selection

The design parameters to be determined are the biasing current I_{tail}, the source capacitor value C_{tail} and the width of M1 and M2. The previous subsection concludes that MOSFETs should be biased in deep subinversion to have the maximum conversion gain. This implies a large transistor width and a small tail current.

The largest transistor width is limited by the parasitic capacitances between the two gates. Since the peak detector is in shunt with the resonation tank, all these capacitances contribute to the tank. The frequency stability can be severely influenced if these parasitics dominate the tank capacitance. Considering the inductor we selected, a 655 fF total capacitance is required for the tank to resonate in 4.5 GHz. We limit the parasitics to 10% of this total value, i.e. 65 fF, so that a 20% variation of parasitics causes less than 1% of frequency deviation.

The tail current and source capacitor together determine the discharge time constant. This time constant is an intrinsic trade-off between amplitude accuracy and output dynamic range. A slow discharge accurately follows the peak, but only a small envelope variation can be followed. On the other hand, a fast discharge can follow fast envelope variation, but it detects not only the peaks, but also the rising curve before peaks. In our design, the maximum voltage drop between 2 peaks is around 30 mV, in a period of 0.22 ns. This determines the current-capacitance ratio to be

$$\frac{I_{tail}}{C_{tail}} = \frac{V_{drop}}{T_{period}} = \frac{30\text{ mV}}{0.22\text{ ns}} = \frac{30\text{ uA}}{0.22\text{ pF}}. \tag{5.28}$$

The source capacitor should be much larger than, or should take into account, the input capacitance of the following stage. Otherwise the discharge time constant would be different. In our design, a voltage buffer for measurement purpose is the load of the peak detector. We choose a C_{tail} of 100 fF, then the biasing current is calculated by Equ. 5.28 to be 15 uA.

It is worth mentioning here that the $^{kT}/_{C}$ noise should not be considered when choosing the value of C_{tail} . Sooner or later, after the envelope detection, a bandpass filter has to be applied to extract the subband signal. The bandwidth of this

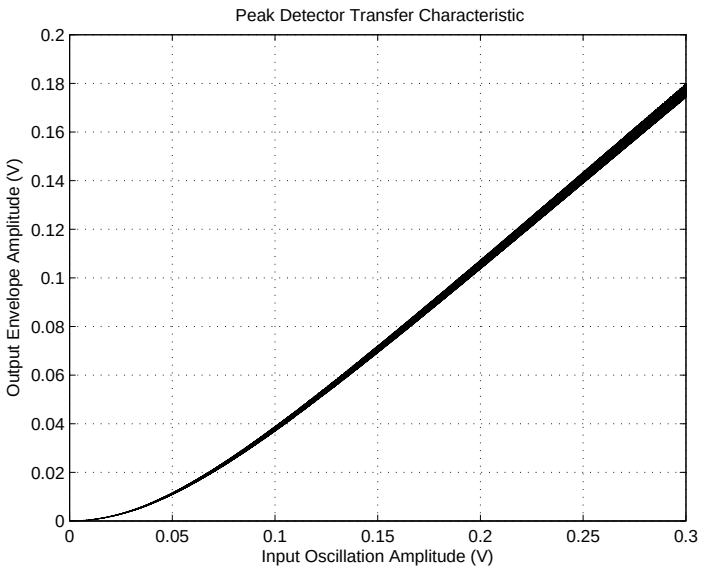

Figure 5.12: The simulated transfer characteristic.

bandpass filter is smaller than the bandwidth determined by C_{tail}. So a large source capacitor cannot improve the noise performance in this receiver front-end.

5.3.5 Simulation Results

5.3.5.1 Transfer Characteristic

The transfer characteristic showing the voltage amplitude of the input and the output is plotted in Fig. 5.12. From the graph, it can be observed that a 0-to-300 mV oscillation amplitude yields a 0-to-180 mV output envelope, which indicates a conversion gain of around 0.6. Furthermore, the nonlinearity of conversion gain can be observed from Fig. 5.12 (and also Fig. 5.11) when the input oscillation amplitude is small. This reduced conversion gain sets the minimum detectable oscillation amplitude (about 40 mV), which can be beneficial since the small oscillations caused by noise are suppressed.

The peak detector's response to the practical signal generated by an SRO is plotted in Fig. 5.13. As shown in the graph, the envelope is extracted from the oscillation, with a certain amount of attenuation.

The peak detector draws 30 uA from the 0.9 V supply, yielding a power consumption of 27 uW.

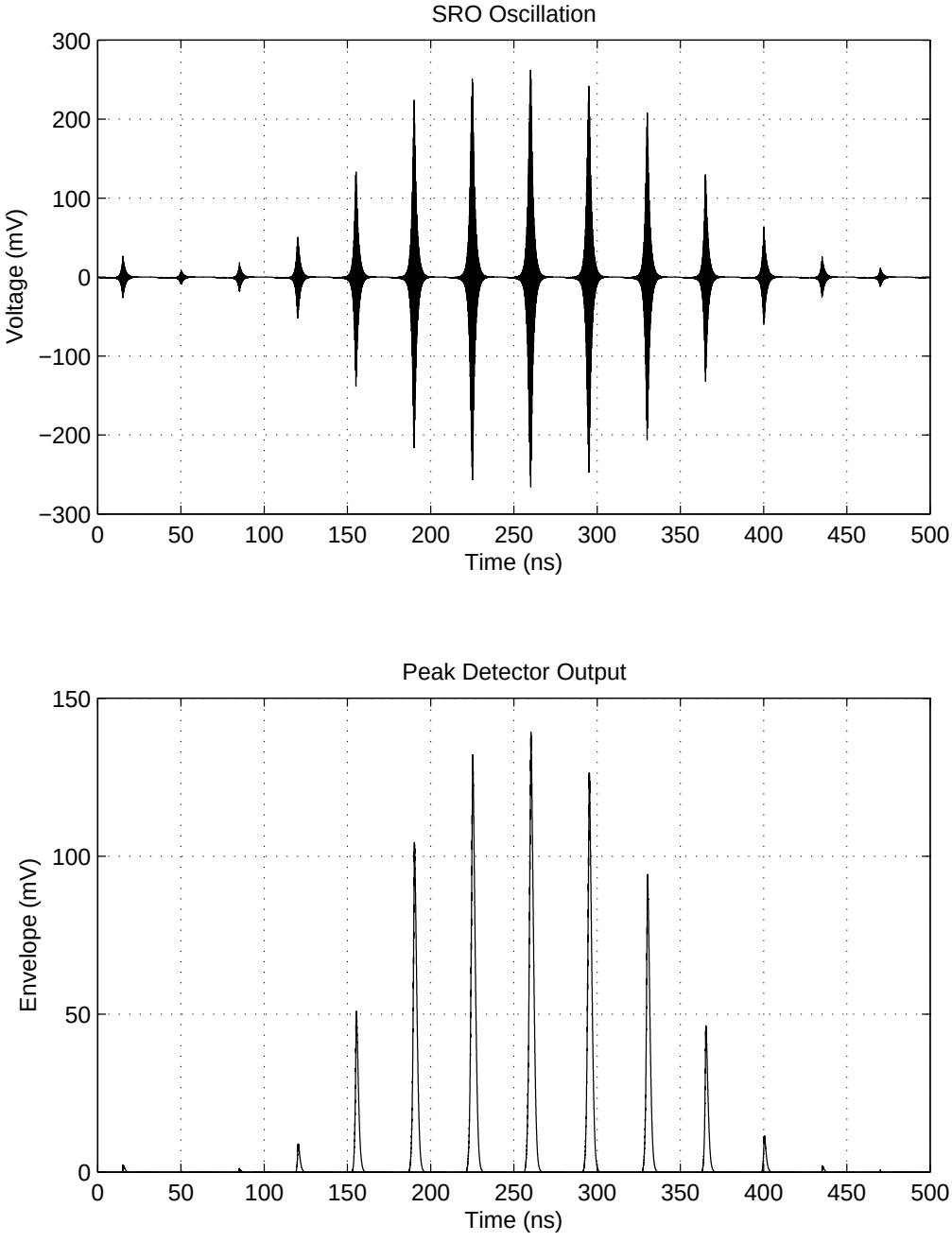

Figure 5.13: The oscillation and its envelope.

GM (mS)	SNRo (dB)	NF Budget (dB)
100	20	9
20	14	3
10	11.3	0.3
1	4.2	-6.8

Table 5.3: Output SNR vs. LNA transconductance and noise figure budget.

5.4 Low-noise Amplifier

5.4.1 Design Objective

The LNA performs several functions in this receiver front-end. First of all, it preamplifies the received weak RF signal to a certain level such that noise in following stages is comparatively insignificant. Secondly, it behaves as an impedance matching network between the antenna and the following SRO. Thirdly, it shields the high-power oscillation of SRO from coupling back into the antenna. As a result, the LNA has to satisfy several requirements in order for the system to operate properly.

5.4.1.1 Input Impedance

The characteristic impedance of the antenna is 50 ohm given as a specification. For a differential input, an off-chip balun of 1:2 (50:100) impedance transformation ratio is assumed. A hybrid ring would be a practical example.

5.4.1.2 Gain and Noise Figure

The requirements of the gain and noise figure for the LNA are derived from a test-bench simulation with the already designed SRO, peak detector and an ideal transconductance block. In essence, we plug in the worst-case RF excitation and find out the transconductance that yields the minimum acceptable output SNR. More specifically, from Section 4.2, the worst-case RF signal is -80 dBm (Equ. 4.4) when the receiver is 10 meters away from the transmitter. And the required output SNR is 11 dB (Equ. 4.12) for a data-rate of 100 kbps and a bit-error-rate of 10^{-6}.

For super-regenerative receivers, we argue the necessity of using the transconductance instead of voltage or power gain to characterize an LNA. When an SRO is following an LNA, it modifies the load resistance of the LNA constantly. The negative conductance behaves as a gain-boosting amplifier when it is in shunt with the load impedance of an LNA (since it increases the load resistance). The voltage and power gain is also changing, so they are time-varying. On the other hand, transconductances can be load-resistance independent.

Intensive simulations, to be discussed in Section 7.2, yield the relationship be-

tween LNA transconductance and output SNR listed in Tab. 5.3. As shown in the table, there is a trade-off between the gain and noise figure requirements. A high gain suppresses the noise of following stages so the LNA NF dominates the receiver NF. On the other hand, a low gain brings the noise of following stages into play and the NF requirement is tightened. A sensible choice for LNA specification from Tab. 5.3 is a transconductance of 20 mS and a noise figure of 3 dB.

In the LNA design process, it is convenient to use a constant resistance, the passive tank resistance of 1046 ohm, as the load. Then, the voltage gain of the LNA is calculated as

$$A_v = GM * R_L = 20.9, \tag{5.29}$$

and the power gain is

$$S_{21} = \frac{\frac{V_o^2}{R_L}}{\frac{V_i^2}{R_S}} = A_v^2 \frac{R_S}{R_L} = 41.8 = 16.2\,\text{dB}. \tag{5.30}$$

5.4.1.3 Reverse Isolation

As discussed in Section 4.2, ETSI (European Telecommunications Standards Institute) imposes a narrow-band spurious emission limitation of less than -47 dBm EIRP (Effective Isotropic Radiated Power) [32]. In our design the SRO produces high-power oscillation at 4.5 GHz, which needs to be attenuated to satisfy the spurious emission specification.

A maximum oscillation amplitude of 0.3 V generated by the SRO has a power of

$$P_{osc} = \frac{V_{rms}^2}{R_L} = \frac{2 \times 0.3^2}{1046} = 0.17\,\text{mW} = -7.6\,\text{dBm}, \tag{5.31}$$

when applied on the 1046 ohm load resistance. The required LNA isolation can then be calculated as

$$S_{12} = -47\,\text{dBm} - P_{osc} = -39.4\,\text{dB}. \tag{5.32}$$

5.4.1.4 Specification Summary

The LNA specifications are summarized in Tab. 5.4. Besides these requirements that must be satisfied, minimum power consumption is the goal to pursue.

5.4.2 The Schematic

The LNA schematic is shown in Fig. 5.14. Essentially, it is a differential degenerated common-source stage with cascode and neutralization. More specifically, MOSFETs M1 and M2 are the common-source input stage with their sources degenerated by Ls, to provide a real part of the input impedance. MOSFETs M3 and M4 are the

Parameter	Value
Input Impedance	100 ohm (differential)
GM	$>$ 20 mS
S_{21}	$>$ 16.2 dB
NF	$<$ 3 dB
S_{12}	$<$ -39.4 dB
Bandwidth	500 MHz

Table 5.4: LNA specification summary.

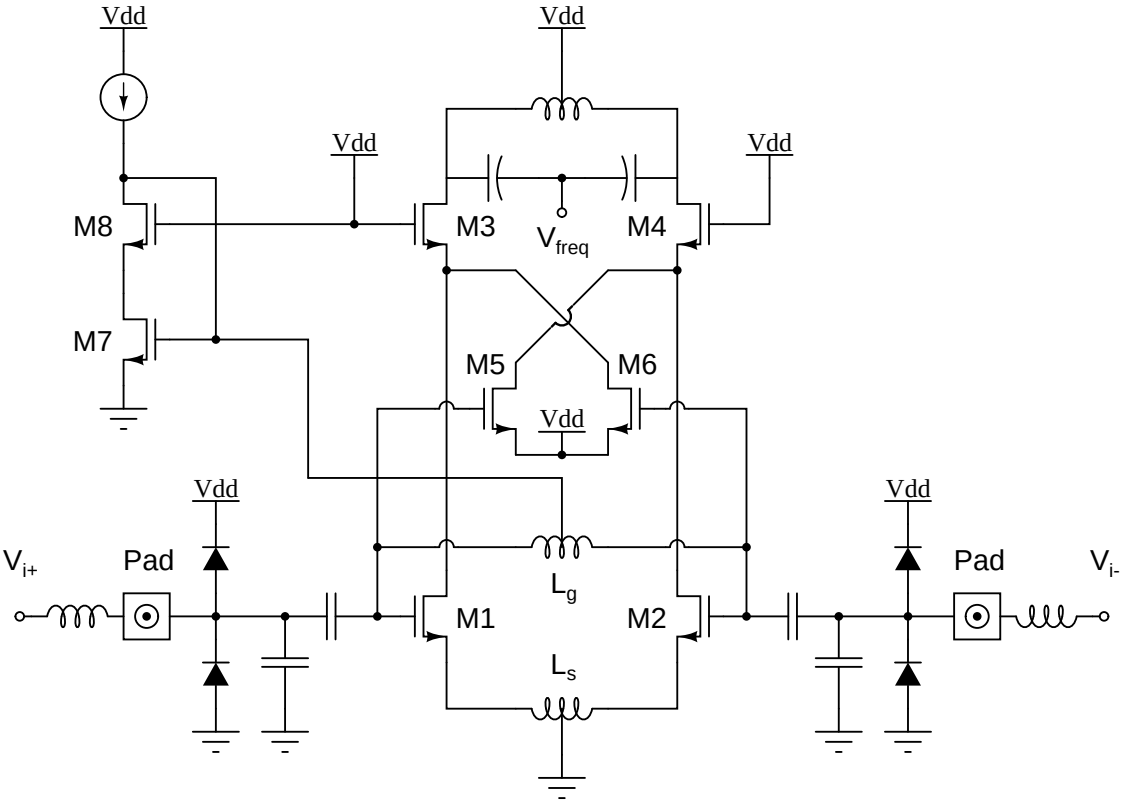

Figure 5.14: The schematic of the LNA.

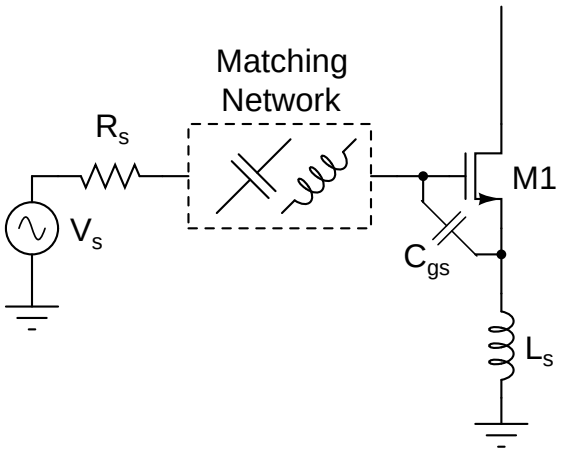

Figure 5.15: Simplified LNA input.

cascode which provide reverse isolation and increase the output impedance to avoid loading the oscillator tank. Extra reverse isolation is provided by the neutralization MOSFETs M5 and M6. The matching network at each side is formed by the degeneration inductor L_s, biasing inductor L_g, a shunt and a series capacitor, the ESD diodes, a C4 pad and a bond-wire. MOSFETs M7 provides the biasing voltage to the gates of M1 and M2 through L_g.

We adopt the differential structure because of its common-mode noise rejection and even-order harmonics suppression. Common-source input stage is chosen for its high power gain compared with common-gate or common-drain stages. Inductive degeneration is capable of noise matching and GM boosting[1] besides its impedance matching functionality. We use the cascode stage not only to provide reverse isolation, but also to prevent the output impedance from loading the oscillation tank. Neutralization is applied for the insufficient isolation of the cascode stage.

Despite the popularity of this topology, we perform a power-driven design procedure which is quite different from the classical methodology [25], which is, from our point of view, noise-driven.

5.4.3 Power-driven Design Procedure

The design procedure discussed in this subsection derives the minimum power for a certain gain and bandwidth, given the device characteristics of a certain fabrication process.

5.4.3.1 Minimum Ft

We derive the relationship between the LNA transconductance and the transition frequency of the input stage.

The input part of the LNA is redrawn in Fig. 5.15. We neglect the cascode and neutralization MOSFETs since they do not contribute or influence the LNA transconductance. The gate to source capacitance, C_{gs}, is drawn explicitly. If the impedance is matched, the current flowing into the dashed box is

$$i_s = \frac{v_s}{2R_s}. \tag{5.33}$$

Furthermore, if the matching network is lossless, maximum power transfer is achieved and all the current is flowing into the degenerated resistor. Then the voltage across C_{gs} is expressed as

$$v_{gs} = \frac{i_s}{j\omega C_{gs}} = \frac{v_s}{j\omega C_{gs} 2R_s} = -jQv_s \tag{5.34}$$

where Q is the quality factor of the input network

$$Q = \frac{1}{2\omega C_{gs} R_s}. \tag{5.35}$$

Then the single-ended transconductance of LNA is expressed as

$$GM_{single} = 2 \cdot GM = \frac{i_d}{v_{gs}} \frac{v_{gs}}{v_s} = -jQ \cdot g_m = \frac{g_m}{j2\omega C_{gs} R_s} = \frac{\omega_T}{2j\omega R_s}, \tag{5.36}$$

where g_m and ω_T is the small-signal transconductance and angular transit frequency of the input MOSFET. From Equ. 5.36, we observe that for an operating frequency of 4.5 GHz, a source impedance of 50 ohm, and $GM > 20\,\text{mS}$ the transit frequency is

$$f_t = \frac{2 \cdot GM \cdot 2j\omega R_s}{2\pi} > 18\,\text{GHz} \tag{5.37}$$

5.4.3.2 Minimum Current Density

The DC operating points of an IBM 90-nm RF NMOS is extracted from a gate voltage sweep. The plots of transit frequency and current density vs. gm/Id are given in Fig. 5.16 and 5.17. We use the parameter gm/Id to indicate the degree of inversion. From Fig. 5.16, we observe that a gm/Id of no less than 14 is required to achieve the transit frequency of 18 GHz. In Fig. 5.17, we pick a current density of 20 uA/um, which yields a gm/Id of about 12.

[1]The gate to source voltages, V_{gs}, of M1 and M2 are increased to Q times the input voltage, V_{i+} or V_{i-}. So the equivalent transconductance of the LNA is also Q times larger than the transconductance of the differential pair, as will be shown in Equ. 5.36.

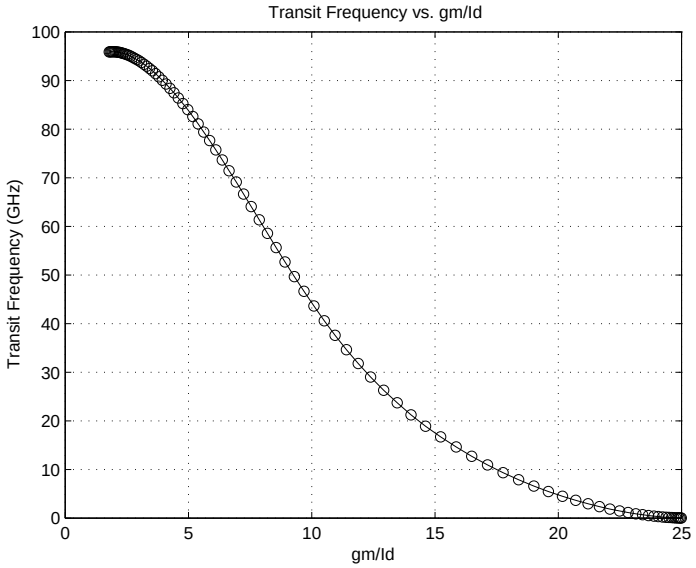

Figure 5.16: Transit Frequency vs. gm/Id.

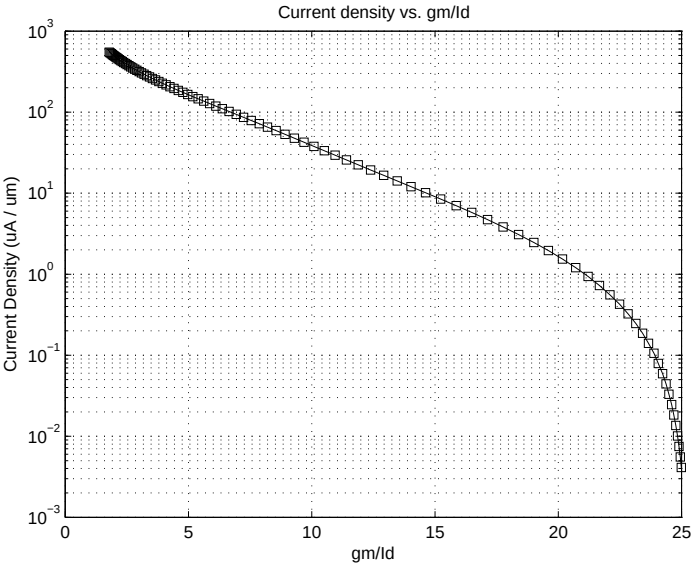

Figure 5.17: Current density vs. gm/Id.

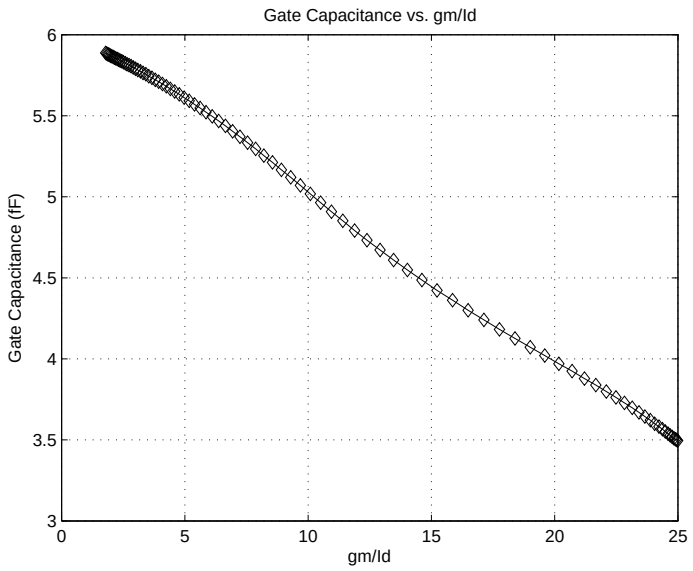

Figure 5.18: Gate capacitance vs. gm/Id.

Until now, the power dissipation is still unclear but the drain current to MOSFET width ratio is determined.

5.4.3.3 Minimum Power

According to our bandwidth requirement of 500 MHz and the center frequency of 4.5 GHz, the quality factor of the matching network is

$$Q = \frac{f_0}{BW} = 9. \tag{5.38}$$

Substituting this Q into Equ. 5.35, we can derive the C_{gs} requirement of

$$C_{gs} = \frac{1}{2\omega Q R_s} = 39\,\text{fF}. \tag{5.39}$$

The gate capacitance as a function of gm/Id is shown in Fig. 5.18 for a transistor of 3.6 um. When gm/Id=12, we have a gate capacitance of around 5 fF. We need to scale it 8 times larger to satisfy the C_{gs} requirement, which yields a MOSFET width of 30 um.

Finally, the minimum biasing current is calculated as

$$I_{min} = 20\,\text{uA/um} \times 30\,\text{um} = 600\,\text{uA}. \tag{5.40}$$

And the differential structure consumes, therefore, 1.2 mA.

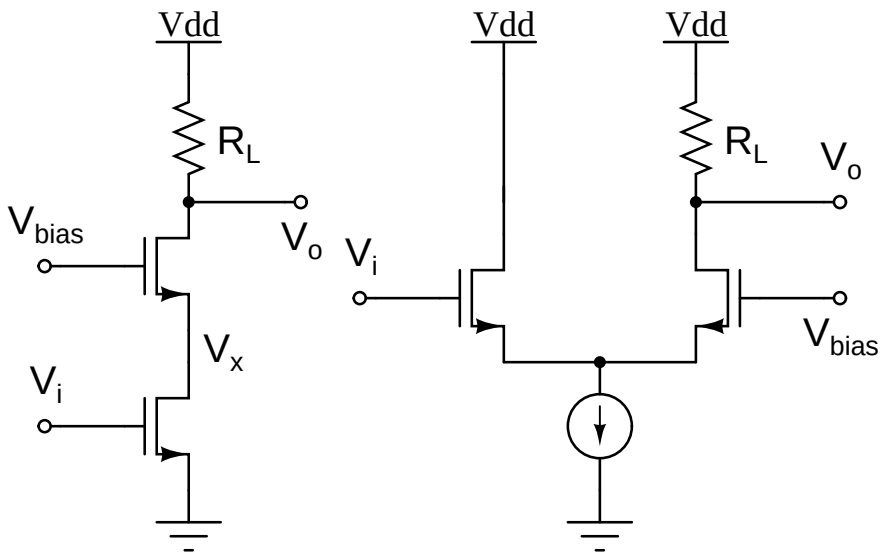

(a) CS-CG (b) CD-CG

Figure 5.19: Unilateralization techniques.

5.4.4 Reverse Isolation

The signal at the output of an amplifier can be coupled back to the amplifier's input by parasitics. For super-regenerative receivers, the amplifiers output has large voltage swing caused by periodic oscillations. This characteristic of an SRO imposes stringent requirement of reverse isolation to the LNA in front of it.

The reverse coupling is mainly caused by the drain to gate capacitance, C_{gd}, of a common-source stage. Commonly used techniques to mitigate the reverse coupling of C_{gd} are the unilateralization and neutralization [35]. In this LNA design, the reverse isolation specification of -39.4 dB is achieved by applying both techniques. Simulations show that a 10% mismatch of the neutralization MOSFETs still leads to acceptable results.

5.4.4.1 Unilateralization

Unilateralization techniques plug in devices in series with the signal path to attenuate signals in one direction. The two commonly used unilateralization method are the CS-CG and the CD-CG combinations, as shown in Fig. 5.19. Both schemes are actually 2-stage designs exploiting the shielding effect of the CG stage. The penalties paid are the increased voltage or current consumption.

In this design, we apply the CS-CG topology, or a cascode. The motivation is that the output resistance of a cascode stage is higher than that of a CD-CG stage. This prevents the output resistance of the LNA from loading the oscillation tank of the following stage.

The shielding effect of a cascode stage can be demonstrated by its reverse transfer

function

$$\frac{v_x}{v_o} = \frac{1}{g_m r_o + \frac{r_o}{R_{o1}} + sC_{gs}r_o + 1}, \tag{5.41}$$

where g_m, r_o and C_{gs} are the transconductance, drain-to-source resistance and gate-to-source capacitance, and R_{o1} are the output resistance of the CS stage. In this expression, C_{gd} of the cascode is neglected for simplicity. In a reasonable design, the second and the third term of the denominator in Equ. 5.41 cannot be much larger than 1.[2] So the main attenuation is given by the intrinsic gain of the cascode stage.

Since 90-nm short-channel devices have their intrinsic gain no more than 10, we increase the length of the cascode MOSFETs to 200 nm. Further increase of length has a diminished return of intrinsic gain but a more serious f_t trade-off. Smaller f_t of the cascode transistors yields a smaller g_m that is incapable of suppressing Miller effect, and a large C_{gs} that lowers the 2nd pole. The 200 nm transistors provide an intrinsic gain of 20, which implies a reverse isolation of -26 dB. Accounting for the -8 dB attenuation caused by C_{gd} coupling, we still need -6 dB isolation.

The preceding analysis shows that barely cascoding cannot provide sufficient reverse isolation for our receiver.

5.4.4.2 Neutralization

Neutralization techniques plug in devices in parallel with the signal path to produce a 180-degree phase shift. Because the LNA has a differential structure, it is convenient to cross couple the output back using the equal amount of coupling capacitance. As shown in Fig. 5.14, transistor M5 and M6 are identical with M1 and M2. The signal coupled by C_{gd} of M5 has the same amplitude as that coupled by C_{gd} of M1, but is 180-degree out of phase. So the two signals cancel each other. The same effect is produced between M2 and M6.

The effect of cancellation highly depends on the matching of C_{gd}, which is not only process- but also voltage-dependent. When devices are perfectly matched, the simulation result shows an extra -18 dB attenuation is obtained, which yields a total reverse isolation of -52 dB. A 10% mismatch analysis shows that all the LNA specifications are still satisfied.

5.4.5 Input Impedance Matching

Compared with the classical inductive degenerated impedance matching, several unique problems are tackled in this design. Firstly, the super-regenerative oscillator

[2]The Miller effect is mitigated by letting $1/g_m \ll R_{o1}$, i.e. $g_m R_{o1} \gg 1$ which implies that R_{o1} and r_o are in the same order of magnitude. Furthermore, the 2nd pole at the node v_x should not be dominant, i.e. $g_m/C_{gs} = g_m r_o/C_{gs} r_o \gg BW$, so signals within the bandwidth yield $sC_{gs}r_o$ not much larger than 1.

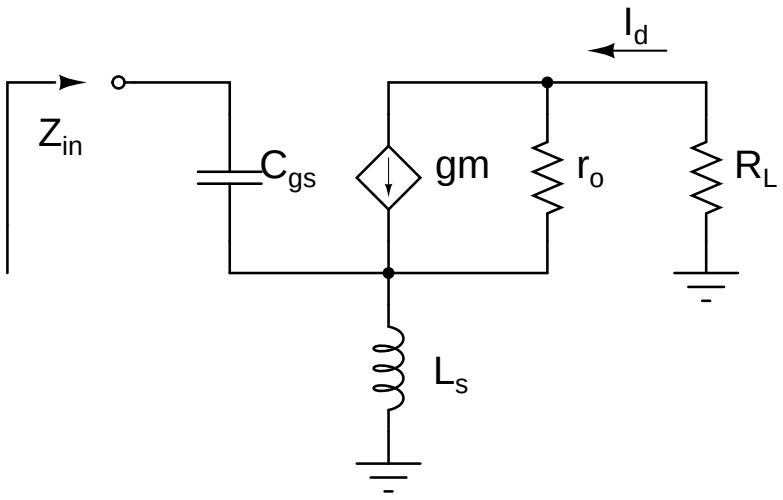

Figure 5.20: Simplified model of inductive degenerated common-source.

following the LNA is a time-varying load. The large load variation leads to input mismatch for bilateral amplifiers. Secondly, special issues arise when neutralization capacitors are used together with inductive degeneration. Last but not least, low-power input stage causes trouble when low-Q matching is desired.

5.4.5.1 Load Dependency of Input Impedance

The simplified model to calculate the input impedance of inductive degenerated common-source stage is shown in Fig. 5.20. A commonly used formula to express the input impedance is derived by the β gyration as

$$Z_{in} = \frac{1}{j\omega C_{gs}} + j\omega L_s\left(1+\beta\right) = \frac{1}{j\omega C_{gs}} + j\omega L_s + \omega_T L_s \tag{5.42}$$

where $\beta = {}^{\omega_T}/_{j\omega}$ is the forward current gain. This expression, however, implicitly assumes $R_L \ll r_o$. For most of LNAs, this condition is true or can be made true by cascoding. In a super-regenerative receiver, where an LNA is loaded by an SRO, we can never make this assumption.

An SRO varies the tank conductance periodically between positive and negative values. The maximum sensitivity of the SRO is obtained at the critical point, when the total tank conductance is zero, as shown in Equ. 3.42. At this time point, however, the load resistance to the LNA is infinite. So we need a more accurate input impedance expression.

The exact input impedance of the circuit shown in Fig. 5.20 is, after elaboration,

$$Z_{in} = \frac{1}{j\omega C_{gs}} + j\omega L_s || \left(r_o + R_L\right) + \frac{g_m}{C_{gs}} L_s \left(\frac{r_o}{r_o + R_L + sL_s}\right), \tag{5.43}$$

where $||$ denotes "in parallel with". We can observe that when R_L is small, Equ. 5.43

simplifies to 5.42. On the other hand, when R_L becomes large, the real part of the input impedance decreases. At the critical point, when all the positive resistance given by the tank and the LNA are canceled, the input impedance has no real part. Intuitively, when the drain to ground resistance (R_L in this case) is infinite, no current is flowing into the drain and no current is flowing out from the source. Source degeneration, which utilizes the source current as a feedback, cannot be functional. We may expand this conclusion to all source current involved impedance matching techniques, such as a common-gate input stage.

The LNA load and input resistance changing with the quenching wave is plotted in Fig. 5.21. Our LNA designed so far has a differential output resistance of around 15.8 kohm. When the absolute value of tank resistance is much (10 times) smaller than 15.8 kohm, as denoted between the dashed lines in Fig. 5.21, the LNA is matched to the input.

Improving the performance further to achieve input impedance matching at critical point is fundamentally difficult. At the output side, to drive an infinite resistance, a voltage output should be used. But low output impedance loads the tank and brings down the Q factor, which involves several dimensional trade-offs. At the input side, we need a low impedance to load the output of the LNA in order not to influence the input matching. This implies that a current buffer should be inserted in, between the LNA and the SRO. This implication justifies the cascoding applied in the first place. Further cascoding does make the LNA more unilateral, but increased power consumption outweighs the benefit.

5.4.5.2 Neutralization

A simple inductive degeneration generates a real part of input impedance being proportional to the source inductor, L_s. However, the neutralization capacitors change the input impedance and destroy the proportionality. As a result, a maximum of input resistance exist.

A simple way to show the effect is to observe the current flow through gate-drain and neutralization capacitances, as shown in Fig. 5.22. Assuming

$$v_{g1} = -v_{g2} = v_g \tag{5.44}$$

$$v_{d1} = -v_{d2} = v_d \tag{5.45}$$

and

$$C_{gd} = C_n = C\,, \tag{5.46}$$

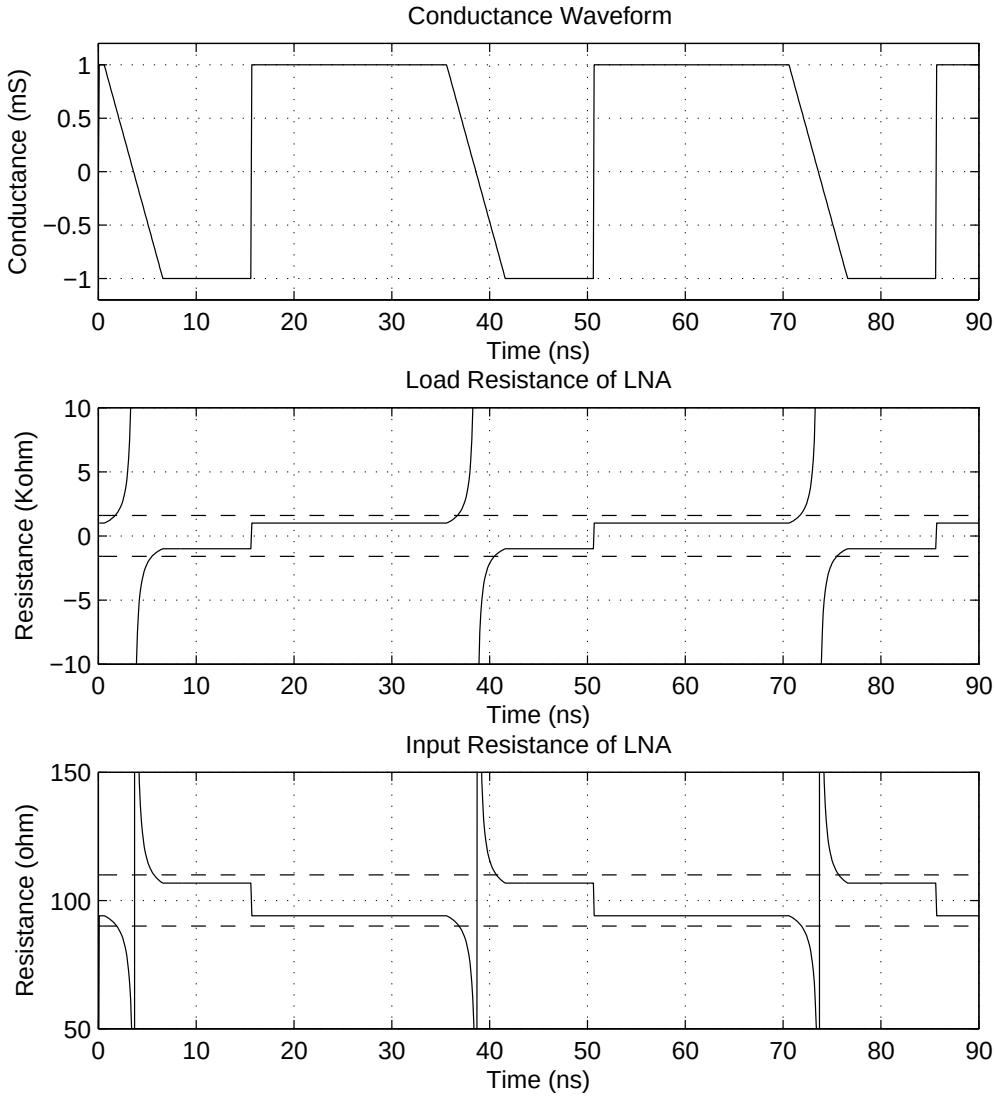

Figure 5.21: The variation of load and input resistance of LNA.

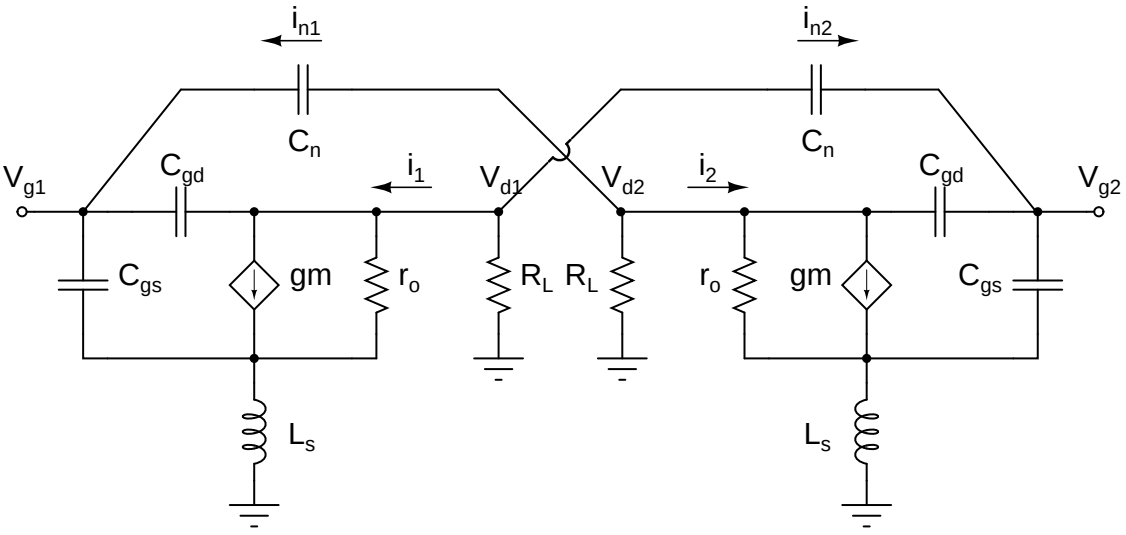

Figure 5.22: Neutralization Currents.

we have

$$
\begin{aligned}
i_1 &= (v_d - v_g)\, sC && (5.47)\\
i_{n1} &= (-v_d - v_g)\, sC && (5.48)\\
i_2 &= (-v_d - v_g)\, sC && (5.49)\\
i_{n2} &= (v_d + v_g)\, sC\,. && (5.50)
\end{aligned}
$$

Therefore, the current flowing out of node v_{g1} via capacitances C_{gd} and C_n is

$$i_{g1} = -i_1 - i_{n1} = 2v_g sC\,. \tag{5.51}$$

This extra current flow, i_{g1}, caused by C_{gd} and C_n , changes the input impedance of the LNA from Equ. 5.43 to

$$Z_{in} = \left[\frac{1}{j\omega C_{gs}} + j\omega L_s || \left(r_o + R_L\right) + \frac{g_m}{C_{gs}} L_s \left(\frac{r_o}{r_o + R_L + sL_s}\right)\right] \,||\, \frac{1}{2j\omega C}. \tag{5.52}$$

The input resistance of the LNA with and without the influence of C_{gd} and C_n (the real part of Equ. 5.42 and 5.52), as a function of the degenerated inductance, L_s, are plotted in Fig. 5.23. Two phenomena can be observed from the graph. Firstly, to achieve a certain matching resistance, neutralization requires a much larger L_s value. Secondly, C_{gd} and C_n cause a maximum of input resistance looking into the gate. Before this maximum happens, an increase of the source inductance, L_s, yields a proportional increase of gyrated gate resistance, as is predicted by Equ. 5.42 and 5.43. However, increasing L_s further after the peak of gate resistance can only reduce this resistance.

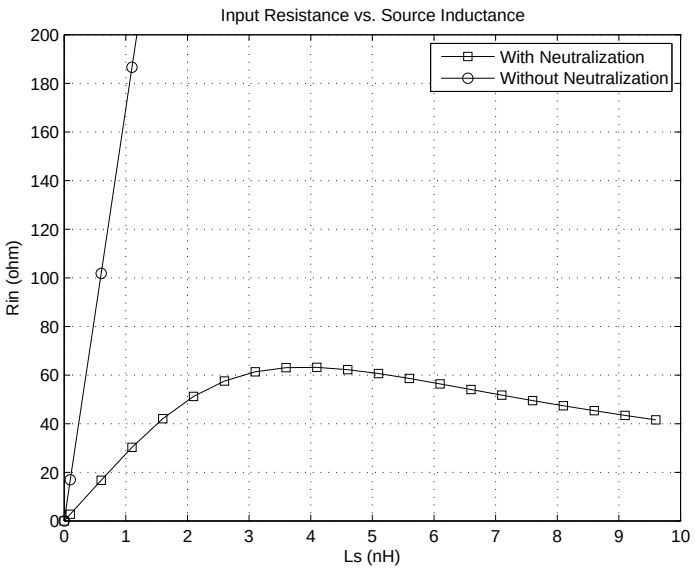

Figure 5.23: Input resistance vs. source inductance.

5.4.5.3 Low power, Low-Q Matching

Passive matching techniques can be divided into 2 categories, the narrow-band and wide-band matching. The narrow-band matching turns the center frequencies of all the cascading filters to the operating frequency. For low-loss networks, the insertion loss could be close to 0 dB at the center frequency. The drawback is that the bandwidth is determined by the Q factor of the network and the operating frequency. The wide-band matching, on the other hand, tunes the cascading filters away from the center in such a way that the stacked frequency response is flat in the passband. This type of matching techniques decouples the bandwidth dependencies on the Q factor and the operating frequency. The penalty paid is the insertion loss, which cannot be zero even if loss-less components are used. This LNA uses a narrow-band matching technique, which yields the smallest insertion loss for a given number of stages and the given quality of components.

In order to achieve the 500 MHz bandwidth, we need the Q factor of the matching network to be

$$Q = \frac{f_0}{BW} = \frac{4.5\,\text{GHz}}{500\,\text{MHz}} = 9. \tag{5.53}$$

Following analysis shows that this Q requirement is difficult to achieve for low-power LNAs.

The matching network and its equivalent simplified representation are shown in Fig. 5.24. In the schematic, L_b is caused by the bond-wire, which is specified as 2 nH. The bond-pad and ESD (Electrostatic Discharge) diodes are all capacitance paths to the ground, which constitutes parts of C_p'. C_p, another capacitor is added to C_p' so they resonate with L_b at the operating frequency. The Q factor of this L

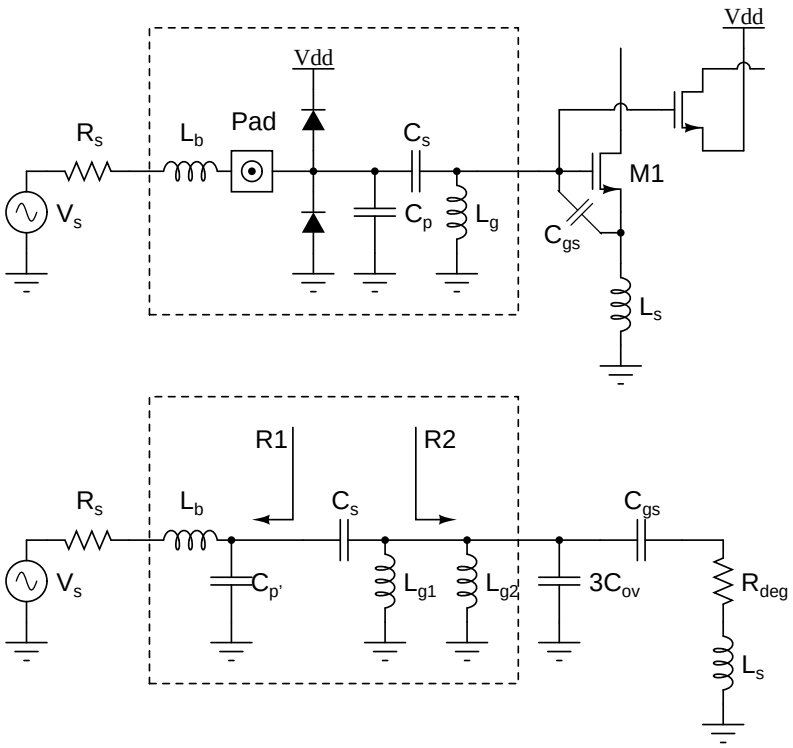

Figure 5.24: Matching network and its equivalent representation.

match is

$$Q_1 = \frac{\omega_0 L}{R_s} = \frac{2 \times \pi \times 4.5 \times 10^9 \times 2 \times 10^{-9}}{50} = 1.13. \tag{5.54}$$

The resistance looking to the source after this transformation, denoted as R_1, is

$$R_1 = R_s \left(1 + Q_1^2\right) = 50 \times \left(1 + 1.13^2\right) = 114\,\Omega. \tag{5.55}$$

At the input transistor's side, we split the shunt inductor L_g into L_{g1} and L_{g2} for interpretation purpose only. In Subsection 5.4.3, we have select the transistor's width to obtain a Q_2 of around 10 when $R_{deg} = 50\,\Omega$. This can be transformed into an equivalent parallel resistance of

$$R_2 = R_{deg} Q_2^2 = 5\,\mathrm{k}\Omega. \tag{5.56}$$

The rest of the network transforms this 5 kohm resistance down to 114 ohm, then the matching is done. This transformation network, C_s and L_{g1} should have a Q factor of

$$Q_3 = \sqrt{\frac{R_2}{R_1}} = 6.62\,, \tag{5.57}$$

which requires the inductor to be

$$L_{g1} = \frac{R_2}{\omega_0 Q_2} = 26.7\,\mathrm{nH}. \tag{5.58}$$

L_{g2} is resonating with the input capacitance of the transistor at 4.5 GHz, which is

$$L_{g2} = \frac{1}{\omega_0^2 C_{in}} = 14.2\,\text{nH}, \tag{5.59}$$

where

$$C_{in} \approx 3C_{ov}||C_{gs} = 88\,\text{fF} \tag{5.60}$$

is the input capacitance looking into the gate of M1. The total inductance of L_g is then

$$L_g = L_{g1}||\,L_{g2} = 9.3\,\text{nH}. \tag{5.61}$$

The preceding analysis argues that using loss-less components and fairly unlimited values, the minimum-power LNA satisfying all the specifications are feasible. However, two practical problems destroy this feasibility. First of all, the limited Q factor of L_g jeopardizes the gain and the noise figure of the LNA. For example, an inductor of Q=20 yields an equivalent shunt resistance of 5.25 kohm, which is nearly equal to the input resistance, R_2, calculated in Equ. 5.56. This leads to a 3 dB decrease of signal power and a 1.76 dB increase of noise power. This implies a 3 dB gain reduction and 4.76 dB noise figure degradation. Secondly, one inductor's value, $L_g = 9.3$ nH, is prohibitively large. It is worth mentioning that using a shunt-inductor topology has yielded the minimum inductance possible, since the 2 inductors, L_{g1} and L_{g2} are in parallel. Even if the large physical dimension is tolerable, a symmetrical inductor of 18.6 nH has too low a self-resonant frequency to be of any use.

The fundamental cause of these problems is the small power consumption and thus the small C_{in}. If power is doubled, i.e. C_{in} is doubled, then L_{g2} is halved, R_2 is quartered and L_{g1} is thus halved, according to Equ. 5.59, 5.56 and 5.58, respectively. Therefore, we are dealing with the ultimate power-gain-noise trade-off, but from a power-aware perspective. We increase the width of the input MOSFETs and biasing current to increase the gain and decrease the noise figure until they satisfy the LNA specifications. Adequate performance is achieved when the biasing is twice as much as the minimum derived in Subsection 5.4.3.

5.4.6 ESD Protection

Electrostatic discharge is considered at the beginning of the design of the matching network. The total capacitance between the chip-input to the ground, shown as C_p' in Fig. 5.24, is resonating with L_b at 4.5 GHz. So it has a value of

$$C_p' = \frac{1}{\omega_0^2 L_b} = 625\,\text{fF}. \tag{5.62}$$

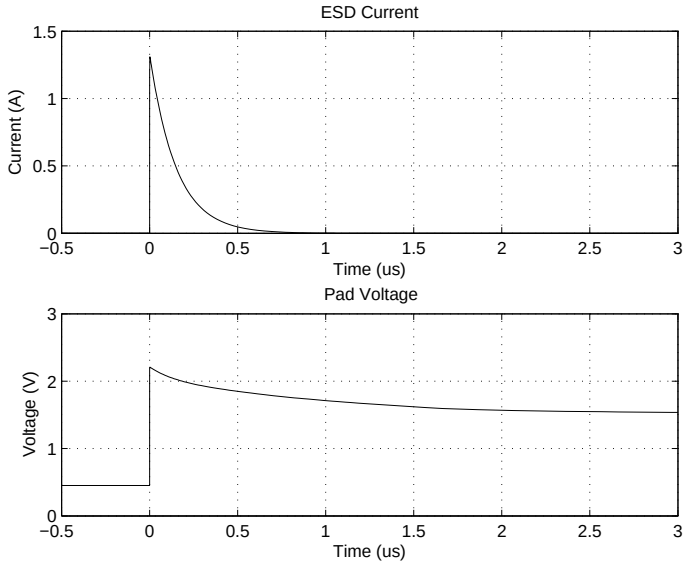

Figure 5.25: The transient voltage and current of an ESD event.

The smallest C4 bond-pad, having a dimension of 85×85 um, accounts for 50 fF. The parasitics of C_s also take several fF. The rest capacitance budget is given to ESD devices.

We utilize the double-diode ESD protection scheme with minimum dimension for its minimum additional capacitance. A 2 kV HBM (Human Body Model) ESD event is applied to the input and ground. The voltage at the input node and the current flowing through the diodes are plotted in Fig. 5.25. We can observe a maximum current of 1.3 A and a maximum voltage of 2.2 V.

The gate-dielectric integrity is verified according to IBM's technology design manual [33]. For a product lifetime of 100 KPOH (thousand of power-on hours), a maximum temperature of 85 °C, an area of gate oxide of 2×60um $\times$ 100nm and a gate-biasing voltage of 594 mV, this protection scheme can withhold a total amount of 18 minutes of this type of ESD events.

The same ESD event applied between the input and the V_{dd} is also verified with no gate-oxide breakdown.

5.4.7 Simulation Results

The s-parameter simulation is performed to verify the gain, matching and reverse isolation of the LNA.

The S11 of the LNA from 4 to 5 GHz is shown in Fig. 5.26. It can be observed from the plot that the LNA is matched well at 4.5 GHz, with an S11 of -37.5 dB. At 4.25 and 4.75 GHz, the S11 is 5.3 and 6.5 dB, respectively. S11 is not matched to -10 dB in the whole 500 MHz bandwidth since low power low-Q matching involves a

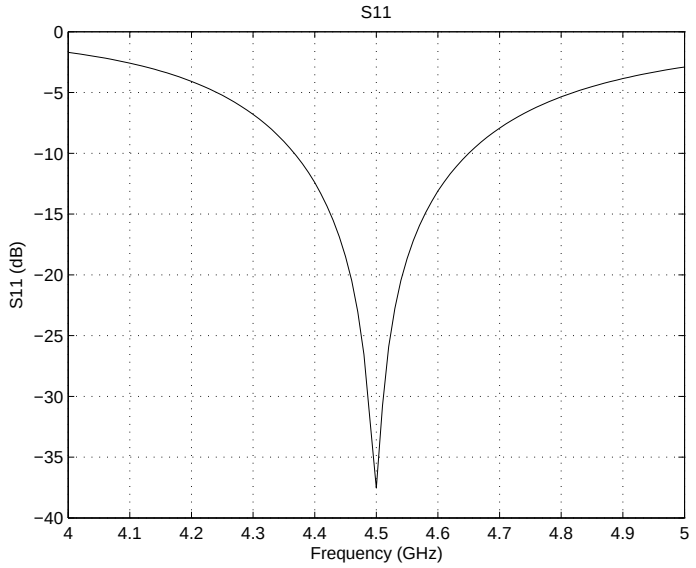

Figure 5.26: Input port reflection coefficient, S11.

trade-off, discussed in Subsection 5.4.5. Instead, signal is allowed to be attenuated to 50% of its power at the edge of the bandwidth. The -3 dB S11 happens at 4.13 GHz and 4.99 GHz frequency. Hence, for a low-loss input matching network, the -3 dB bandwidth is around 860 MHz.

The forward power gain, S21, is plotted in Fig. 5.27. As shown in the graph, a maximum gain of 16 dB is obtained at the center frequency, which indicates an LNA transconductance of 20 mS. The -3 dB bandwidth is around 220 MHz, limited by the load of the LNA. This bandwidth barely means that the load resonant tank has a Q factor of

$$Q = \frac{f_0}{BW} = \frac{4.5 \text{ GHz}}{220 \text{ MHz}} = 20.5 \,. \tag{5.63}$$

The reverse power gain of the LNA is shown in Fig. 5.28. As shown in the graph, a minimum of 52 dB reverse isolation is obtained, satisfying the S12 $<$ -39.4 dB specification. This performance guarantees that the ETSI spurious emission limitation is satisfied.

The noise figure of the LNA is shown in Fig. 5.29. As shown in the graph, the minimum noise figure of 2.5 dB is achieved at 4.5 GHz. At 4.25 and 4.75 GHz, the noise figure is 2.9 and 2.8 dB, respectively.

Two current paths each draws 1.22 mA from the 0.9 V supply. Therefore, the LNA consumes 2.2 mW power. This continuous power consumption can be reduced by duty cycling using an auxiliary circuit, which biases the LNA dynamically during the SRO sampling period and turns it off during the quenching period.

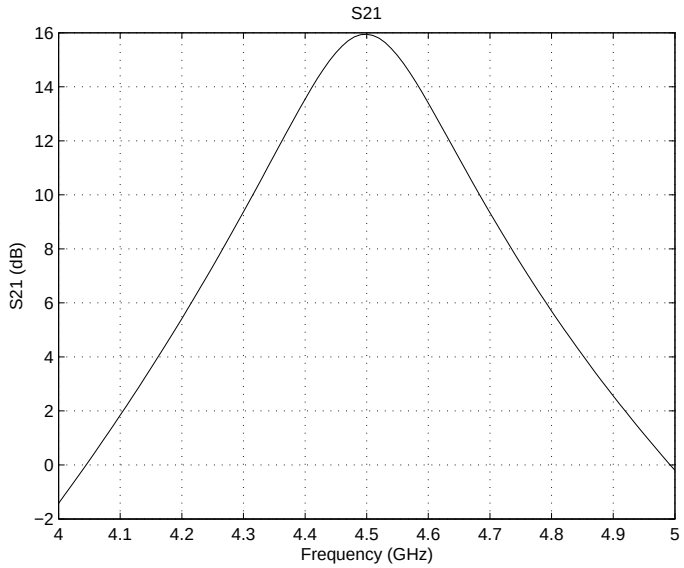

Figure 5.27: Forward power gain, S21.

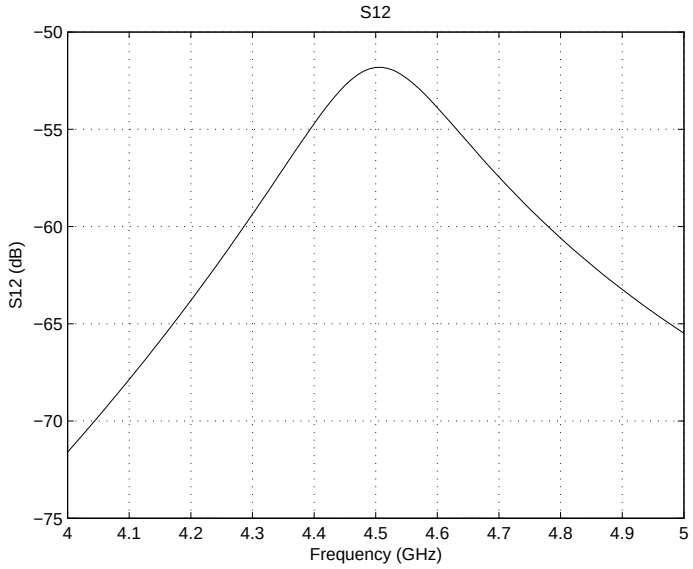

Figure 5.28: Reverse power gain, S12.

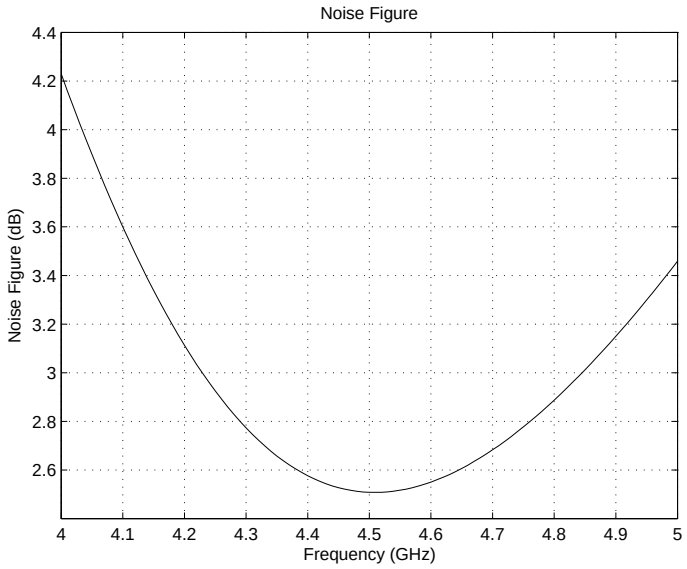

Figure 5.29: The noise figure of the LNA.

Chapter 6

Auxiliary Circuits

6.1 Introduction

Super-regenerative receivers need auxiliary circuits to work properly. First of all, every SRO needs a time-varying biasing. The complexity of biasing circuits depends on the waveform to be applied to SROs. To obtain the desired FM-AM conversion, a large voltage swing and low-power dissipation, this design uses a special waveform which complicates the biasing circuit considerably. Secondly, power reduction is possible if the LNA is shut down during the quenching period. Super-regenerative receivers are inherently sampling circuits which deal with only discrete time signals. LNA is only useful in certain periods to provide gain and matching. At the rest of the time, it can be put to rest for power saving consideration as long as its reverse isolation is not compromised. Thirdly, a voltage buffer is required to output the demodulated subcarrier. This stage is mainly designed for testing and measurement purpose. Oscilloscopes are assumed to be the load. Lastly, an on-chip current reference circuit is designed for the biasing of all the functional blocks.

The detailed design of the biasing waveform generator for SRO, the dynamic biasing circuit for LNA, the output buffer and the current reference are presented in Section 6.2, 6.3, 6.4 and 6.5, respectively.

6.2 Biasing Waveform Generator for SRO

The biasing waveform generator produces the saw-tooth like current waveform specified in Subsection 5.2.4 to bias the SRO. We assume that an external clock is available. The duty cycle of the clock should be tunable in order for the SRO to have a variable gain. The peak of biasing waveform is also designed to be externally tunable, so that the external control of the oscillation amplitude, gain, and frequency response of the SRO is possible after the fabrication.

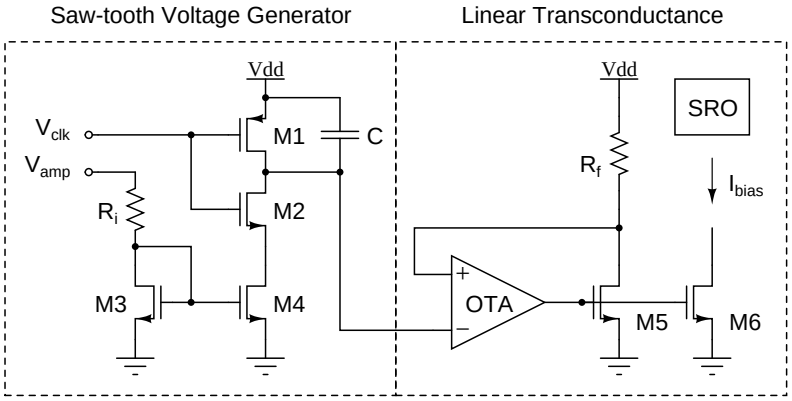

Figure 6.1: The schematic of the biasing waveform generator.

6.2.1 The Schematic

The circuit of this biasing waveform generator is shown in Fig. 6.1. In essence, the circuit first converts the external rectangular clock signal into a saw-tooth voltage waveform, which is then converted into a current waveform by a linear transconductance block.

6.2.2 Saw-tooth Voltage Generator

The saw-tooth voltage is derived from an external rectangular clock using the left half of the circuit shown in Fig. 6.1. The circuit consists of a capacitor, 2 switches M1 and M2, a resistor R_i and a current mirror formed by transistor M3 and M4.

An external DC voltage V_{amp} is converted to a DC current by R_i. The current is then duplicated to the switched-capacitor circuit by the current mirror. On a positive period of the clock, M1 is open and M2 is closed. The capacitor, C, is charged by the DC current, and the voltage across the capacitor is growing linearly with time. When a positive to negative transition of the clock occurs, M2 becomes open and M1 is closed, which short-circuits the capacitor and discharges it sharply. This short is continued until the next positive cycle begins. In this way, the shape of the quenching waveform described in Fig. 5.5 is generated in a voltage form, as shown in the second row of Fig. 6.4.

The amplitude of the saw-tooth waveform can be controlled by the external voltage V_{amp}. A large voltage yields a large current charging the capacitor, and for a given period, a large ramp amplitude, and vice versa.

6.2.3 Linear Transconductance

The linear transconductance converts a voltage into a current with the shape of the waveform preserved. The circuit is shown in the right part of Fig. 6.1, which

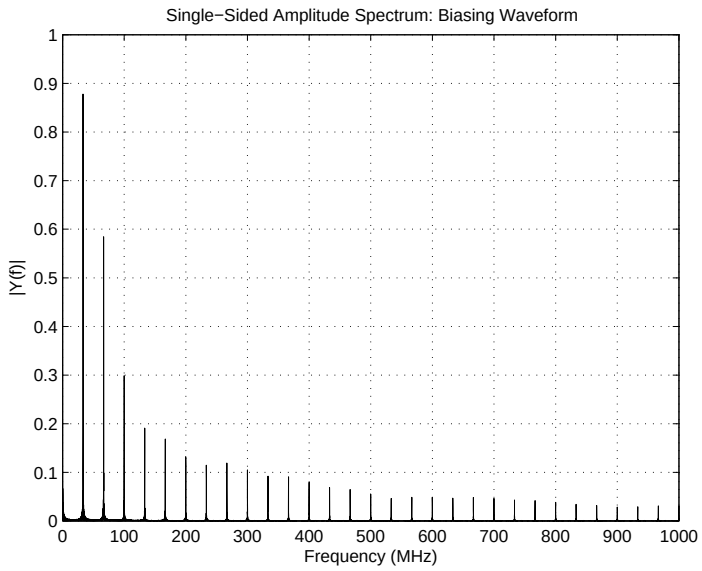

Figure 6.2: Amplitude spectrum of the biasing waveform.

consists of a resistance R_f, an operational transconductance amplifier (OTA) and a current mirror formed by MOSFETs M5 and M6.

The OTA, transistor M5 and R_f form a negative feedback loop. For a given gate voltage of M5, a current is generated. Resistor R_f converts this current into a voltage and feeds it back to the positive input of the OTA. If this voltage is higher than the voltage across the capacitor, the OTA applies a positive incremental voltage to the gate of M5, which yields an increased current and a reduced voltage at the positive input of the OTA. In this way, the negative feedback linearize the transconductance of M5, and a transconductance of

$$GM = \frac{I_o}{V_{in}} \approx \frac{1}{R_f} \tag{6.1}$$

is obtained, when the loop-gain is large. Transistor M6 accurately duplicates this current to bias the SRO.

6.2.4 OTA Design

In the biasing waveform generator shown in Fig. 6.1, the main power consumer is the OTA. Therefore, the design goal for this OTA is to minimize the power while achieving the performance requirements.

6.2.4.1 Specification

The power of an OTA is determined by its gain-bandwidth product. For a cascode structure, the DC gain is a fairly constant value while the bandwidth is not. So

we need to specify the minimum bandwidth requirement for the OTA. A discrete Fourier transform yields the amplitude spectrum of the saw-tooth biasing waveform. Its normalized version is plotted in Fig. 6.2. As can be observed from the graph, the main power of the biasing waveform is concentrated in frequencies below 500 MHz. Therefore, we use a 500 MHz bandwidth, i.e.

$$BW = 500 \text{ MHz}, \tag{6.2}$$

as our design specification for the closed-loop linear transconductance. A smaller bandwidth leads to waveform distortion and less controllability of the SRO.

Assuming a single-pole behavior, the gain of the OTA is expressed as

$$A_v = \frac{A_{DC}}{1 + j\frac{f}{f_c}}, \tag{6.3}$$

where A_{DC} and f_c are the DC-gain and -3 dB bandwidth, respectively. Then the close-loop transfer function is

$$GM_{cl} = -\frac{A_v g_m}{1 + A_v g_m R_f} = \frac{A_{DC} g_m}{1 + A_{DC} g_m R_f + j\frac{f}{f_c}}, \tag{6.4}$$

where g_m is the small-signal transconductance of M5. The bandwidth of the closed-loop transconductance is

$$BW_{-3dB} = (1 + A_{DC} g_m R_f)\, f_c = 500 \text{ MHz}. \tag{6.5}$$

Assuming a cascode topology is going to be used and an intrinsic gain of 10 is available for this technology, A_{DC} is around 100 or 40 dB. Since the output current of M5 is a biasing waveform, g_m is signal dependent and time-varying. To simplify the calculation, we further assume that the loop-gain is mainly supplied by the OTA, i.e.

$$g_m R_f \approx 1. \tag{6.6}$$

Then the bandwidth specification for the OTA can be calculated as

$$f_c \approx \frac{BW_{-3dB}}{1 + A_{DC}} = 5 \text{ MHz}. \tag{6.7}$$

Equ. 6.6 determines a trade-off between the power consumption and tracking errors at the start of ramps. If we assume $g_m R_f \ll 1$, we need a fast OTA with large f_c, consuming quite some power. On the other hand, if we assume $g_m R_f \gg 1$, it is invalid at the starting up of a ramp, since the drain current of M5 is small, so is the transconductance, g_m. In this period, the loop-gain is severely overestimated and a

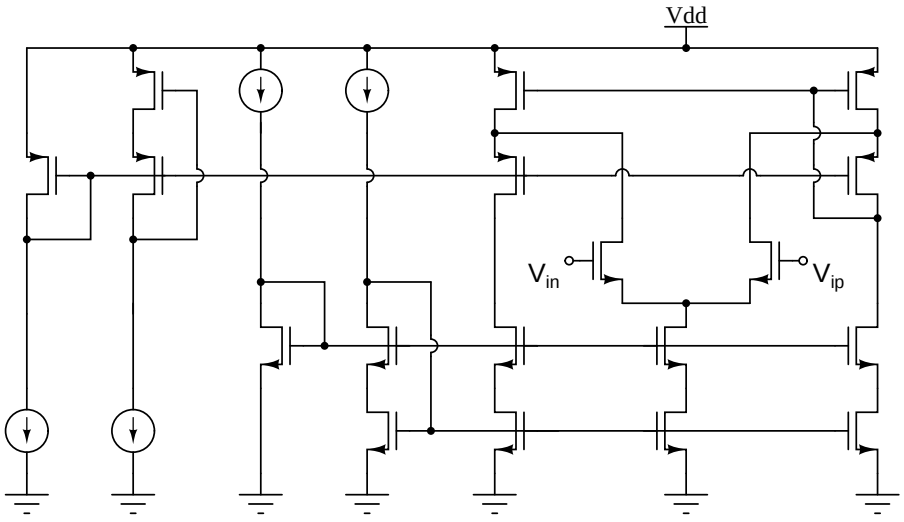

Figure 6.3: The schematic of the OTA.

current slope deviating from its voltage reference can be observed. The simulation result showing this effect is plotted in Fig. 6.4.

6.2.4.2 The schematic

The schematic of the OTA is shown in Fig. 6.3. In essence, the folded cascode structure is used for its high gain compared with those using uncascoded current sources as loads. Since the input voltage ranges from 500 mV to 900 mV, a pair of NMOSs is used for the input.

The lengths of all the transistors are scaled to 200nm for the improved intrinsic gain and reduced threshold voltage. All transistors are biased in moderate inversion to balance the speed and power consumption. More specifically, a gm/Id of 15 is selected, which yields a current density of 10 uA/um and a transit frequency of 1 GHz. The NMOS transistors have a basic width of 10 um except the input ones, which are 40 um wide. PMOSs are 3 times larger in width. As a result, 100 uA is consumed in each current path. A total current consumption is 400 uA.

6.2.5 Simulation Results

A transient simulation is performed and the result of the external clock, saw-tooth voltage, op-amp virtual ground, the gate voltage of the tail current source and the biasing voltage for the SRO are shown in Fig. 6.4. The amplitude control voltage, V_{amp}, is set to 700 mV.

From the saw-tooth waveform at the second row, we can observe the charge-injection effect caused by the small capacitor and comparatively large switches. The small capacitor is desirable since a small current is needed to charge it. Large switches are used so that the conducting resistance is small. Charge injection is not

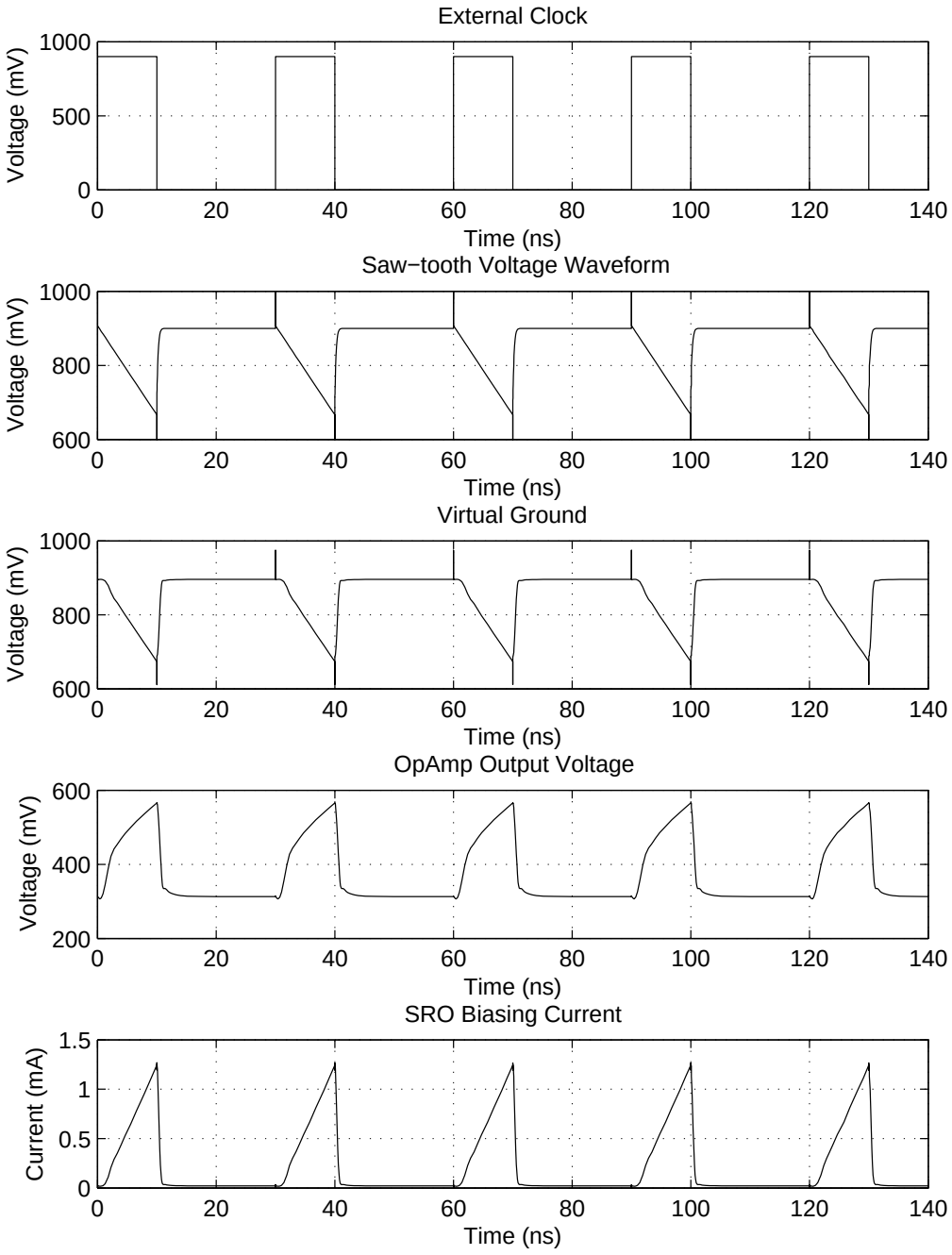

Figure 6.4: Transient simulation result of the biasing waveform generator.

a serious issue in this application because the continuous charging and discharging current conducts the charges quickly and the limited bandwidth of the feedback loop filters the sharp pulses.

By carefully inspecting the biasing current waveform shown in the bottom of Fig. 6.4, a slope deviation can be observed at the starting part of a ramp. This effect is caused by the small transconductance of M5 and M6 when the biasing voltage at their gates is low. At this phase, Equ. 6.6 is not satisfied and the loop-gain of the transconductance loop is small, yielding this tracking error. Careful simulations are performed to formulate Equ. 6.6 in such a way that the tracking error only appears *before* the SRO is reaching its critical point. So the biasing slope *at* the critical point is not influenced by this tracking error.

The op-amp constantly drains 408 uA from the 0.9 V power supply. The current sensor path (R_f and M5), op-amp biasing and the switched capacitor consume 26 uA, 10 uA and 4 uA, respectively. As a result, a total power of 403 uW is consumed.

Two measures can be taken to trade performance off for less power. Firstly, the 500 MHz bandwidth specified in Equ. 6.2 can be compromised, which leads to significant waveform distortion. Secondly, we can assume that the gm of M5 has a larger contribution to the loop gain by violating Equ. 6.6, which causes larger slope deviation at the starting part of a ramp. Both measures degrade the controllability of the SRO.

The power dissipation of this biasing circuit is 1.6 times as large as that consumed by the SRO. This extra power consumption, caused by the complex saw-tooth current generator brings us back to the selection of the biasing waveform for the SRO. Although we intend to save power by using a slope-controlled SRO, its complex biasing causes power overhead that outweighs the benefit. An SRO working in step-controlled state is, under the circumstances, worth a try (see Section 7.3).

6.3 Dynamic Biasing for LNA

LNAs used in super-regenerative receivers do not need to work all the time. SROs are sampling amplifiers, which amplify only a portion of the signal in a certain period. For the power-saving purpose, LNAs can be turned off when SROs are in the quench period or when oscillations have already been built up.

6.3.1 LNA Minimum Start-up Time Analysis

An LNA cannot share the same clock with an SRO in a receiver. As analyzed in Chapter 3, the maximum sensitivity of an SRO happens at the clock transition point. Signals right before a transition are at least as important as they are after

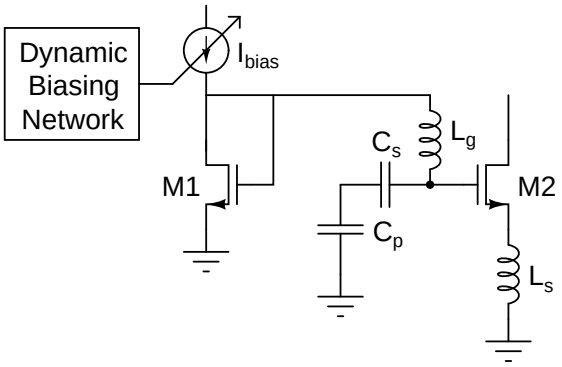

Figure 6.5: The equivalent biasing network for LNA.

the transition. So an LNA should start working before an SRO is turned on.

How long an LNA should start before an SRO depends on the characteristics of both of them. Intensive analysis in Chapter 3 deals with the sensitivity curve of SROs. This subsection analyzes the warm-up time of the LNA introduced in Section 5.4.

The schematic involving the dynamic biasing of the LNA is shown in Fig. 6.5. Transistor M2 is the input stage of the LNA. Inductors L_s and L_g and capacitors C_s and C_p are used for input power matching. Transistor M1 is a part of a current mirror, which feeds the biasing voltage through L_g to the gate of M2. The biasing current source is controlled by switching events and thus it can be treated as a step stimulus.

When a steep power-up current is generated, it faces 2 paths. The first path is the resistance of the diode-connected MOSFET M1, which is around $1/g_m$. The second path is formed by RF components L_g, C_s, C_p, L_s and parasitics of M2. At high frequencies, this second path has a lower impedance than that of M1. So the initial part of the power-up current is bypassed, without generating a voltage through M1.

A slow warm-up is undesirable. However, to accelerate this process is difficult since the bypassing components are also parts of the power matching network, which should not be modified. Simulation result (plotted in the bottom of Fig. 6.11) shows that the warm-up time of the LNA is around 5 ns.

6.3.2 Dynamic Biasing Circuit

The circuit, which periodically turns off the LNA, is plotted in Fig. 6.6. Because the prestarting of the LNA is required, a delay-line is created to provide a time constant internally without referencing to another clock.

The whole circuit consists of a ramp voltage generator, a comparator, a NOT and a NAND gate to deal with logics, and a switch, M6, to quench the current

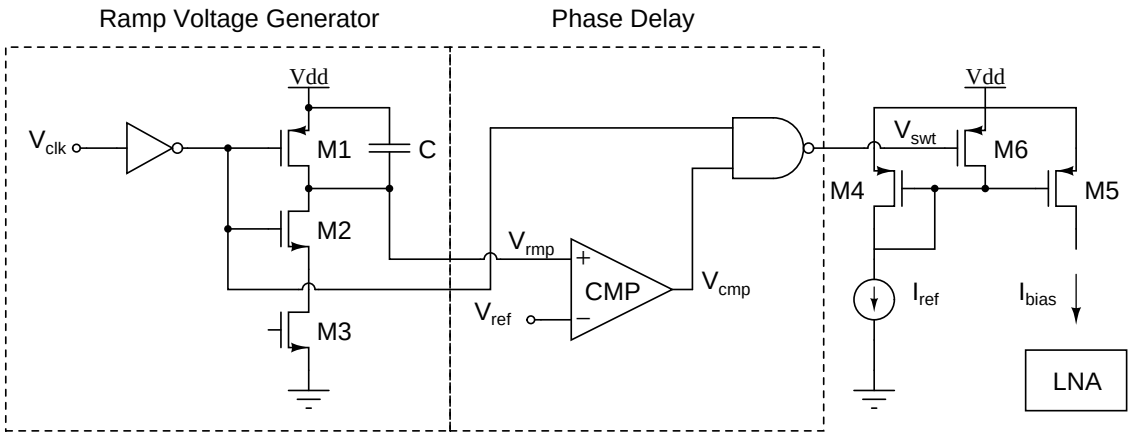

Figure 6.6: The schematic of the dynamic biasing network for LNA.

mirror.

The ramp voltage generator converts the negative portion of the clock into a ramp. The detailed mechanism is identical with the other one discussed in Subsection 6.2.2.

The comparator constantly compares the voltage integrated by the capacitor to an external reference voltage, V_{ref}. By doing this, V_{ref} is able to control the amount of phase delay of the positive to negative transition edge.

The logics enforce the LNA to work at both the warm-up and the amplification period. The waveform of the node voltages are shown in Fig. 6.7. In the figure, V_{clk} is inverted at first. Then its quenching parts are converted to ramps, denoted as V_r. After that, the comparison between V_{ref} and V_r generates positive to negative transitions of V_{cmp}. It is these transitions that trigger the start-up of the LNA. Finally, the NAND combines the warm-up period and the working period of the LNA into one signal, V_{swt}, which controls the switch of the current mirror M6. When V_{swt} is positive, M6 is open, and the LNA works.

The physical dimension of the switch, M6, involves the trade-off between charge injection and current leakage. A large M6 has a small conducting resistance and the LNA is quenched completely. However, charge injection can be clearly observed. On the other hand, a small M6 has a relatively large on-resistance. When I_{ref} is flowing through this resistance, the voltage drop leads to a leaking current flowing in the LNA. A compromise between the two yields the dimension of M6 as L=100 nm and W=10 um.

6.3.2.1 Comparator

The schematic of the comparator is shown in Fig. 6.8. The input stage is an N-input differential pair with a current mirror as the load. Its main purpose is to provide gain. The second stage is an NMOS driving a PMOS current source. Extra gain

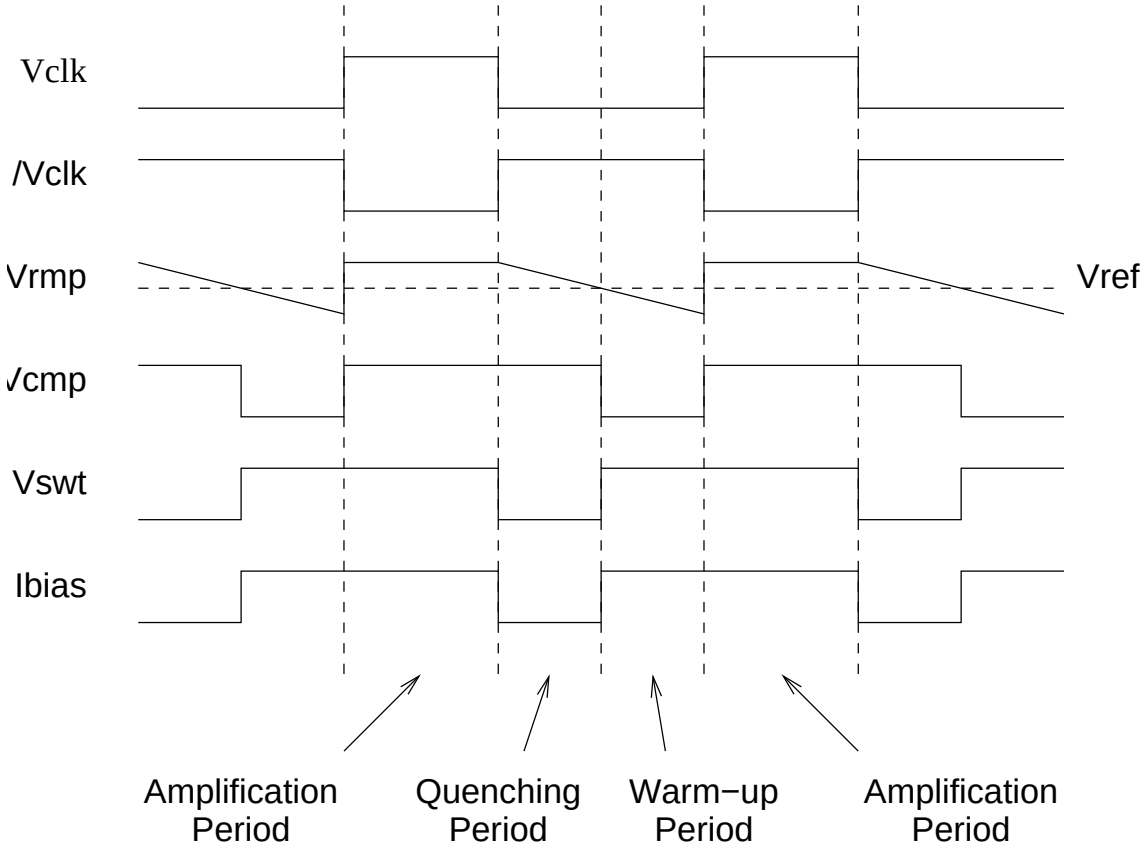

Figure 6.7: Dynamic biasing waveforms.

and a rail-to-rail voltage swing are provided by this stage. Since the load of this comparator is an NAND gate, which has a small dimension, the comparator also use small transistors (L=200 nm, W=1 um). Biasing current of 10 uA is consumed in each path. Thus, a total current consumption is 30 uA.

6.3.2.2 Logic Gates

The transistor level NOT and NAND gates are shown in Fig. 6.9. Since the inverter drives M1, M2 and the NAND gate, it has a width of 10 um for the NMOS and 20 um for the PMOS. The NAND gate only drives the switch M6, so it has the minimum dimension. Because NMOSs in the NAND gate is in series, they have the same width as the PMOSs.

6.3.3 Simulation Results

Simulations show that a V_{ref} setting from 900 mV to 580 mV yields an LNA turn-off period ranging from 0 to 20 ns, i.e. 16 mV/ns. After the LNA and the SRO are plugged in, simulations further show that a power-off period ranging from 0 to 17.5 ns produces almost identical SRO output amplitude compared with one another. For a 17.5 ns power-off, the control voltage, V_{ref} should be 620 mV.

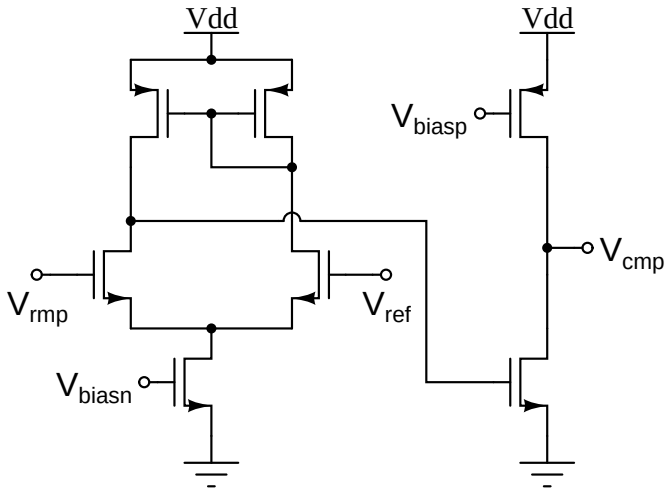

Figure 6.8: The schematic of the comparator.

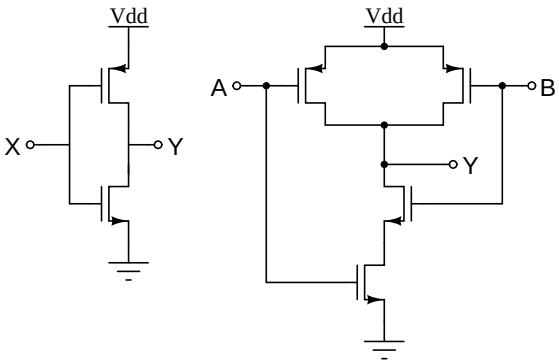

Figure 6.9: The schematic of the NOT and NAND gate.

The transient results of node voltages and the biasing current are plotted in Fig. 6.10 and 6.11. The simulation is performed at a control voltage of 620 mV.

Fig. 6.10 is the simulated version of Fig. 6.7, showing the external clock, the inverted clock, the voltage ramp, the comparator output and the switching signal.

Fig. 6.11 plots the switching signal again with the gate voltage of the mirror, the gate voltage of the input pair and the LNA current. The slow start-up behavior of the LNA, as analyzed in Subsection 6.3.1, can be clearly observed.

The power consumption of this dynamic biasing circuit consists of the static power, consumed by the first stage of the comparator and the current mirror, and the dynamic power, consumed by the logic gates, the switched-capacitor and the second stage of the comparator. All the dynamic power caused by gate switching is neglected in this analysis since the power supply voltage is low and the gates are small. The static current consumed is 30 uA, consisting of 20 uA by the first stage of the comparator and 10 uA by the current mirror of the LNA (M4 in Fig. 6.6). The average of the dynamic current consumed is between 5.7 uA to 11.4 uA, depending on the duty-cycle of the comparator output. In detail, the switched capacitor draws 5.7 uA in average and the second stage of the comparator draws 0 to 5.7 uA. In conclusion, this dynamic biasing circuit draws around 36-to-42 uA current from the 0.9 V power supply, which indicates a power consumption of 32-to-38 uW.

At a control voltage of 620 mV (the best power saving situation without performance degradation), the average biasing current of the LNA is 601 uA single-ended and 1.20 mA in total, compared with the 2.44 mA current consumption if the LNA is not quenched. Thus, 50.7% power reduction is obtained.

6.4 Output Buffer

The output buffer duplicates the oscillation envelope generated by the peak detector and drives external instruments.

6.4.1 Device Testability

This design takes the testability into consideration. Four control inputs, namely V_{clk}, V_{amp}, V_{frq} and V_{ref} are implemented for performance fine-tuning after fabrication. V_{clk} and V_{amp} fix the slope and amplitude of the quenching wave for SRO. Their combination controls the gain, sampling speed, output pulse shapes and frequency response of the super-regenerative receiver. V_{frq} is used to adjust the receiver's operating frequency. V_{ref} controls the warm-up time of the LNA. By tuning these inputs, the receiver can be configured to the optimum after fabrication.

Many of these postfabrication configurations need feedback. The ideal output

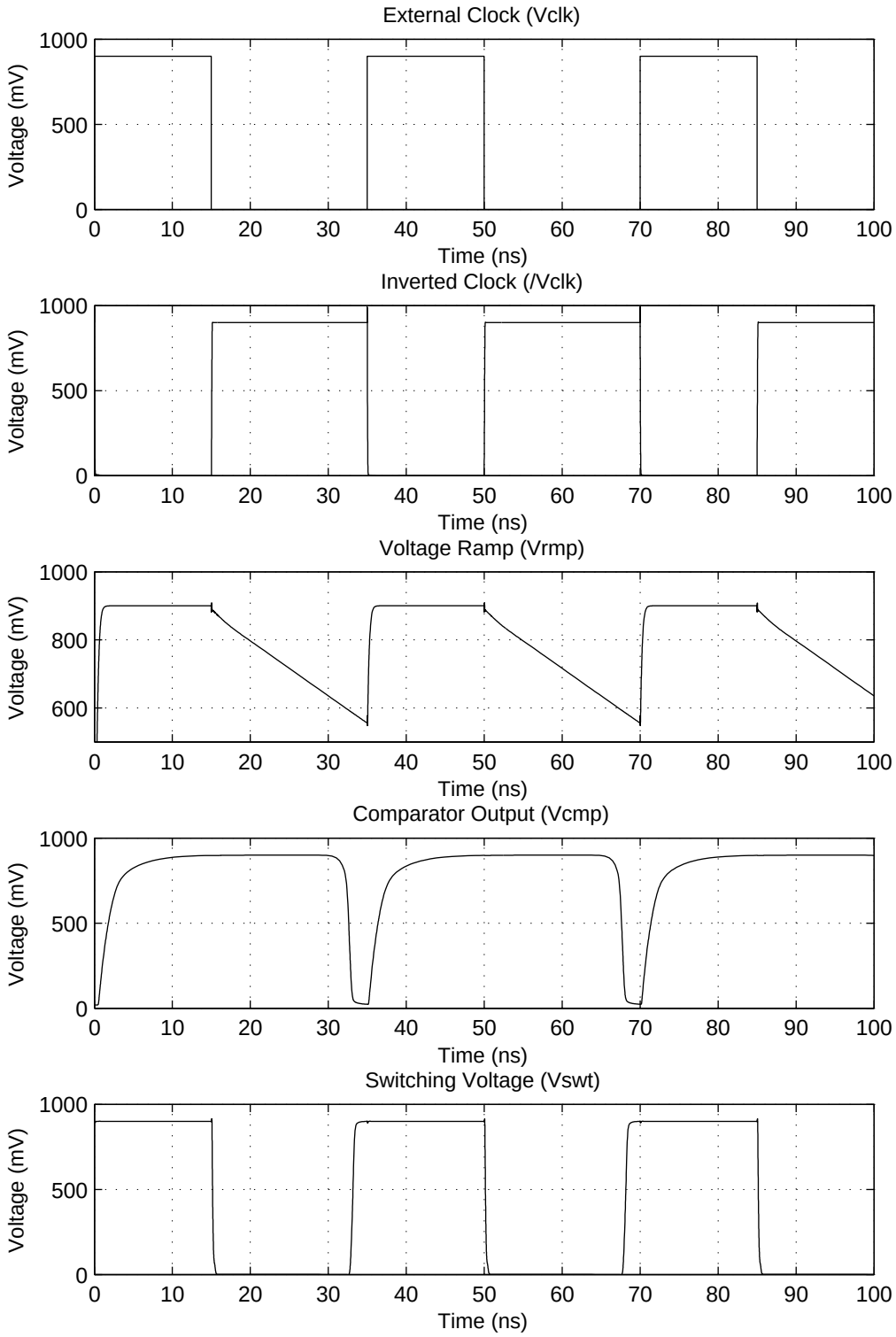

Figure 6.10: The transient simulation result of the dynamic biasing network.

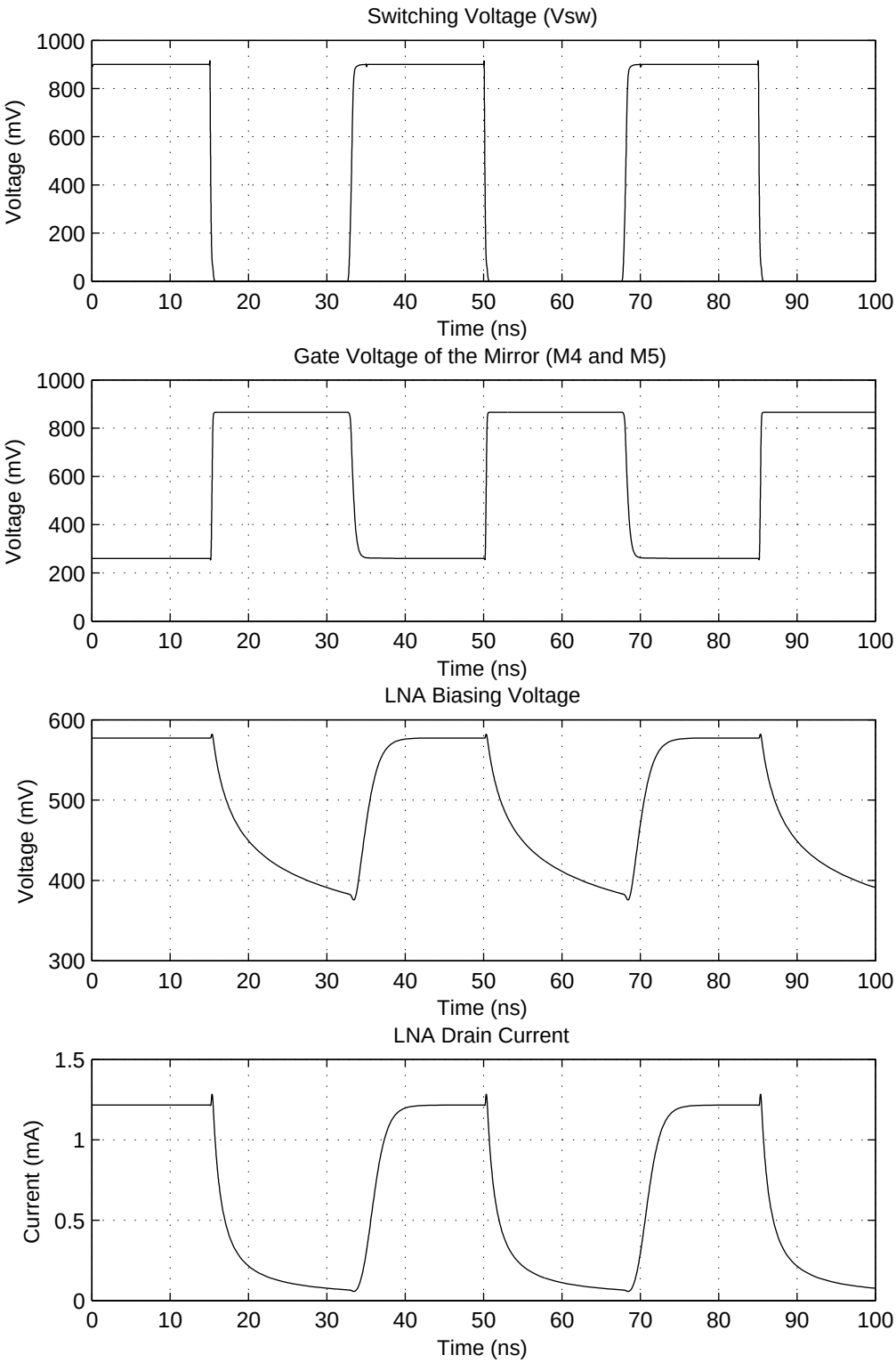

Figure 6.11: The transient simulation result of the LNA under dynamic biasing.

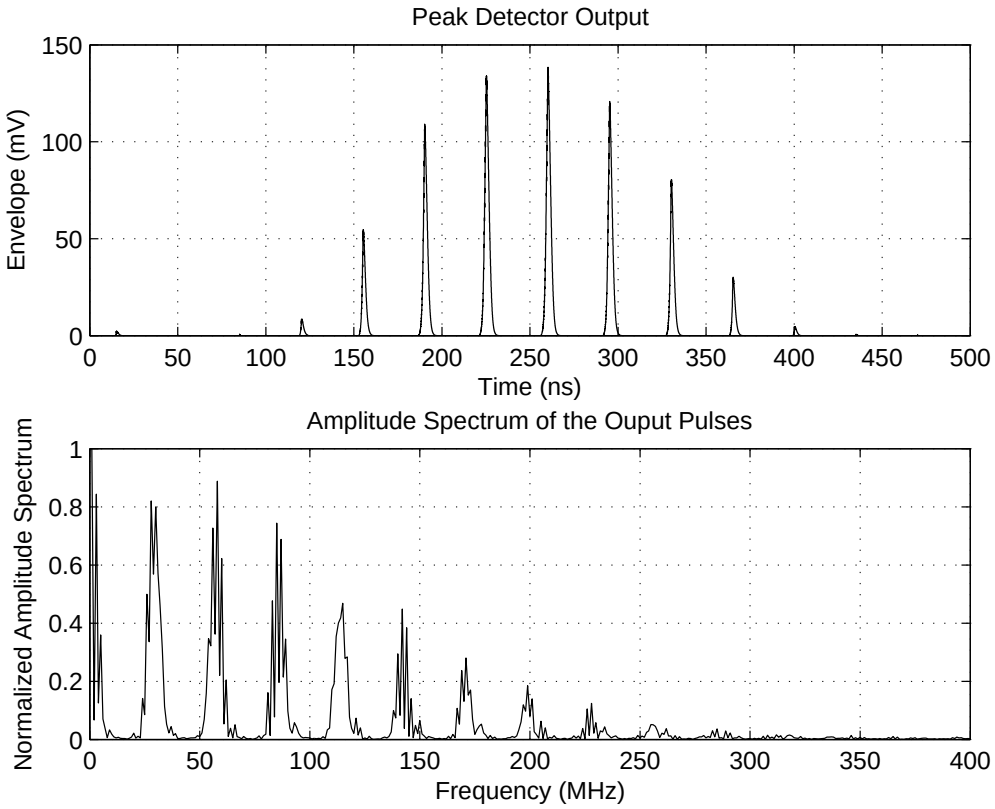

Figure 6.12: Output pulses and their power spectral density.

signal which contains abundant information is the pulses at the output of the peak detector. By observing this signal, the operating frequency, gain, pulse shapes, sampling speed and frequency response can all be deduced.

6.4.2 Design Objective

The output buffer is designed to amplify the weak signal from the peak detector to drive external instruments. Furthermore, it should be able to shield the instruments from influencing the operation of the receiver.

The output signal to be buffered is plotted at the top of Fig. 6.12. It can be observed that a maximum voltage swing of 150 mV is required for the output buffer. By performing a discrete Fourier transform to the output signal, its normalized amplitude spectrum is plotted at the bottom of Fig. 6.12. As shown in the graph, a bandwidth of around 300 MHz is needed to preserve most of the output signal power.

The signal source, i.e. the peak detector, has a specific output capacitance of 100 fF, which should not be influenced. Otherwise, the discharge time constant of the peak detector would be modified and a reduced conversion gain and slow tracking behavior could be observed.

At the load side, the input impedance of measurement instruments is specified as 10 kohm resistance in parallel with 20 pF capacitance.

6.4.3 The schematic

The schematic of the output buffer is shown in Fig. 6.13. It is a 2-stage Op-amp with unity-gain feedback.

The first stage is a folded cascode OTA with NMOS input differential pair. We choose a folded cascode input for its large gain compared with single differential pair and small voltage headroom requirement compared with a telescopic structure. The NMOS input pair is chosen since the input biasing is relatively high, around 570 mV.

The second stage is an NMOS common source with a PMOS current source. The main purpose of this stage is to drive the 20 pF capacitive load. A source follower is not used in this design since the limited voltage swing of the previous stage and the voltage shift prevents the output-to-input connection.

The lengths of all the transistors are scaled to 200nm for the improved intrinsic gain and reduced threshold voltage. All transistors are biased in moderate inversion to balance the speed and power consumption. More specifically, the overdrive voltage is selected to obtain a gm/Id of 15, which yields a current density of 10 uA/um and a transit frequency of 1 GHz. The second stage has a width of 600 um (1800 um for the PMOS), in order to have a biasing current of 6 mA and a slew rate of 0.3 V/ns. The first stage is a 3 times scaled version of the OTA designed in Subsection 6.2.4 to drive the second stage with reasonable speed.

Miller compensation is performed to achieve a phase-margin of 60 degrees. In detail, a 1.81 pF capacitor is plugged in, shown as C_c in Fig. 6.13.

The input capacitance of this buffer stage is around 128 fF, slightly larger than the 100 fF capacitor used in the peak detector. Simulations show that the substitution of the 100 fF capacitor used in the peak detector by this 128 fF input capacitance of the buffer yield indistinguishable results.

The buffer amplifier has its own power supply so that the power consumption of this buffer and the receiver can be measured separately.

6.4.4 Simulation Results

An AC small-signal analysis yields the open-loop amplitude and phase response after the frequency compensation, plotted in Fig. 6.14. As shown in the graph, a phase margin of 60 degree is obtained.

A transient simulation is performed, and the voltage output of the peak detector and the buffered version are plotted in Fig. 6.15. From the graph, nearly identical

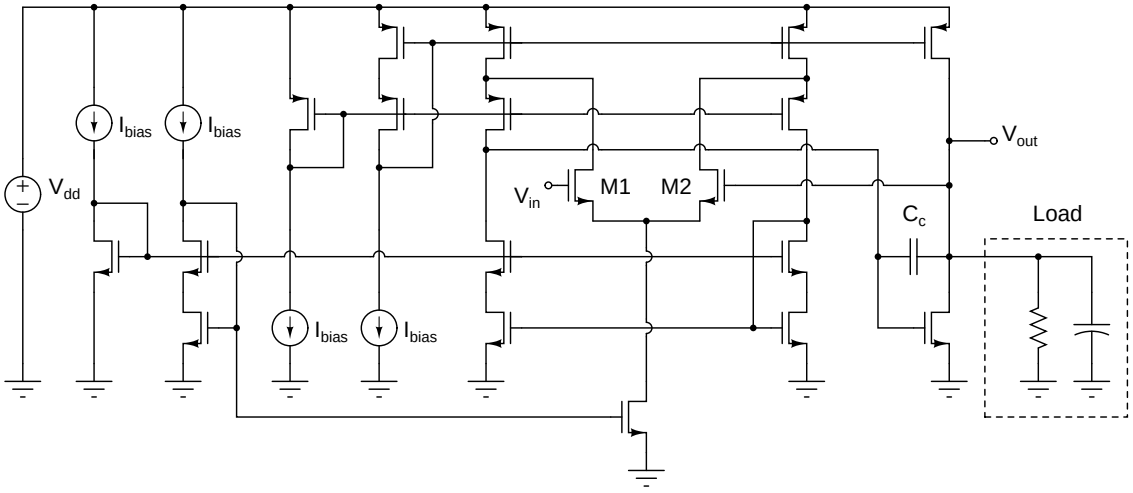

Figure 6.13: The schematic of the output voltage buffer.

waveforms are observed.

This output buffer draws 9.86 mA from a 0.9 V power supply, i.e. a power consumption of 8.87 mW.

6.5 Current Reference

The biasing currents of all the circuit blocks are provided by an on-chip current reference.

6.5.1 The schematic

A peaking current source is used in this design, as shown in Fig. 6.16. Essentially, M1 and its K times scaled up version, M2, have a square-law I-V relationship, so the voltage between their gates are nonlinearly depending on their drain currents, which are forced to be equal by a current mirror (M3 and M4). On the other hand, the resistor, R, has a linear I-V relationship. In order for the voltage between the gates of M1 and M2 and the voltage across the resistor to be equal, the drain current of M1, or M2, has to be a certain value (besides zero), defined by the cross point of the nonlinear curve and the linear one. M5 is a start-up device which guarantees a current flow at zero condition. The capacitor, C, bypasses voltage variation caused by noise and filters ringing at the start-up phase.

The design parameters for this circuit are:

R the resistance value

K the ratio of M2's W/L to M1's W/L

W/L the width-to-length ratio of M1.

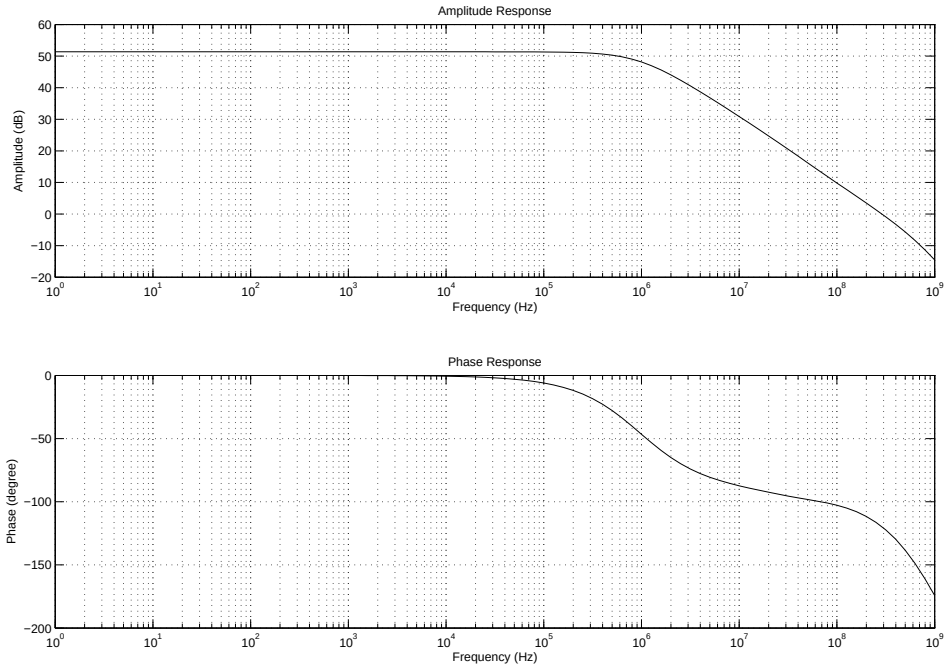

Figure 6.14: Bode plot after Miller compensation.

In order to minimize the power-supply sensitivity, R should be maximized [36]. Considering chip area and process variation, R is chosen to be 1 kohm. For a peaking current source, the current is not a monotonic growing function of the power supply. A maximum current exist for a voltage supply variation. Therefore, to minimize the power supply sensitivity, K is chosen in such a way that the current is locally independent on the voltage supply around the nominal current value. This condition happens for a V_{dd} of 0.9 V when $K = 7$. At last, we adjust W/L to 30 um / 1 um for a nominal current of 100 uA.

6.5.2 Power Supply and Temperature Sensitivity

DC-sweep simulations are performed to obtain the power-supply and temperature sensitivity of the output current.

The current vs. the supply voltage is plotted at the left of Fig. 6.17. The peak of the current is tuned to the nominal power supply voltage of 0.9 V. The derivative of output current to supply voltage at V_{dd}=0.9 V is 0. Furthermore, a 10% voltage variation (from 0.81V to 0.99V) causes a maximum output change from 95.64 uA to 95.35 uA, i.e. a 0.3% current variation.

A temperature variation from 0 to 85 degrees Celsius yields a biasing current from 88 to 115 uA as plotted at the right of Fig. 6.17. Thus, a positive temperature coefficient of 0.318 uA/K is obtained.

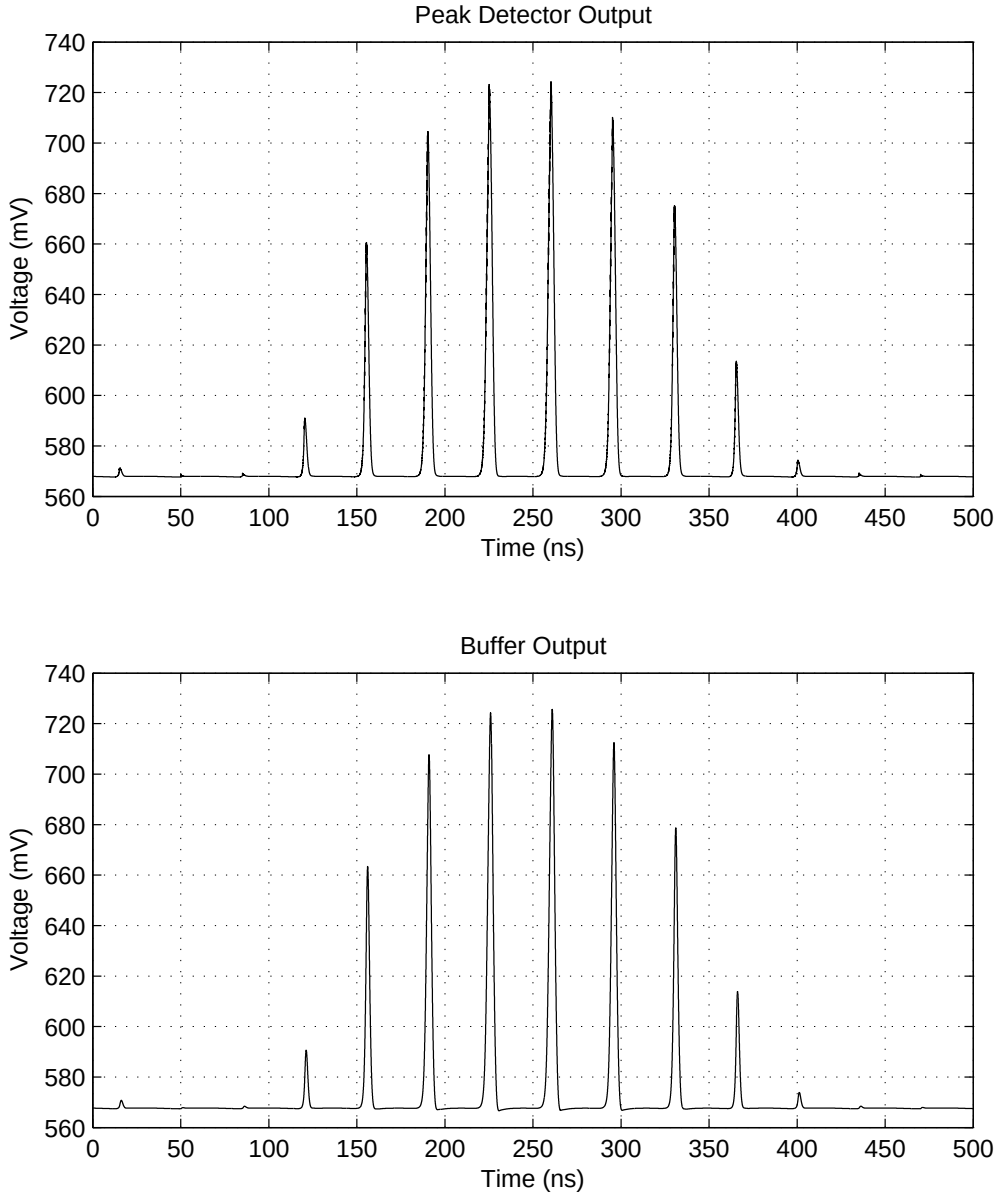

Figure 6.15: Voltage output of the peak detector and the buffered version.

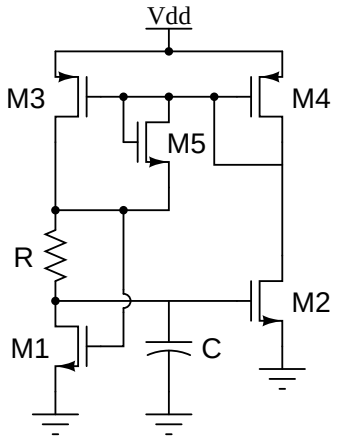

Figure 6.16: The schematic of the peaking current reference.

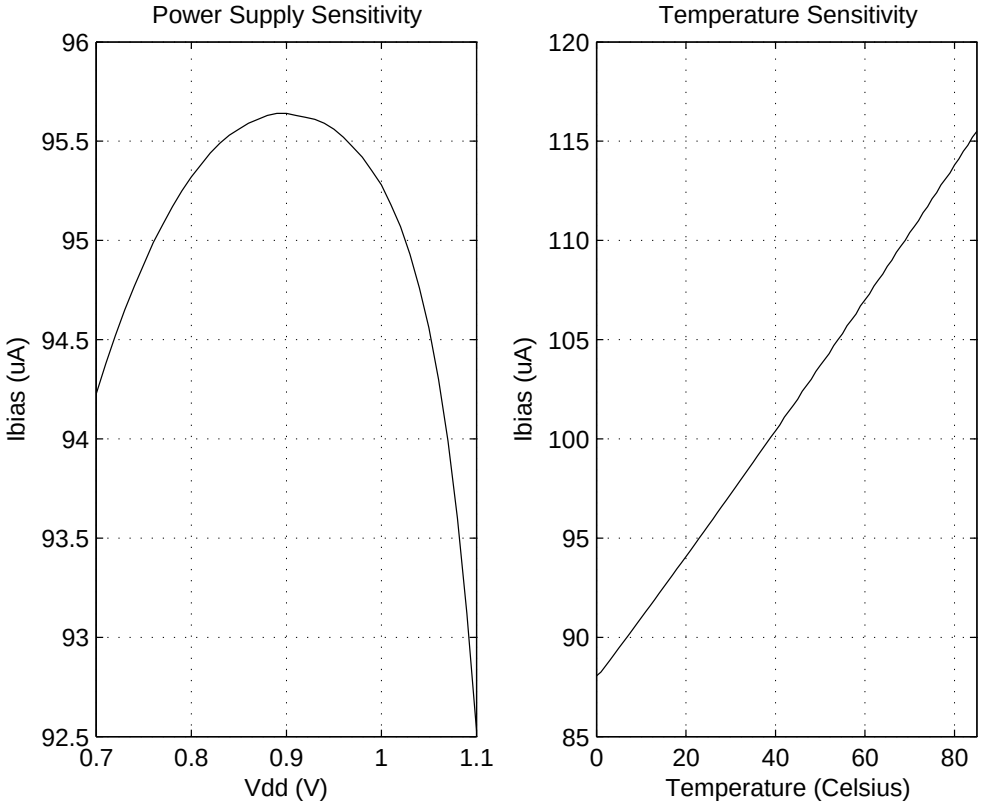

Figure 6.17: Power-supply and temperature sensitivity of the output current.

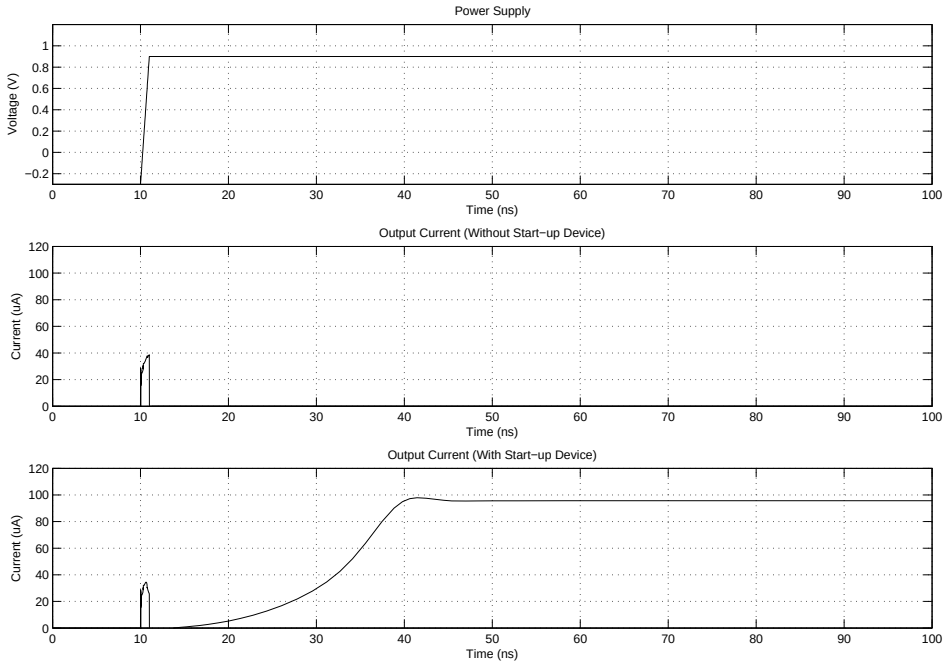

Figure 6.18: Power-up behavior.

6.5.3 Power-up Behavior

Transient simulations are also performed to examine the power-up behavior. The supply voltage of 0.9 V is applied as a 1 ns step, shown at the top of Fig. 6.18. The responses of the circuits with and without the start-up device (transistor M5) are shown at the bottom and middle of Fig. 6.18, respectively. From the figure, it is observed that transistor M5 accelerates the start-up of the current reference circuit significantly.

Chapter 7

Receiver Performance

7.1 Introduction

In Chapter 5 and 6, circuit blocks of the UWB-FM super-regenerative receiver are presented. This chapter evaluates the performance of the receiver as a whole.

Section 7.2 introduces the simulation setup and presents the results. A test-bench is designed to simulation the system consisting of all the building blocks in the circuit level. Simulation results are compared with the receiver specification derived in Chapter 4 to show the validity of the design.

The global optimization of power consumption is discussed in Section 7.3. This procedure leads to further power reduction, since the individual power minimization for each block does not necessarily yield the minimum power in total.

7.2 Test-bench Simulation

7.2.1 Transient Noise Analysis

Super-regenerative receivers are nonlinear time-varying dynamical systems. Furthermore, super-regeneration is the transient response of such a dynamical system. Therefore, fast circuit simulation techniques such as periodic steady-state in time domain and harmonic balance in frequency domain neglect super-regeneration effect completely. Only the transient analysis, using the method of time domain numerical integration, can simulate the behavior of super-regenerative receivers.

Noise is a stochastic process. In time domain, noise is simulated by a random noise generator. Depending on the power of a noise source, the random noise generator produces a time series of random numbers with a certain variance.

The transient noise analysis is a time domain circuit simulation technique. It uses the time-domain integration method to calculate the transient response of a dynamical system with internal noise. At each integration step, random numbers

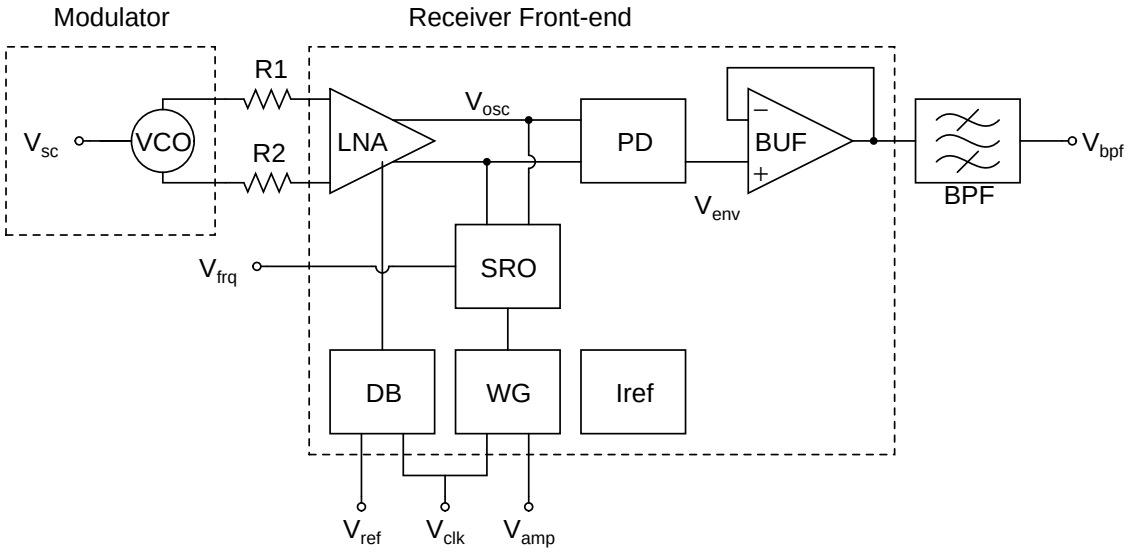

Figure 7.1: Block diagram of the receiver test-bench.

are generated at first, representing the value of noise sources at that time. Then, these noise signals, together with other deterministic signals are used as stimuli to the system. After that, nodal analysis is performed to calculate the instantaneous node voltages and loop currents. At last, the voltages across capacitors and the currents flowing through inductors are calculated by numerical integration for the next time step.

We use the transient noise analysis to characterize the noise performance of the super-regenerative receiver. The simulation procedure consists of 2 steps. First, a transient analysis is performed to the receiver under excitation of the UWB-FM RF signal. The RMS value of the output is the signal power. Then, several passes of transient noise analysis are performed to the receiver with no RF excitation. The mean of the RMS value of the outputs is the noise power. In this way, the output SNR is obtained and the noise figure of the receiver can be calculated.

There are three issues need to be justified before applying the aforementioned simulation procedure. Firstly, superposition property is implicitly assumed. This assumption is valid as long as the SRO is working in the linear region, as indicated in Equ. 3.31. Secondly, the output noise is implicitly assumed to be stationary and ergodic. Otherwise, many long noise sample paths are required to calculate the noise power. Thirdly, the noise samples to calculate the statistical variance is assumed to be enough. Two passes of 5000 ns transient noise simulation results are used to calculate the RMS noise power. We do not have enough computation power to do a more intensified simulation.

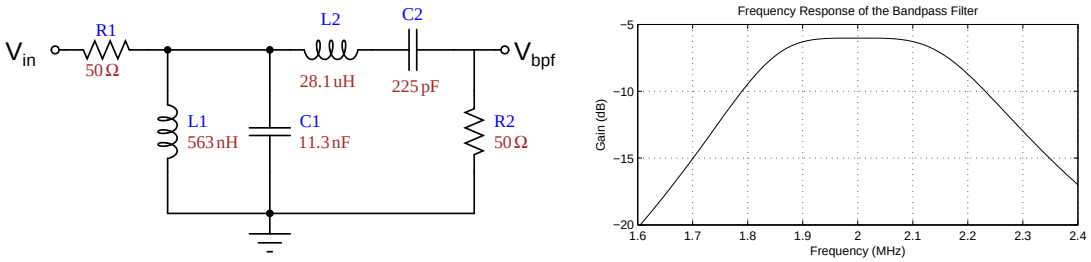

Figure 7.2: Bandpass filter and its frequency response.

7.2.2 The Test-bench

The schematic used for test-bench simulation is plotted in Fig. 7.1. The receiver front-end to be evaluated consists of all the circuit blocks introduced in the previous chapters, namely the LNA, SRO, peak detector (PD), waveform generator (WG) for SRO, dynamic biasing (DB) for LNA, output buffer (BUF) and the current reference (Iref).

The UWB-FM RF signal is generated by an ideal voltage-controlled oscillator (VCO) being controlled by a 1 MHz triangular subcarrier (V_{sc}). The VCO oscillates at 4.5 GHz when V_{sc} is zero, and it has a gain of 500 MHz/V. V_{sc} has a peak-to-peak value of 1 V and a DC value of zero. In this way, the output of the VCO is an FM modulated signal having a center frequency of 4.5 GHz and a bandwidth of 500 MHz.

According to Equ. 4.4, the received power is -80 dBm for a communication range of 10 meters. This signal power should generate a 31.6 uV voltage across the input impedance of LNA of 100 ohm. To take the LNA matching into consideration, we plug in two 50 ohm resistors, R1 and R2, and double the voltage output of VCO to 63.2 uV. As a result, the input power to the LNA is -80 dBm if it is power matched.

The output of the receiver is passed through a bandpass filter (shown as BPF in the figure). This filter has two functions. Firstly, it recovers the subcarrier from the amplitude modulated pulses, so the mission of the receiver front-end is accomplished. Secondly, the processing gain is obtained by this filter, so that the noise figure or the sensitivity of the receiver can be measured.

A second-order Butterworth filter, implemented in the LC-ladder form, is used in this test-bench. The schematic and the frequency response of this filter are shown in Fig. 7.2. As shown in the graph, the filter has a 2 MHz center frequency and a 400 kHz bandwidth. As a result, it passes through the FSK modulated subcarrier while eliminates the out-of-band noise as much as possible.

The reason that this filter is not integrated on-chip is because the back-end of the receiver, i.e. the FSK demodulator, may not require this filter at all. For example, if the noncoherent FSK detection is performed, two detuned bandpass filters can demodulate the FSK into binary signal without prefiltering.

7.2.3 Simulation Results

A transient simulation is performed to the test-bench. The voltage waveforms of the input subcarrier, SRO oscillation, its envelope and the output after bandpass filter are plotted in Fig. 7.3. As shown in the graph, the receiver is capable of recovering the subcarrier. Since the FM signal is converted to a 100% modulated AM signal, and the noncoherent detection of this DSB-AM signal neglects the phase information completely, the 1 MHz subcarrier is recovered as a 2 MHz signal.

The transient noise simulation is performed to the test-bench with zero RF input. The voltage outputs of the SRO, the peak detector and the bandpass filter are plotted in Fig. 7.4. The SRO oscillation in this simulation is caused by the noise only.

Comparing the amplitudes of the pulses from Fig. 7.4 to that shown in Fig. 7.3, we observe that the noise generates larger pulses than the signal does. In other words, noise power is larger than the signal power. The only property that distinguishes signal from noise is that the signal power is concentrated in a specific frequency band while the noise power is evenly distributed. The bandpass filter in the test-bench filters out all the out-of-band noise, so that noise power is reduced while the signal power is left intact. The comparison of the V_{bpf} signals shown in Fig. 7.4 and Fig. 7.3 shows this SNR improvement.

The output signal-to-noise ratio is calculated by the RMS value of the signal divided by that of the noise. A conservative estimation using the peak-to-peak voltage of the signal divided by the largest peak-to-peak voltage of the noise yields an output SNR of 14.3 dB.

The whole receiver excluding the output voltage buffer draws 2.273 mA in average from a 0.9V voltage supply. Thus, a power consumption of 2.046 mW is obtained.

7.3 Global Power Reduction: A Step-controlled SRO

7.3.1 Motivation

Compared with a slope-controlled SRO, a step-controlled SRO yields at least 20% reduction of dynamic range, and consumes more power for the same voltage swing, as discussed in Section 5.2. Because of these reasons, the slope-control mechanism is chosen in the first place.

However, the slope-control requires a complex saw-tooth waveform generator to bias the SRO. This generator consumes extra power, which is even more than that of the SRO, as discussed in Section 6.2. It is possible to reduce this extra power but the penalty paid is a performance degradation.

On the other hand, the biasing circuit for a step-controlled SRO is much simpler. It can be implemented by a current mirror with its gates periodically pulled down

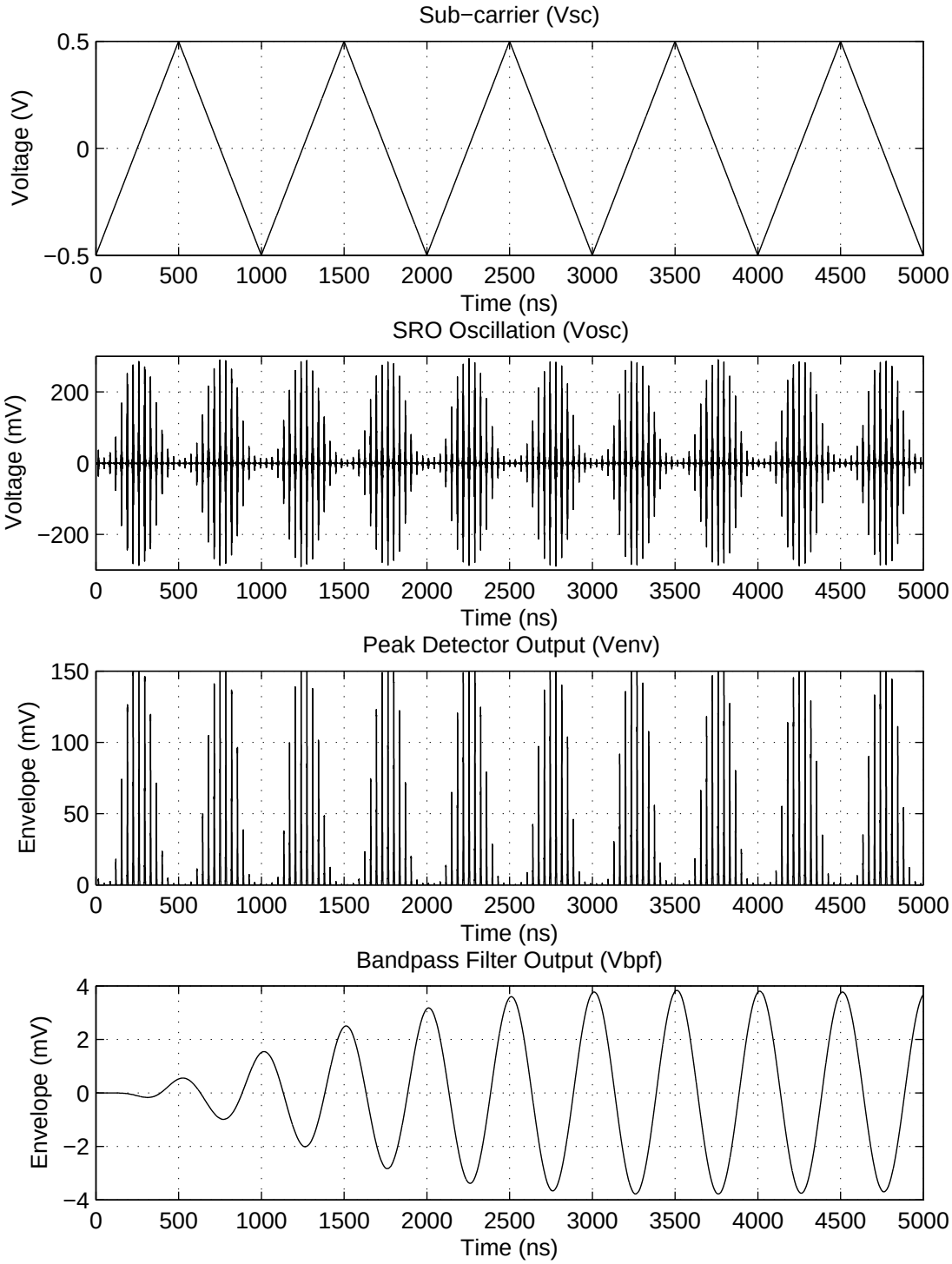

Figure 7.3: Receiver outputs under signal excitation.

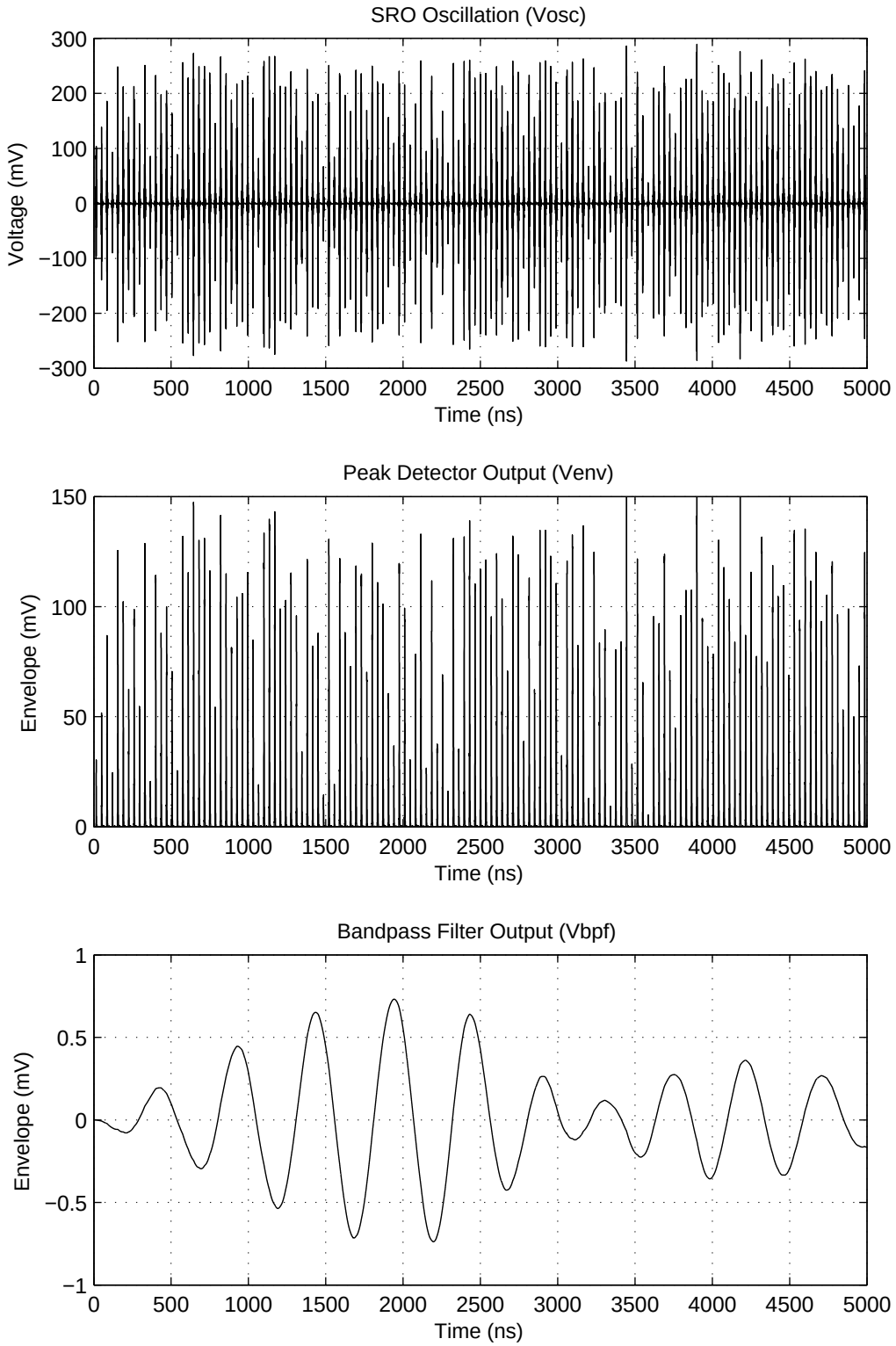

Figure 7.4: Receiver outputs without input signal.

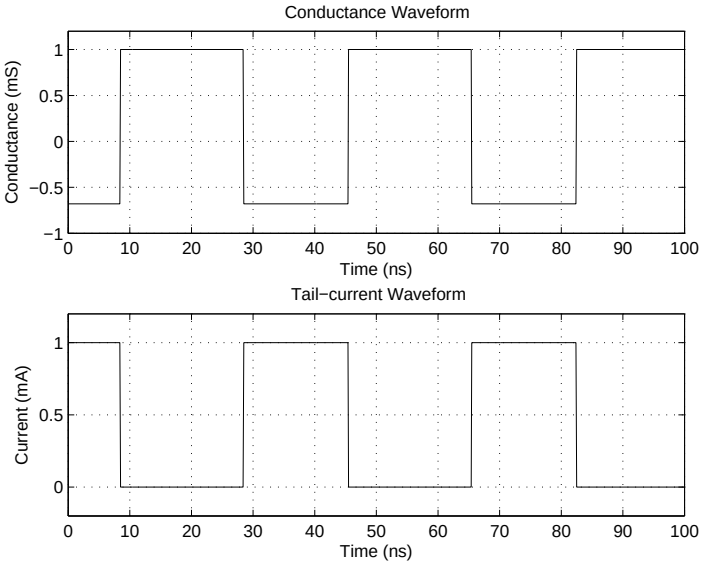

Figure 7.5: Conductance and Tail current waveform for step-control.

by a clocked switch.

Therefore, applying step-control may lead to global power reduction, despite the increased power and the inferior performance of the SRO.

7.3.2 The Adapted Design for Step-control

The slope-controlled super-regenerative receiver front-end already designed consists of an LNA, an SRO, a peak detector, an output buffer, a current reference, the dynamic biasing circuit for the SRO and that for the LNA. In the adapted version applying the step-control, the SRO is tuned slightly, the biasing waveform generator is substituted by a switch, and the logic is inverted for the dynamic biasing of the LNA. The rest of the circuit blocks, namely the LNA, the peak detector, the output buffer and the current reference, are utilized in the new design without modification.

7.3.2.1 The Step-controlled SRO

Biasing Waveform In Subsection 5.2.4, it is discussed that a step-controlled start-up and quenching needs a rectangular waveform. The ideal conductance waveform yielding the optimum frequency response is plotted in the top of Fig. 7.5. In the plot, the negative conductance is set to -0.681 mS according to Tab. 5.1. And the duration of the negative conductance is 16.5 ns determined by the certain amount of gain amplifying the RF signal to an oscillation amplitude of 300 mV.

The conductance waveform is generated by a rectangular-pulse current source. The required waveform of this source is shown in the bottom of Fig. 7.5.

Biasing Current and Transistor Widths For a certain negative conductance, there is still one degree of freedom to select the biasing current or transistor widths. This selection involves the dynamic range - power trade-off discussed in Subsection 5.2.5. Basically, a small biasing current and large transistors are power saving but the dynamic range is limited. A large biasing current requires small transistors to generate a certain negative conductance. This large current density yields large overdrive voltages and the oscillation amplitude is voltage limited. So an optimum current density exists for a certain negative conductance and voltage supply.

Extensive simulations show that this optimum is achieved when the biasing tail current is 1 mA and the width of each transistor of the cross coupled pair is 5 um.

7.3.2.2 The Dynamic Biasing Circuit

The dynamic biasing circuit for the step-controlled SRO and the LNA is shown in Fig. 7.6. Both the SRO and LNA are biased by current mirrors with switches attached to the gates. When either one is quenched, the corresponding switch is closed to pull down the gate voltage and shut down the current flow.

The switch quenching the SRO is directly controlled by an external clock. The other one quenching the LNA is controlled by a delayed version of the external clock. As is shown in the top of Fig. 7.6, the delay-line is a logically inverted version of the one discussed in Section 6.3. The simulated node voltages and biasing currents are shown in Fig. 7.7.

7.3.3 Test-bench Simulation Results

Test-bench simulations similar to those introduced in Section 7.2 are performed to evaluate the step-controlled super-regenerative receiver. The simulation results are shown in Fig. 7.8 and Fig. 7.9, for signal and noise excitation, respectively. The same conservative estimation using the peak-to-peak voltage of the signal divided by the largest peak-to-peak voltage of the noise yields an output SNR of 13.2 dB.

The step-controlled super-regenerative receiver excluding the output voltage buffer draws 1.996 mA in average from a 0.9V voltage supply. Thus, a power consumption of 1.796 mW is obtained.

7.3.4 The Power Reduction of the Step-controlled Receiver

In the previous sections, two super-regenerative receiver front-ends, one slope- and the other step-controlled, are designed for UWB-FM reception. Test-bench simulations indicate that both designs satisfy the system specification. Under this condition, the minimum power consumed by the 2 receivers is compared.

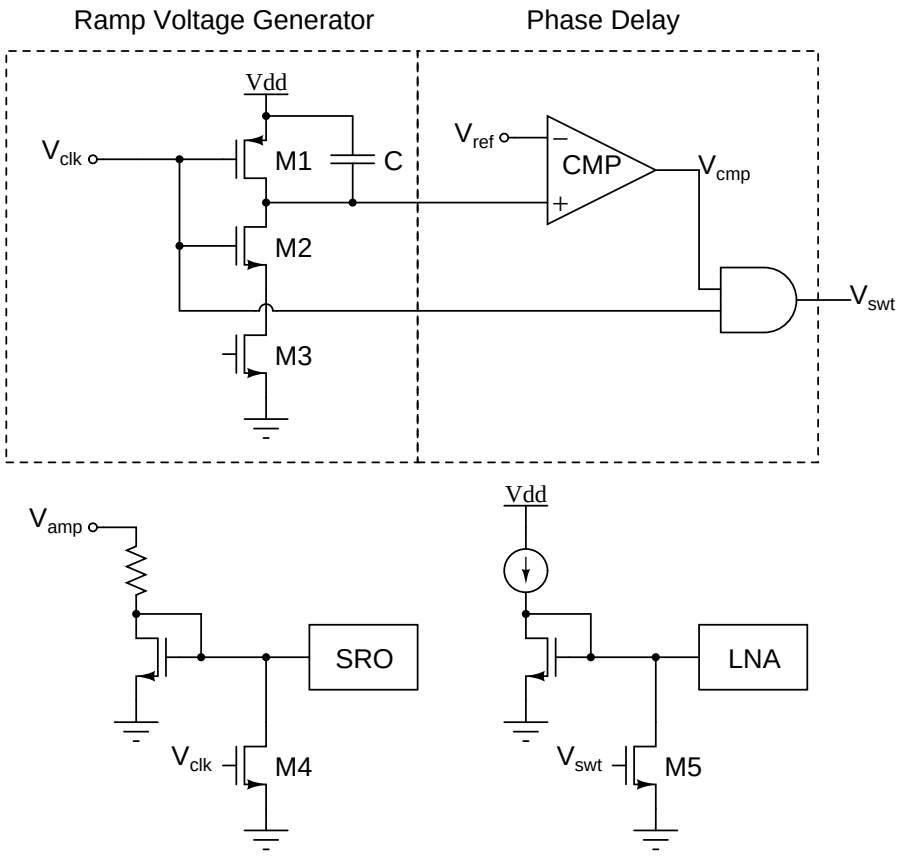

Figure 7.6: The dynamic biasing circuits for the SRO and the LNA.

	Slope-controlled	Step-controlled
SRO	257 uA	428 uA
Dynamic Biasing for SRO	448 uA	100 uA
Total	705 uA	528 uA

Table 7.1: The comparison of current consumption between the slope- and step-controlled receivers.

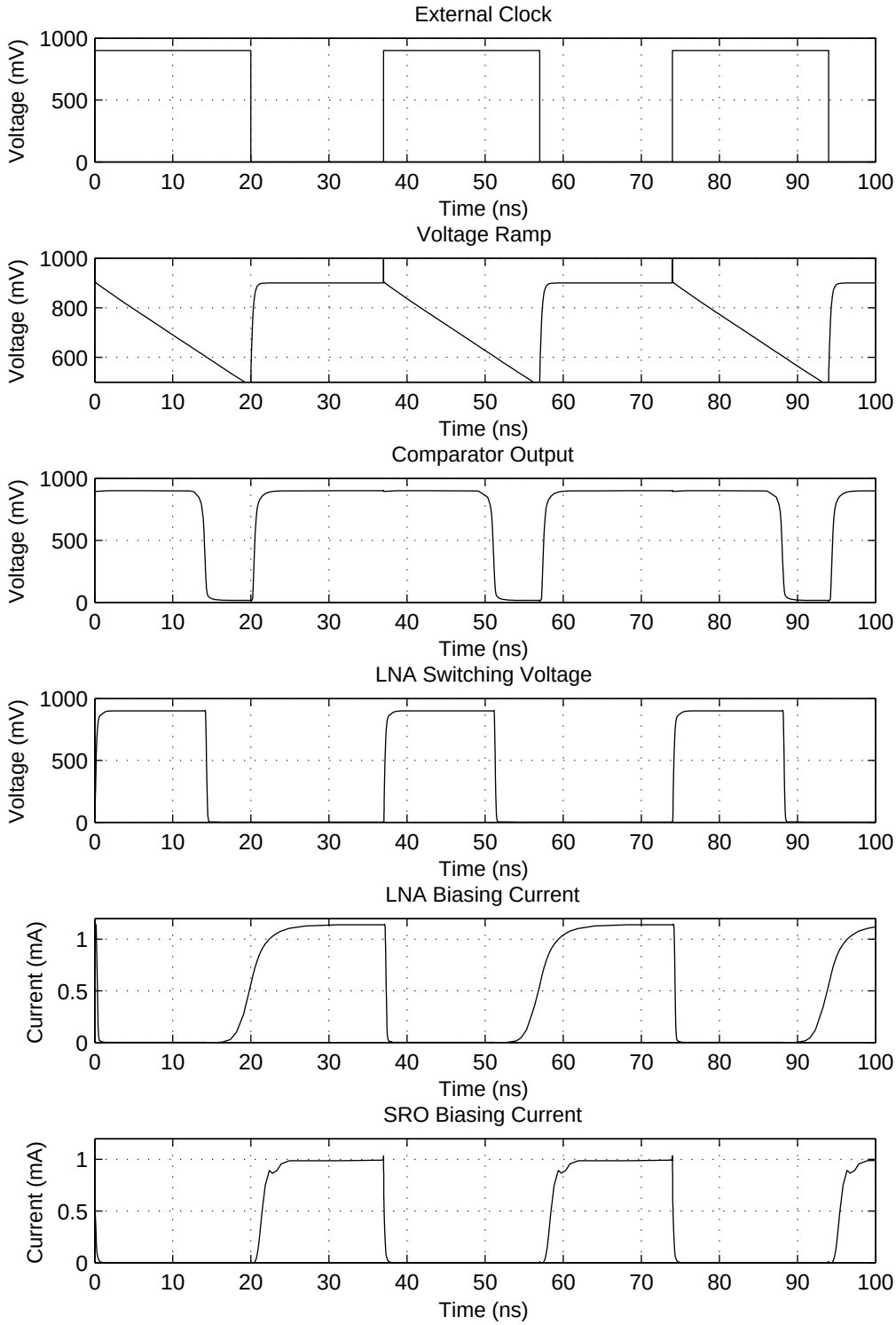

Figure 7.7: Delay-line voltages and biasing currents of the SRO and the LNA.

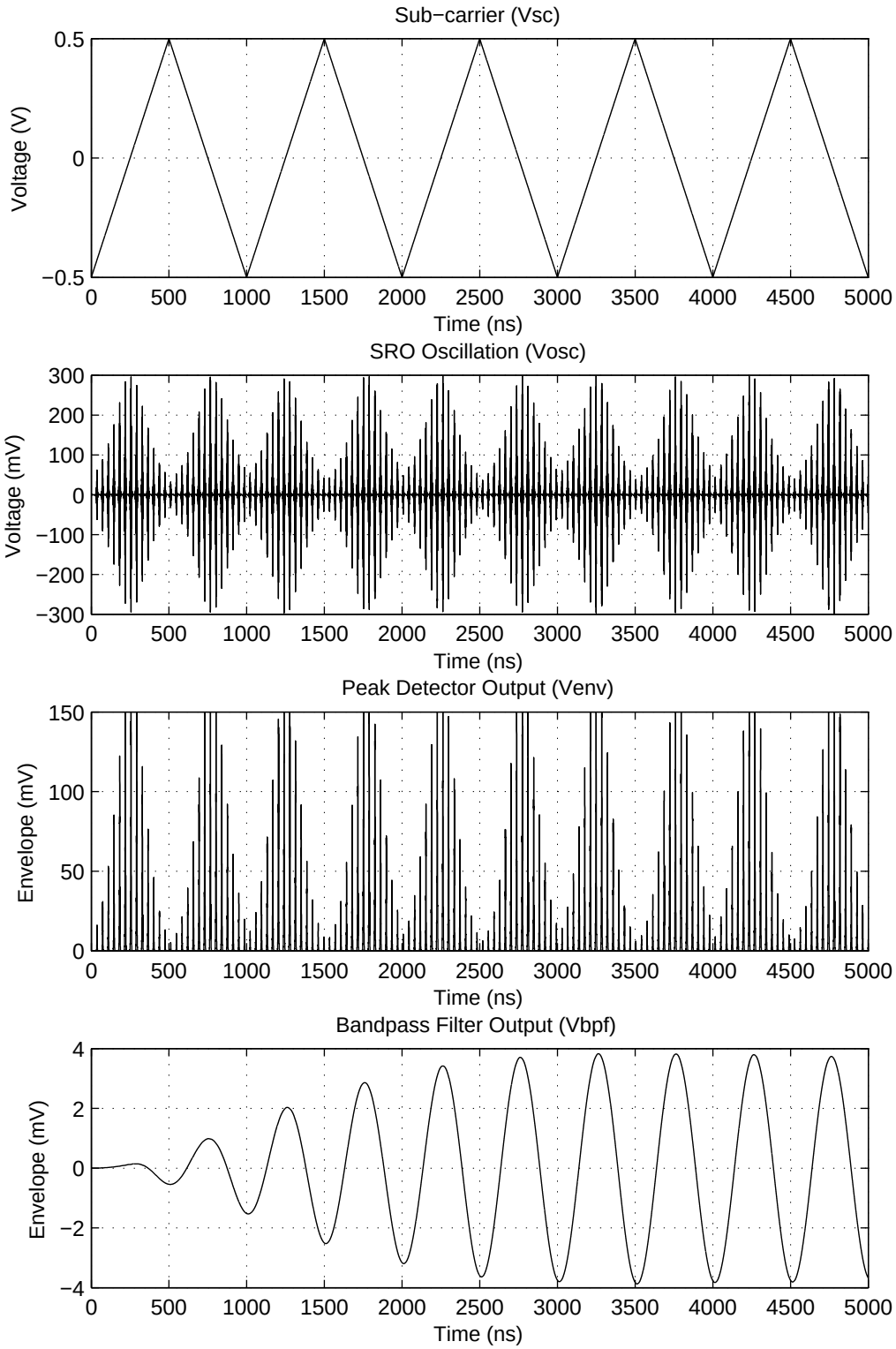

Figure 7.8: Receiver outputs under signal excitation.

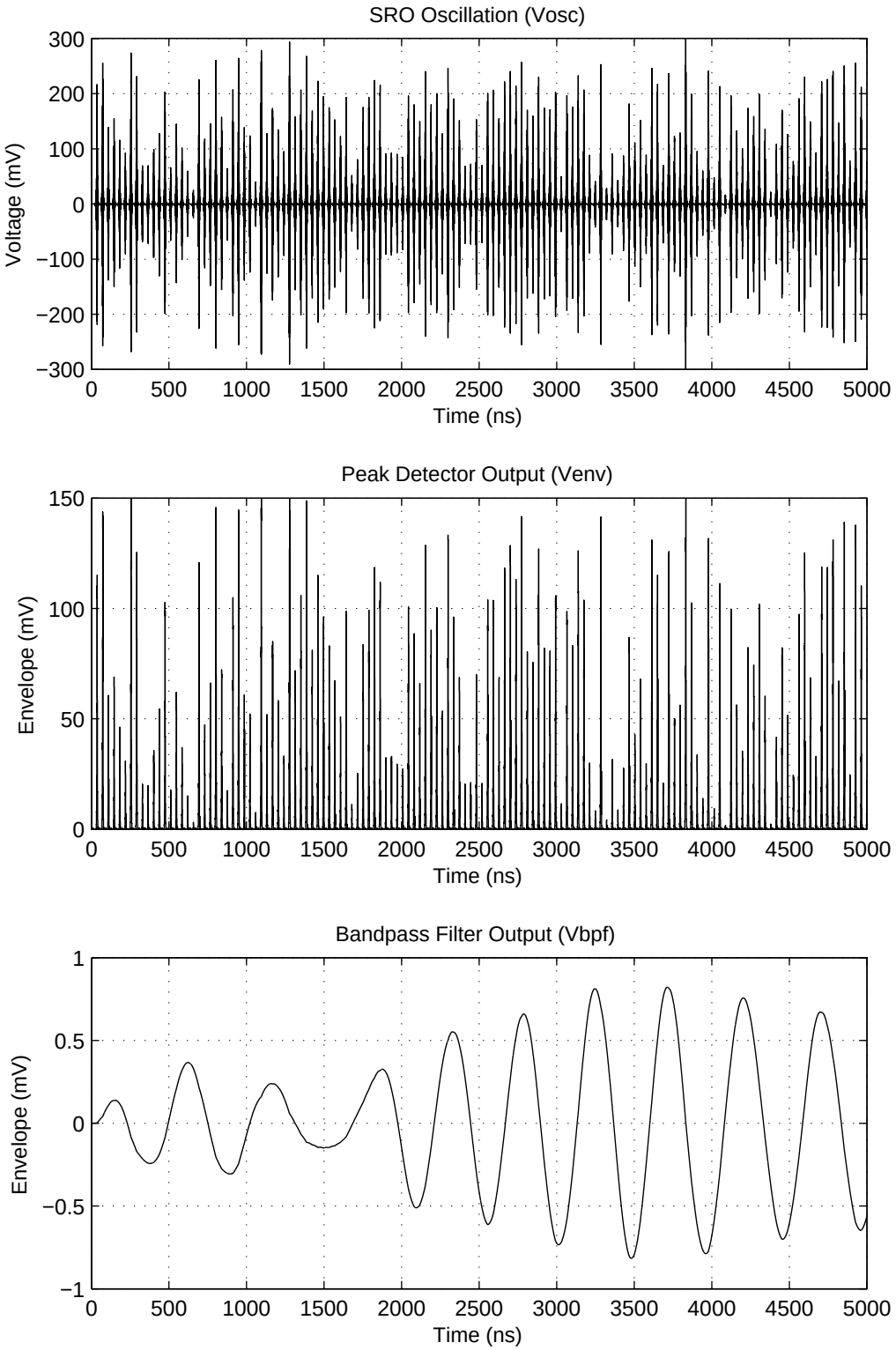

Figure 7.9: Receiver outputs without input signal.

Besides the power consumed by the LNA, peak detector and the biasing, which are nearly equal for the two receivers, the power dissipation of the SRO and its dynamic biasing circuit is listed in Tab. 7.1. We can observe from the table that although the slope-control yields a smaller SRO power consumption than the step-control does, as predicted theoretically in Subsection 5.2.4, the extra power used to generate the complex waveform outweighs its benefit. In contrast, the step-control is power consuming in principle, but the simple power management circuit leads to overall power saving.

Chapter 8

Conclusions

8.1 Summary of Results

UWB-FM systems, targeting on short-range low-data-rate wireless applications, demand receivers with low complexity and low power consumption. In this research, a fully integrated super-regenerative receiver in IBM 90-nm RF CMOS technology is designed to detect 500 MHz bandwidth UWB-FM signals at 4.5 GHz. Circuit simulations show that a receiver sensitivity of -82.2 dBm is attainable for a 100 kbps baseband data-rate and 10^{-6} bit-error-rate. The whole circuit draws an average of 2 mA from a 0.9 V supply.

Tab. 8.1 compares the performance of this work with another two recently published UWB-FM receivers. As shown in the table, this receiver demonstrates higher sensitivity while consumes remarkably less power.

The contribution of this work also includes an innovative optimization of the quenching waveform for WBFM detection and a novel low-power driven design procedure for LNAs.

In conclusion, super-regenerative receivers, due to their simplicity and low power-consumption, are promising for short-range low-data-rate UWB-FM applications.

	Tong [12]	Gerrits [37]	This work
RF frequency	4 GHz	4 GHz	4.5 GHz
RF bandwidth	2 GHz	500 MHz	500 MHz
Sensitivity	N/A	-74 dBm	-82.2 dBm
Data rate	N/A	62.5 kbps	100 kbps
Bit error rate	N/A	10^{-4}	10^{-6}
Power consumption	19.4 mW	9.6 mW (w/o LNA)	1.8 mW
Technology	0.18 um CMOS	0.18 um BiCMOS	90 nm CMOS

Table 8.1: Performance comparison of UWB-FM receivers.

8.2 Future Work

This research demonstrates the feasibility and advantage of performing UWB-FM detection by super-regenerative receivers. Layout, fabrication and physical measurement of this design is necessary to make the point more concrete. Industrial application of this design requires further reliability and yield analysis.

UWB-FM is designed to have multiuser capability and robustness to narrow-band interference [28, 38]. The multiuser capability is briefly discussed in Section 4.2. The feasibility of using this receiver for subcarrier FDMA requires further study of the LNA linearity. Qualitatively, the susceptibility to narrow-band interference is the most at the center frequency, 4.5 GHz, and the least at 4.25 and 4.75 GHz. The quantitative relation of tolerable interference strength versus frequency is a subject for future study.

The current design of this receiver assumes an external clock to quench the oscillation periodically. However, it leaves the freedom of generating this clock to the user. Self-quenching is possible by the addition of a comparator and a monostable multivibrator. In this configuration, oscillations are quenched as long as the output envelope reaches a certain level. Self-quenching leads to very simple implementation and presumably low power consumption. The penalty paid is the reduced dynamic range. Whether the dynamic range reduction is acceptable for UWB-FM applications is a subject for future research.

RF-MEMS technology may reduce the power consumption considerably. According to Section 5.2, the lower bound of power consumption is ultimately limited by the quality factor of the resonator. In the literature, bulk acoustic wave (BAW) resonators are increasingly used to obtain super-regenerative receivers working at micro-watt power levels. The extra benefit of using high-Q devices includes the selectivity and frequency stability improvements.

Bibliography

[1] J. F. Gerrits and J. R. Farserotu., "Ultra wideband fm: A straightforward frequency domain approach," *European Microwave Conference, 2003. 33rd*, pp. 853–856, Oct. 2003.

[2] E. H. Armstrong, "Signaling systems," *US Patent*, July 1922.

[3] J. Whitehead, *Super-Regenerative Receivers*. Cambridge Press, 1950.

[4] P. Favre, N. Joehl, A. Vouilloz, P. Deval, C. Dehollain, and M. Declercq, "A 2-v 600-ÎŒa 1-ghz bicmos super-regenerative receiver for ism applications," *Solid-State Circuits, IEEE Journal of*, vol. 33, pp. 2186–2196, Dec 1998.

[5] A. Vouilloz, M. Declercq, and C. Dehollain, "A low-power cmos super-regenerative receiver at 1 ghz," *Solid-State Circuits, IEEE Journal of*, vol. 36, pp. 440–451, Mar 2001.

[6] N. Joehl, C. Dehollain, P. Favre, P. Deval, and M. Declerq, "A low-power 1-ghz super-regenerative transceiver with time-shared pll control," *Solid-State Circuits, IEEE Journal of*, vol. 36, pp. 1025–1031, Jul 2001.

[7] J.-Y. Chen, M. Flynn, and J. Hayes, "A fully integrated auto-calibrated super-regenerative receiver in 0.13-ÎŒm cmos," *Solid-State Circuits, IEEE Journal of*, vol. 42, pp. 1976–1985, Sept. 2007.

[8] I. McGregor, E. Wasige, and I. Thayne, "Sub-50ÎŒw, 2.4 ghz super-regenerative transceiver with ultra low duty cycle and a 675ÎŒw high impedance super-regenerative receiver," *Microwave Conference, 2007. European*, pp. 1322–1325, Oct. 2007.

[9] B. Otis, Y. Chee, and J. Rabaey, "A 400 /spl mu/w-rx, 1.6mw-tx super-regenerative transceiver for wireless sensor networks," *Solid-State Circuits Conference, 2005. Digest of Technical Papers. ISSCC. 2005 IEEE International*, pp. 396–606 Vol. 1, Feb. 2005.

[10] J. L. Bohorquez, J. L. Dawson, and A. P. Chandrakasan, "A 350ÎŒw cmos msk transmitter and 400ÎŒw ook super-regenerative receiver for medical implant communications," *VLSI Circuits, 2008 IEEE Symposium on*, pp. 32–33, June 2008.

[11] J. Gerrits, J. Farserotu, and J. Long, "A wideband fm demodulator for uwb applications," *Research in Microelectronics and Electronics 2006, Ph. D.*, pp. 461–464, 0-0 2006.

[12] T. Tong, J. Mikkehen, and T. Larsen, "A 0.18 mum cmos implementation of a low power, fully differential rf front-end for fm-uwb based p-pan receivers," *Communication systems, 2006. ICCS 2006. 10th IEEE Singapore International Conference on*, pp. 1–5, 30 2006-Nov. 1 2006.

[13] M. H. L. Kouwenhoven, *High Performance Frequency Demodulation Systems*. Delft University Press, 1998.

[14] F. Moncunill-Geniz, P. Pala-Schonwalder, C. Dehollain, N. Joehl, and M. Declercq, "An 11-mb/s 2.1-mw synchronous superregenerative receiver at 2.4 ghz," *Microwave Theory and Techniques, IEEE Transactions on*, vol. 55, pp. 1355–1362, June 2007.

[15] D. Ash, "A low cost superregenerative saw stabilized receiver," *Consumer Electronics, IEEE Transactions on*, vol. CE-33, pp. 395–404, Aug. 1987.

[16] F. Moncunill, O. Mas, and P. Pala, "A direct-sequence spread-spectrum superregenerative receiver," *Circuits and Systems, 2000. Proceedings. ISCAS 2000 Geneva. The 2000 IEEE International Symposium on*, vol. 1, pp. 68–71 vol.1, 2000.

[17] F. Moncunill-Geniz, P. Pala-Schonwalder, and F. del Aguila-Lopez, "New superregenerative architectures for direct-sequence spread-spectrum communications," *Circuits and Systems II: Express Briefs, IEEE Transactions on*, vol. 52, pp. 415–419, July 2005.

[18] M. Pelissier, D. Morche, and P. Vincent, "Rf front end of uwb receiver based on super-regeneration," *Ultra-Wideband, 2007. ICUWB 2007. IEEE International Conference on*, pp. 180–183, Sept. 2007.

[19] F. Xavier Moncunill-Geniz, P. Pala-Schonwalder, F. del Aguila-Lopez, and R. Giralt-Mas, "Application of the superregenerative principle to uwb pulse generation and reception," *Electronics, Circuits and Systems, 2007. ICECS 2007. 14th IEEE International Conference on*, pp. 935–938, Dec. 2007.

[20] M. Anis, R. Tielert, and N. Wehn, "Fully integrated self-quenched super-regenerative uwb impulse detector," *Wireless Pervasive Computing, 2008. ISWPC 2008. 3rd International Symposium on*, pp. 773–775, May 2008.

[21] H. Kalmus, "Some notes on superregeneration with particular emphasis on its possibilities for frequency modulation," *Proceedings of the IRE*, vol. 32, pp. 591–600, Oct. 1944.

[22] L. Hernandez and S. Paton, "A superregenerative receiver for phase and frequency modulated carriers," *Circuits and Systems, 2002. ISCAS 2002. IEEE International Symposium on*, vol. 3, pp. III–81–III–84 vol.3, 2002.

[23] J. Ayers, K. Mayaram, and T. Fiez, "A low power bfsk super-regenerative transceiver," *Circuits and Systems, 2007. ISCAS 2007. IEEE International Symposium on*, pp. 3099–3102, May 2007.

[24] F. Moncunill-Geniz, P. Pala-Schonwalder, and O. Mas-Casals, "A generic approach to the theory of superregenerative reception," *Circuits and Systems I: Regular Papers, IEEE Transactions on*, vol. 52, pp. 54–70, Jan. 2005.

[25] T. H. Lee, *The Design of CMOS Radio-Frequency Integrated Circuits*. Cambridge University Press, 2nd. ed., 2004.

[26] J. Whelehan, "Low-noise amplifiers-then and now," *Microwave Theory and Techniques, IEEE Transactions on*, vol. 50, pp. 806–813, Mar. 2002.

[27] Y. Xue, J. Gerrits, H. Choi, Nikhil, and S. K., "Specification for prototyping from phy and layer 2 (update d3.3.4a)," Tech. Rep. IST-507102 D3.3.4b, My Personal Adaptive Global NET, Dec. 2005.

[28] J. Gerrits, J. Farserotu, and J. Long, "Multi-user capabilities of uwbfm communications systems," *Ultra-Wideband, 2005. ICU 2005. 2005 IEEE International Conference on*, pp. 6 pp.–, Sept. 2005.

[29] F. C. Commission, "First report and order," *Revision of Part 15 of the Commission's Rules Regarding Ultra-Wideband Transmission Systems*, Apr. 22 2002.

[30] J. Keignart, J.-B. Pierrot, N. Daniele, A. Alvarez, M. Lobeira, J. L. Garcia, G. Valera, and R. P. Torres, "U.c.a.n. report on uwb basic transmission loss," Tech. Rep. IST-2001-32710, U.C.A.N., Mar. 2003.

[31] C. Mutti, F. Bauer, K. Schoo, M. Monti, F. Platbrood, A. Pollini, J. Gerrits, J. Ayadi, and I. Siaud, "Requirement specification for phy-layer," Tech. Rep. IST-507102 D3.2.1, My Personal Adaptive Global NET, Jun. 2004.

[32] ETSI, *Electromagnetic compatibility and Radio spectrum Matters (ERM); Wideband Transmission systems; Data transmission equipment operating in the 2,4 GHz ISM band and using spread spectrum modulation techniques; Part 1: Technical characteristics and test conditions.* No. ETSI EN 300 328-1 in European Standard (Telecommunications series), ETSI, v1.3.1 ed., Dec. 2001.

[33] IBM, *CMOS 9SF Technology Design Manual*, vol. ES 88H1175. IBM, Setp. 2007.

[34] R. Meyer, "Low-power monolithic rf peak detector analysis," *Solid-State Circuits, IEEE Journal of*, vol. 30, pp. 65–67, Jan 1995.

[35] D. Cassan and J. Long, "A 1-v transformer-feedback low-noise amplifier for 5-ghz wireless lan in 0.18-/spl mu/m cmos," *Solid-State Circuits, IEEE Journal of*, vol. 38, pp. 427–435, Mar 2003.

[36] B. Razavi, *Design of Analog CMOS Integrated Circuits.* McGraw-Hill, 2001.

[37] J. Gerrits, J. Farserotu, and J. Long, "A wideband fm demodulator for a low-complexity fm-uwb receiver," *Wireless Technology, 2006. The 9th European Conference on*, pp. 99–102, Sept. 2006.

[38] J. Gerrits, J. Farserotu, and J. Long, "Low-complexity ultra wideband communications," *Circuits and Systems, 2007. ISCAS 2007. IEEE International Symposium on*, pp. 757–760, May 2007.